MOLECULAR SIMULATION STUDY OF ADSORPTION, DIFFUSION AND DISSOCIATION

by

Liang Chen

B.S. in Chemical Engineering,

Nanjing University, 2001

Submitted to the Graduate Faculty of

the School of Engineering in partial fulfillment

of the requirements for the degree of

Doctor of Philosophy

University of Pittsburgh

2006

UNIVERSITY OF PITTSBURGH

SCHOOL OF ENGINEERING

This dissertation was presented

by

Liang Chen

It was defended on

January 25th, 2006

and approved by

J. Karl Johnson, Ph. D., Professor

Kenneth D. Jordan, Ph. D., Professor

Götz Veser, Ph. D., Assistant Professor

Joseph J. McCarthy, Ph. D., Associate Professor

Christopher Matranga, Ph. D., Research Scientist

Dissertation Advisor: J. Karl Johnson, Ph. D., Professor

MOLECULAR SIMULATION STUDY OF ADSORPTION, DIFFUSION AND DISSOCIATION

Liang Chen, Ph. D.

University of Pittsburgh, 2006

There are two main objectives in my research work. The first objective is to investigate the adsorption behavior of various gases on single walled carbon nanotubes. This is accomplished by using the classical molecular simulation methods. Our simulation work has provided molecular level interpretation of some interesting phenomena observed experimentally by our collaborators. The second objective is to study the catalytic properties of metal/metal carbide surfaces and interfacial phenomena by using *ab initio* density functional theory.

We have studied the adsorption of various gases on carbon nanotubes by using classical molecular simulation and optimization techniques. We specifically have investigated the displacement of adsorption on different adsorption sites. The systems investigated include CO_2 on SWNT, Xe/CF_4 on SWNT and CO_2/Xe on SWNT. Our simulations indicate that CO_2 is easily replaced from the endohedral and interstitial sites of SWNT bundles by Xe, while the groove/external surface sites loose much less CO_2. These calculations agree very well with the experimental observations. We have also observed unique one dimensional behavior of gases adsorbed on carbon nanotubes by using optimization and parallel tempering Monte Carlo. The results show that CO_2 molecules adsorbed in the groove sites of single walled carbon nanotubes display behavior that is quasi-1-dimensional. At finite coverages of CO_2 in grooves clusters containing only odd numbers of molecules are formed at low temperatures. Even numbers of molecules form two clusters, each containing an odd number of molecules.

We have carried out density functional theory studies on the catalytic properties of metal surfaces. We investigated adsorption of CO on the Ag(110) surface and CO adsorption, diffusion and dissociation on the W(111) surface. The CO molecule is found to non-dissociatively adsorb in end-on configurations (α states) and dissociatively absorb in inclined configurations (β states). The dissociation of β state CO is found to have an activation energy of about 0.8 eV, which is lower than the energy required to desorb CO molecularly from the surface.

We have also studied the tungsten difussion mechanisms in cobalt. Our calculations indicate that the diffusion is vacancy mediated. Therefore, we proposed the triangle and quadrangle mechanims, and examined the full diffusion pathways.

PREFACE

I am very thankful to my advisor, Dr. J. Karl Johnson, for training, mentoring and providing opportunities to me during the past four years. His guidance, inspiration, encouragement, and wise and thoughtful discourses have laid the foundation for my Ph. D.. I am also grateful for his kind concern and help beyond my study. I learned a lot from both his academic excellence and character nobleness.

I would like to thank National Energy Technology Laboratory for support of my work. I am very much indebted to the immense help and encouragement from my group colleagues.

TABLE OF CONTENTS

LIST OF TABLES

LIST OF FIGURES

1.0 INTRODUCTION

1.1 STUDY OF ADSORPTION BY COMPUTER SIMULATION

Adsorption is a very important process in industial applications. It is widely applied in pharmaceutical, catalytic, separation industries. However, the design of adsorbents and adsorption processes is still quite empirical because the molecular or atomistic level understanding of the adsorption phenomena is limited.

Classical molecular simulations (e.g. grand canonical Monte Carlo simulation) have been widely performed to study the various adsorption processes such as gas adsorption on graphite surfaces and carbon nanopores,[1] and gas adsorption on metal or metal oxide surfaces. These simulation methods have been proven to be capable of providing reliable results for well-defined systems, and even some experimentally inaccessible properties.

Recently, more and more attention has been drawn to the simulation of adsorption on carbon nanotubes. [2, 3] The interest is invoked mainly by the great potential of carbon nanotubes being used as adsorbent for hydrogen storage.

Simulation of gas adsorption on noble metal surfaces is a classic topic in first principle calculations. There are many calculations dealing with carbon monoxide adsorption on metal or metal oxide surfaces because of its importance in industial catalysis.[4] These first principles calculations can give detailed description of the electronic structure of the system, binding, bonding and adsorption mechanism.

Recently, some experiments showed that metal carbides are very promising substitutes for the noble metals owing to their good catalytic activity, abundant availability and cheap prices.[5, 6] There are relatively few theoretical studies dealing with gas adsorption on these carbide surfaces.

1.2 CARBON NANOTUBES

The discovery of carbon nanotubes by Iijima in 1991 has opened a brand new research field.[7] It invokes not only industial interests but also academic attentions. A carbon nanotube is a member of the fullerene family. Typical dimensions of carbon nanotubes are 0.5 to 1.5 nm in diameter. Their lengths range from nanometers to centimeters. The ends of the tube are capped with fullerene-like hemispherical caps, which can be removed by oxidization processes. Single-walled carbon nanotubes (SWNTs) have great potential in catalysis, gas storage, and other applications owing to their large surface areas and pore properties.

Recently, a great deal of attention has been given to the one dimensional behavior of gas adsorbed in carbon nanotubes.[8, 9, 10] The confinement of particles adsorbed in the endohedral, interstitial channel and groove sites offers the possibility of experimental or theoretical realization of quasi-one-dimensional systems. A growing literature of experiments and simulations has focused on the study of spherical or nearly spherical molecules adsorbed in SWNTs.

1.3 DENSITY FUNCTIONAL THEORY

Density functional theory (DFT)[11, 12] is a very successful approach for the description of ground state properties. It is widely applied in not only standard bulk materials calculations but also in calculation of surface science and complex materials such as carbon nanotubes.

The basic idea of DFT was proposed by Hohenberg and Kohn [12]in 1964 that the ground state energy and other properties of a systems are uniquely determined by the electron density. This is also expressed by stating that the enery, E, is a unique functional of electron density $\rho(\mathrm{r})$. The energy functional is written as a sum of interaction of eletrons with nuclei, the kinetic energy, the electron-electron coulombic energy, and the so-called exchange-correlation potentials.

In pratice, the accuracy of DFT relies heavily on the approximations for the exchange-correlation potential. The exchange-correlation potential accounts for the effects of the Pauli

principle and the Coulomb potential beyond the pure electrostatic interaction of electrons due to the correlation. If we can find the exact exchange-correlation potential, it means that we can solve the many-body problem exactly. However, we do not even know the form of the exact exchange-correlation functional.

There are two kinds of common approximations for the exchange-correlation potentials. The first one is the so-called local density approximation (LDA), which is based on the uniform eletron gas model. The LDA functional has been shown to be inadquate for some problems. Therefore, extension beyond LDA and better approximations, i.e. gradient-corrected functionals have been developed. A variety of gradient corrections have been proposed in the literature.

1.4   MICROWAVE PROCESSING OF MATERIALS

Microwave sintered tools are known to have much better material properties than conventional pressure/temperature sintered tools.[13, 14] For example, microwave sintered tungsten carbide drill bits out perform conventionally sintered parts.[13] Also, polycrystalline diamonds can be directly incorporated into tungsten carbide drill bits through single-step microwave sintering. However, the origin of the differences between microwave and conventional processing is not known to any satisfactory degree. Multiple approaches are needed to fully understand the phenomena associated with microwave processing. Experimental and empirical investigations are being performed by Agrawal and coworkers at Penn State.[14] Complementary modeling is needed to arrive at a phenomenological and complete description of microwave processing. Modeling at the meso-scale and continuum levels are needed to address issues of grain growth and macroscopic structure. Atomic-level details are needed to understand interfacial and diffusion issues. Our work is focused on fundamental first-principles atomic calculations on diffusion and mobility of thermally and microwave processed materials.

Thermal sintering of WC/Co green parts requires long sintering cycles and results in unwanted grain growth. In contrast, microwave sintering of WC/Co green parts takes place in

a short amount of time with very little grain growth. This phenomenon is not expected and understood quite well. It has also been observed that the composition of the Co phase is strikingly different depending on whether the material was thermally or microwave processed.[15] The thermally processed materials have Co phases containing about 20 wt% W, which is exactly the eutectic compositions of the Co/W melt at about 1500 K. In contrast, microwave processed WC/Co materials have Co phases with virtually no W dissolved in the Co binder. The reason for this composition difference is not clear. We propose to initiate a study of the transport of W in the Co binder phase, as a first step in understanding the difference between thermally and microwave processed materials.

2.0 ADSORPTION OF CF$_4$ ON INTERNAL AND EXTERNAL WALLS OF OPENED SINGLE WALLED CARBON NANOTUBES – A VIBRATIONAL SPECTROSCOPY STUDY

The contents of this chapter were taken from Byl, O., Kondratyuk, P., Forth, S., FitzGerald, S., Yates, J.T. Jr., Chen, L. and Johnson, J.K.,*J. Am. Chem. Soc.* **125**, 5889,(2003). The experimental work in section 2.2 was performed by Oleg Byl and co-workers. The simulation work in section 2.3 was performed by myself.

2.1 INTRODUCTION

Since the discovery of single walled carbon nanotubes (SWNTs) by Iijima [7] and by Bethune et al. [16] in 1993 there has been a large interest in their application as sorbents.[17, 18, 19] This is due to the deep potential energy well for adsorption in the interior of the nanotube.[20, 21, 22] The synthesis of SWNTs normally produces closed structures where each tube is terminated by an end cap, which prevents adsorption within the interior. Oxidative chemical treatments [23] must be applied to the closed SWNTs to open the end caps in order to access the interior of the nanotubes.[24] While oxidation in solution [HNO$_3$ + H$_2$O$_2$ + H$_2$SO$_4$] has been found to be effective for opening closed SWNTs, we have developed a gas phase ozone oxidation process, which is easily controlled. This O$_3$-oxidation procedure has been extensively investigated by IR spectroscopy in previous studies.[25, 26] Oxidation can remove the end caps of individual SWNTs as well as producing or enlarging vacancy defects on the nanotube walls. Both carbonyl groups and C-O-C functional groups are known to form at the rims and at defective wall sites by oxidation.[24, 27] Heating to 773-1073 K removes

these blocking groups (by evolution of CO and CO_2 [28]) leaving open entry ports for gas adsorption into the interior.[27].

Adsorption in the interior of a nanotube may be accompanied by adsorption on the exterior surface under appropriate conditions of temperature and pressure[17, 21, 10, 29]. This paper provides the first experimental detection of adsorbed molecules on both the interior and exterior sites on opened SWNTs as well as a method for selective displacement of the internally-bound adsorbed molecules. This has been done by working at cryogenic temperatures and observing the adsorbed probe molecule by transmission infrared spectroscopy. It has been found that the vibrational mode observed is red shifted due to interaction with the nanotube surface. The red shift for interior molecules is larger than the shift for exterior adsorbed molecules.

Confinement of CF_4 in pseudo-one-dimensional condensed structures inside the (10,10) nanotube used here does not result in the production of LO and TO lattice modes observed in 3D clusters of CF_4.

We have employed CF_4(g) as a probe molecule for adsorption on opened single walled nanotubes.[17, 10] CF_4 exhibits an intense triply degenerate asymmetric stretching mode at 1282 cm^{-1}.[30] Its almost spherical shape and polarizability [3.84 Å^3] are similar to that of Xe [4.04 Å^3], which was used in earlier experiments.[20, 24, 28, 27] The similar properties of CF_4 and Xe make them ideal for interesting adsorbed CF_4 displacement experiments to be reported in this work.

2.2   EXPERIMENTAL

2.2.1   Single Walled Carbon Nanotubes

The SWNTs obtained from Professor R. Smalley's group, Rice University, Houston TX were produced by means of the pulsed laser vaporization technique. The raw material was purified by HNO_3/H_2SO_4 treatment. This technique is used to remove foreign carbon impurities and produces oxidized C=O and C-O-C functionalities on the rims and on defect sites in the walls of the SWNTs. These functional groups have been shown to block physical adsorption

into the interior of SWNTs and the groups must be removed by heating to ~873 K in order to open the entry ports for adsorption.[27] The tube diameter distribution was centered near that of (10,10) SWNTs with a diameter of 13.6Å, The length distribution was rather narrow with the most probable length of 320 nm. The purified SWNTs are observed by SEM to form long bundles. This material was identical to that used in previous studies.[28, 27] The purified sample of nanotubes was suspended in dimethylformamide (DMF). About 25 μg of SWNTs was used for this study that gave 75 μg/cm^2 surface density of the sample.

2.2.2 Vacuum System and IR Cell

The stainless steel vacuum system is equipped with a 60 L/s turbomolecular and a 20 L/s ion pump. The pressure was measured with an ionization gauge ($10^{-10} - 10^{-4}$ Torr range) and a capacitance manometer ($10^{-3} - 10^3$ Torr range). The system base pressure was 10^{-7} Torr after 20 hours of baking out at 430-455 K. A UTI 100C quadrupole mass spectrometer was used for leak checking and monitoring of the gas composition in the system.

Figure 1 shows the cell used for transmission IR studies. The cell is connected directly to the gas line and was described in detail previously. The SWNT sample is supported on the surface of a CaF$_2$ spot produced from CaF$_2$ powder hydraulically pressed at 15 000 psi into a tungsten sample support grid. A second CaF$_2$ spot is used as the reference. The grid is stretched between nickel clamps, which are electrically and thermally connected to copper power leads that enter the cell through a l-N$_2$ cooled reentrant dewar. The grid temperature range is 90 K to ~1500 K. Temperature is measured with a type K thermocouple spot-welded to the top of the grid. Thermal control is accomplished electronically using LabView software, permitting accurate temperature programming as well as temperature stability to $\pm$0.1 K at the temperature of 133 K, the adsorption temperature employed in this work.

When there is an equilibrium pressure of CF$_4$ in the cell (mTorr range), slight warming of the sample by thermal conduction through the gas phase occurs. This warming effect is automatically compensated by a slight reduction in heating power to the grid, achieving excellent temperature regulation. A temperature gradient in the gas phase results in a slight gas density gradient as one moves vertically along the sample support grid. Thus, subtraction
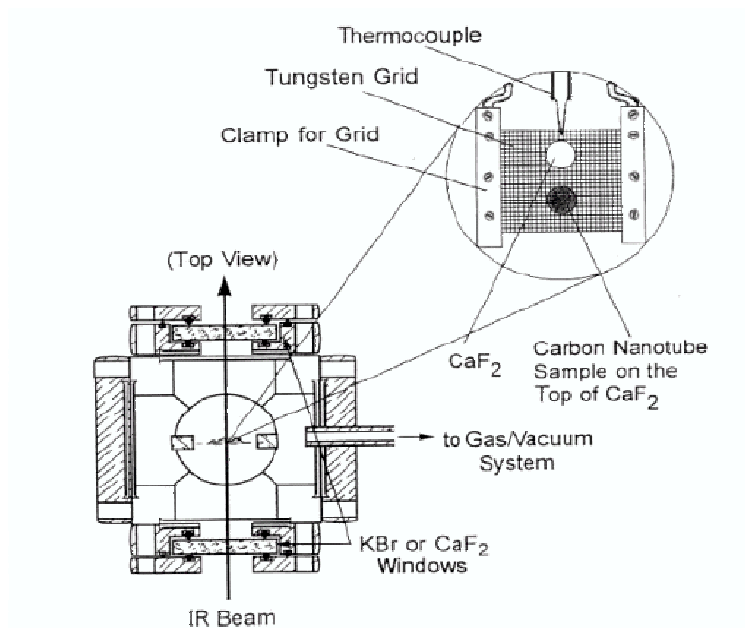
Figure 1: Transmission IR cell-cross-section. The cell is moved by means of horizontal and vertical Newport linear activators allowing precise allignment of the IR beam onto desired section of the sample grid.

of the gas phase spectrum (in comparing sample to reference spectra) is not perfect and a small gas phase CF_4 IR peak at 1282 cm^{-1} results as well as a small contribution at 1297 cm^{-1} (shoulder) and at 1224 cm^{-1} (shoulder) from CF_4 adsorption on CaF_2.

Condensation of CF_4 occurs on the reentrant dewar (dewar temperature = 77 K) resulting in an equilibrium vapor pressure of $CF_4 = 3.3 \times 10^{-2}$ Torr. This is therefore an upper limit of the gas pressure in this experiment. Lower CF_4 adsorption pressures may be achieved by controlled dosing of small quantities of CF_4 gas into the cooled cell.

2.2.3 FTIR Measurements

Transmission IR spectra were measured with a Mattson Research Series FTIR spectrometer controlled from a PC. The spectrometer operates in the mid-infrared spectral region from 500 to 4000 cm^{-1} and uses a wide band MCT detector. All spectra were recorded at 4 cm^{-1} resolution with 500 scans for averaging. The support grid holding the SWNT sample in the adsorption cell could be accurately positioned horizontally and vertically (to ± 1 μm) in the IR sample compartment using computer controlled drivers. IR spectra were recorded as follows: (1) SWNTs on a CaF_2 support; (2) CaF_2 support; (3) gas phase thorough the empty grid. In each case spectra were ratioed to background spectra taken without CF_4 in the system.

Prior to each adsorption experiment a background set of spectra was measured. Upon adsorption of CF_4 a second set of spectra was measured and ratioed to the background. Then appropriate differences were taken in order to obtain the spectrum of CF_4 adsorbed on the SWNT sample.

2.2.4 Controlled Oxidation Using Ozone

The SWNT sample was heated in vacuum to 873 K to remove the majority of the oxidized surface functionalities produced by the HNO_3/H_2SO_4 purification process and was then subjected to a series of O_3 exposures, followed by annealing to 873 K in vacuum. This cyclic oxidation/annealing procedure has previously been found to open the SWNTs caps completely and to enhance the adsorption kinetics into the nanotube interior by opening

sites on the nanotube walls and rims.[23, 24, 25, 28, 27] The cyclic procedure causes etching of the SWNT sample, and samples so treated are designated as etched.

High purity O_3 was prepared and purified in an all glass generator described previously.[31] We have found that O_3 prepared in this manner will partially decompose upon admission to a stainless steel vacuum system. This effect may be minimized by prolonged passivation of the stainless steel surface with O_3 at $\cong$10 Torr pressure. For the experiment shown here, the O_3 treatment was carried out at room temperature in three stages: Stage 1: 30 min at 8 Torr, 298 K; Stage 2: 19 hr at 14.3 Torr, 298 K; Stage 3: 18 hr at 15.5 Torr, 298 K. As we will show, initial ozonization produced functional groups at the entrance to the tubes, thus blocking adsorption of CF_4 into the interior of SWNTs in agreement with previous Xe adsorption studies.[24, 28] The SWNTs were then opened by removal of the blocking functional groups through heating to 873 K in vacuum for 30 minutes. This greatly enhanced the ability of the SWNTs to adsorb CF_4.

2.2.5   Xe Displacement Experiment

We employed Xe to preferentially displace adsorbed CF_4 from the nanotube interior. This was done by filling the nanotubes with CF_4 at 3.3×10^{-2} Torr and 133 K. Xe was then added in sequential doses and the IR spectra of the adsorbed CF_4 were recorded.

2.2.6   Gases

CF_4 (99.9% purity) was obtained in a cylinder from Aldrich Chemical Co. and was used without further purification. Xe (99.995%) was obtained from Matheson in a cylinder and was used without further purification.

2.3   SIMULATION METHODS

2.3.1   Vibrational Calculations

The vibrational shifts due to adsorption have been investigated theoretically through quantum calculations using the Gaussian 98 software package. Gas phase spectra of CF_4 were computed at the levels of LDA theory with the 6-31G basis set. The calculated ν_3-asymmetric stretching mode and ν_4-deformation mode frequencies are 1264 cm^{-1} and 572 cm^{-1}, respectively. Quantitative agreement between spectra calculated from LDA and experiment is not expected since LDA does not accurately account for electron exchange, which would account for much of the binding energy. We are also limited in accuracy by the size of the model nanotube and the size of the basis set we were able to use. The LDA calculations of CF_4 adsorbed in the model nanotube gave the average frequencies for the ν_3 mode and ν_4 mode of 1246 cm^{-1} and 571 cm^{-1}, respectively. We have chosen to use a relatively small basis set (6-31G) in order to make the CF_4-nanotube calculations tractable. The CF_4-nanotube system was modeled by using a small cluster to represent the nanotube. We used three unit cells of a (9,9) SWNT, split the nanotube in half (along the plane of the nanotube axis), and terminated the dangling bonds with hydrogen atoms. The model nanotube fragment contained 40 carbon and 20 hydrogen atoms. The CF_4 molecule was placed a distance of several angstroms from the concave (inside) surface of the nanotube and the position of the CF_4 molecule was optimized, holding the atoms in the nanotube fixed. Once the optimized geometry was found we computed the vibrational spectrum. The optimization and frequency calculations were performed at the LDA/6-31G level of theory.

2.3.2   Adsorption Calculations

We have computed the equilibrium amounts of CF_4 and Xe adsorbed on carbon nanotube bundles as a function of Xe partial pressure from molecular simulations. The Grand canonical ensemble (constant μVT) Monte Carlo (GCMC) method [32] was used to calculate adsorption isotherms. The GCMC algorithm consists of three types of moves, namely, translation of a single molecule, creation of a new molecule in the simulation cell, and deletion

of a molecule. Moves were attempted randomly with probability 0.2 for translation and 0.4 each for creation and deletion. Simulations were typically equilibrated for 2 million moves, followed by data taking for 1 million moves. The maximum displacement step size was adjusted during equilibration to achieve approximately a 40% acceptance ratio for translations. We have used the Lennard-Jones (LJ) potential to account for all fluid-fluid and fluid-solid interactions. Parameters for Xe were taken from the literature.[33] The CF_4 molecule was treated as a single spherical particle. The LJ parameters were derived from viscosity data and were previously used in molecular simulations of diffusion in zeolites.[34] The carbon parameters were taken from Steele.[35] Lorentz-Berthelot combining rules were used for the cross interactions. The LJ potential parameters are given in Table 1 where σ is the molecule diameter in Å and ε is the potential well depth such that ε/k is in units of K, where k is the Boltzmann constant. The use of classical potentials to model the nanotube-fluid interactions precludes the modeling of electronic effects, such as the differences between metallic and non-metallic nanotubes.

Table 1: Lennard-Jones potential parameters used in the simulations

	Xe-Xe	CF_4- CF_4	C-C
σ (Å)	4.1	4.66	3.4
ε/k (K)	222.32	134.0	28.0

Three different nanotube bundles were considered in this work. Two bundles were constructed by randomly placing nanotubes of various diameters in a box and then optimizing the spacing between the nanotubes as described by Simonyan and Johnson.[20] Each of these two bundles contained 18 nanotubes. The third bundle was a perfect 3×3 array of (10,10) nanotubes. The numbers of each type of nanotube in each bundle are given in Table 2. Using the nomenclature of Table 2, bundles 1 and 2 are representative of heterogeneous bundles, i.e., bundles with a heterogeneous distribution of nanotube diameters. Bundle 3 is a homogeneous bundle since all nanotubes have the same diameter. Experimentally produced nanotubes are heterogeneous. Comparison of simulations on these two classes of bundles will serve to characterize any qualitative differences between adsorption on homogeneous

and heterogeneous bundles. Smoothed potentials were used for the nanotubes in the bundles in order to increase the simulation efficiency. See ref.[20] for details of the smoothing procedure. We have found that smoothing the potential has no effect on the adsorption isotherms.[20] The nanotubes in the simulation cell were all aligned in the z direction and the lengths of the nanotubes were about 61 Å. The bundle was placed in a parallelepiped simulation cell that was 200 Å on a side in the x and y directions. Periodic boundary conditions were applied in all directions and the potential cutoff was set to 25 Å. The size of the cell in the x and y directions was large enough so that the bundle was isolated (no periodic image interactions).

Table 2: Number and types of nanotubes used in the three different bundles

Bundle	Number of (8,8) tubes	Number of (9,9) tubes	Number of (10,10) tubes	Number of (11,11) tubes	Number of (12,12) tubes	Average Nanotube Diameter (Å)
1	2	2	10	2	2	13.56
2	4	10	2	2	0	12.35
3	0	0	9	0	0	13.56

2.4 RESULTS

2.4.1 Development of CF$_4$-IR Spectrum upon SWNT Etching by O$_3$

Figure 2 shows a typical set of IR spectra obtained in these measurements and the results of taking appropriate differences to derive the IR spectrum of CF$_4$ adsorbed on the SWNT sample. The CaF$_2$ support exhibits a significant contribution to the composite IR spectrum due to CF$_4$ adsorption on its surface, as seen in spectrum (b). Additional IR absorbance due to CF$_4$ is observed for the SWNT sample, supported on CaF$_2$, as shown in spectrum (a). Subtraction leads to spectrum (c), where contributions from adsorbed CF$_4$ on the SWNT sample are observed, along with small features due to incompletely compensated gas phase CF$_4$. The prominent uncompensated gas phase spectral feature is shown as a dashed peak centered at 1282 cm^{-1}.
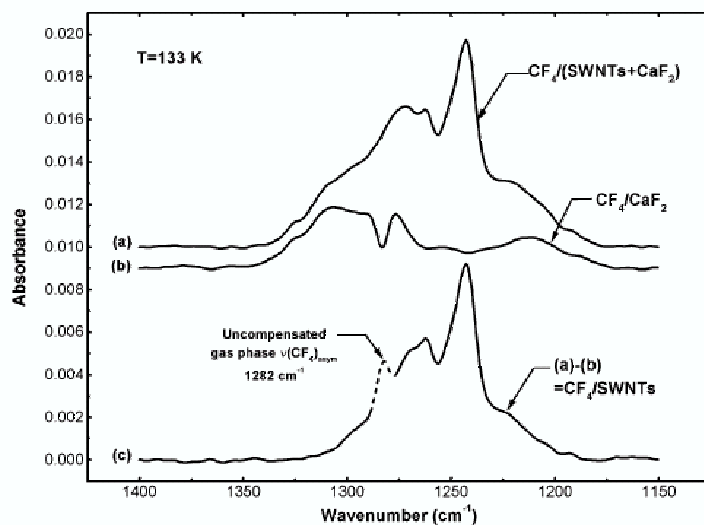
Figure 2: Procedure for spectral subtraction for CF_4 adsorbed at 133 K and 3.3×10^{-2} Torr.

Figure 3 shows the infrared spectrum of adsorbed CF_4 as increasing amounts of etching take place through repeated exposures to O_3, followed by heating. Three etch cycles are presented. As the etching proceeds, enhanced IR intensity due to adsorbed CF_4 is observed to occur at frequencies below 1275 cm^{-1}.

Figure 4 shows a comparison of the development of the IR spectrum of CF_4 for increasing coverage on the SWNT sample before etching by O_3 and after three cycles of etching. Note that the absorbance scales differ by a factor of two for the spectral presentations. The spectra show the effects of increasing equilibrium pressures of CF_4, established at a sample temperature of 133 K. The spectra shown in Fig. 4A for the unetched SWNTs contain only two prominent spectral features for adsorbed CF_4 at 1272 cm^{-1} and 1253 cm^{-1}. For the etched SWNT sample (Fig. 4B), in addition to the spectral features observed in Fig. 4A, an additional pair of absorption bands are observed at 1262 cm^{-1} and 1242 cm^{-1}. As will be discussed later, the pairs of bands observed at different frequencies for the unetched and etched nanotubes are due to the Fermi resonance of the strong infrared-active ν_3 mode and the first overtone of the ν_4 mode, designated $2\nu_4$

14
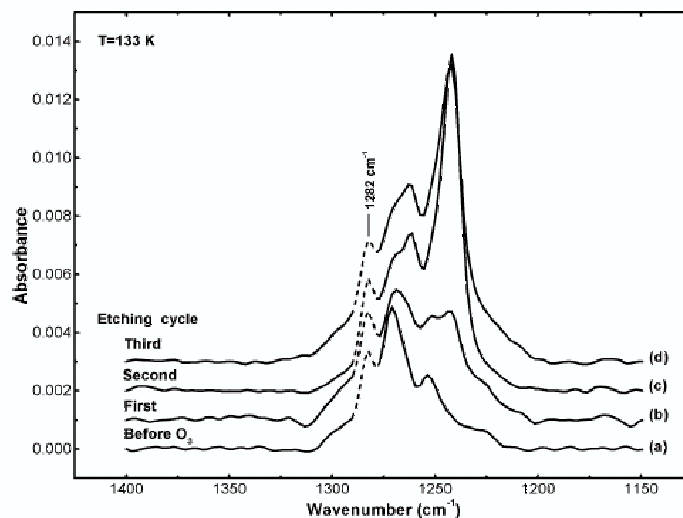
Figure 3: Development of CF$_4$ IR spectra during cycles of O$_3$-induced oxidation followed by heating to 873 K for 30 min in vacuum. P$_{CF4}$=3.3 $\times$ 10^{-2} Torr.

2.4.2 Displacement of Adsorbed CF$_4$ by Xe

The resolution of the overlapping CF$_4$ spectral features has been experimentally confirmed through the displacement of CF$_4$ by Xe. Figure 5 shows a high coverage spectrum of CF$_4$ obtained for the etched SWNT sample. Exposure to Xe at 133 K results in the selective disappearance of two IR bands together at 1262 cm^{-1} and 1242 cm^{-1}. In contrast, the species responsible for the two bands at 1272 cm^{-1} and 1253 cm^{-1} are either not displaced or are more slowly displaced compared to the former band pair. We assign the two bands at 1262 cm^{-1} and 1242 cm^{-1}to CF$_4$ adsorbed in the interior of the etched SWNT sample, and the two bands at 1272 cm^{-1} and 1253 cm^{-1} to CF$_4$ species adsorbed externally on the outer SWNT surface. By varying the sequence of Xe and CF$_4$ adsorption, it was found that the spectra represent identical equilibrium conditions achieved by gas adsorption in either sequence.

15
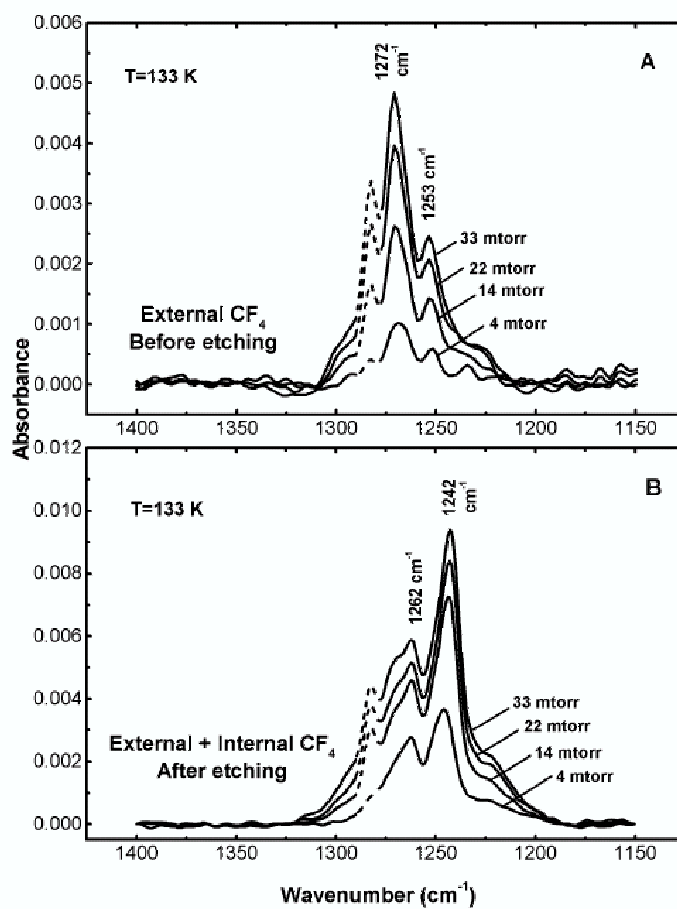
Figure 4: Development of CF$_4$-IR spectra for (A) external sites; and (B) for external + internal sites.
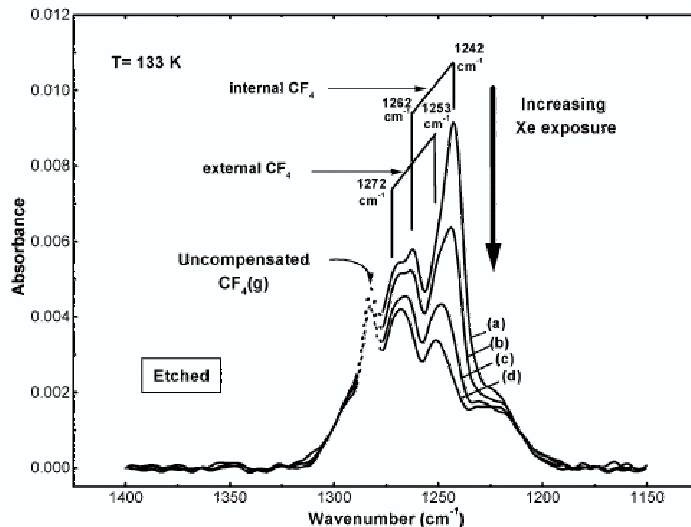
Figure 5: Xe displacement of adsorbed CF_4. Equilibrium Xe pressure was less than 10^{-3} Torr for (a)-(d). The equilibrium P_{CF_4}=3.3 × 10^{-2} Torr for all spectra.

2.5   DISCUSSION

2.5.1   Absence of LO-TO splitting in IR spectra of CF_4 on SWNTs.

The ν_3 mode in CF_4 has an exceptionally high infrared intensity [30]. This gives rise to a strong transition dipole – transition dipole coupling between ν_3 modes of different CF_4 molecules. As a result longitudinal – transverse optical (LO-TO) splitting appears in the infrared spectra at high volumetric concentrations of oscillators. The splitting is strongly dependent on the arrangement of the oscillators. We have not observed LO-TO splitting in this work implying that the concentration of CF_4 molecules inside of and on the exterior of the SWNT sample is not sufficiently bulk-like to promote lattice mode production.

Figure 6A shows the LO-TO mode splitting evolution in the Raman spectra of CF_4 in an Ar matrix at 84.5 K taken as an example from the work of P. Nextoux *et al.* [36]. More examples of LO-TO splitting in the vibrational spectra of CF_4 in the condensed phase can be found elsewhere.[37, 38, 39] At a very low concentration of CF_4, spectrum (a), two peaks at 1272 cm^{-1} and 1257 cm^{-1}caused by the Fermi resonance interaction of ν_3 and $2\nu_4$ are

observed. The LO-TO splitting is very small in this case and reported to be 1.4 cm^{-1}. In pure condensed CF$_4$, spectrum f, LO-TO splitting reaches 75.0 cm^{-1} with the LO band at 1320 cm^{-1} and TO band at 1245 cm^{-1}.
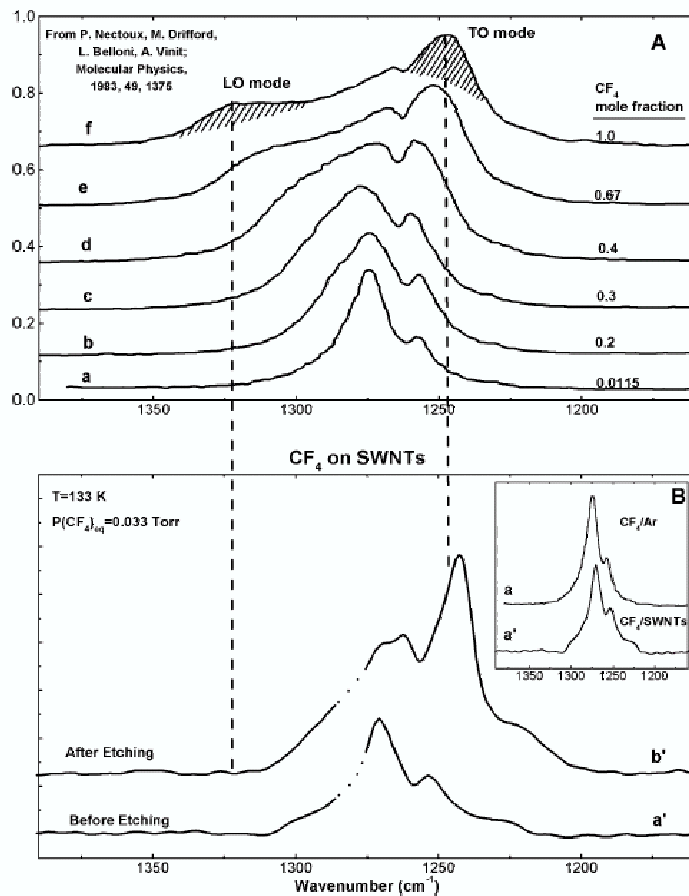
Figure 6: (A). LO-TO splitting evolution in Raman spectra of CF$_4$ in an Ar matrix at 84.5 K with increasing concentration; (B). Spectra of CF$_4$ adsorbed at 133 K and 0.033 Torr on unetched and etched SWNTs.

Figure 6B shows the spectrum of CF$_4$ adsorbed on unetched and etched nanotubes. The close similarity of the IR spectrum of CF$_4$ adsorbed on SWNTs before etching to the Raman spectra of CF$_4$ in an Ar matrix at the lowest concentration (see inset in Figure 6B) implies that there is a similarly negligible amount of LO-TO splitting in the spectra of CF$_4$ adsorbed on the external surface of nanotubes at these conditions. No evidence for LO or TO modes can be seen.

As the nanotubes are etched the internal surface becomes accessible for adsorption. The IR spectra of CF_4 adsorbed on the etched SWNTs (Figure 6B, upper spectrum) contain features from both the external and the internal CF_4. Although the amount of CF_4 adsorbed has increased somewhat compared to unetched nanotubes, the LO mode is not seen and the peak at 1242 cm^{-1} can not be considered to be the TO band because of its sharpness.

Thus the mean size of adsorbed CF_4 ensembles on the inner and outer surface of the SWNTs must be too small to produce the LO-TO modes characteristic of the condensed phase.

2.5.2 Spectra of CF_4 adsorbed on SWNTs.

In vibrational spectroscopy, perturbations between a fundamental and an overtone are frequently encountered, and are known as Fermi resonances [40]. In the case of the CF_4 molecule, the Fermi resonance between the ν_3 mode and the first overtone of the ν_4 mode ($2\nu_4$) has been observed in a number of studies.[41, 42, 43, 44, 45] As a result of the interaction the overtone, usually very weak, borrows intensity from the fundamental band and becomes visible, and at the same time the two bands are shifted further apart. Thus the presence of a Fermi resonance complicates the appearance of the spectrum, so it is often useful to extract the "unperturbed" positions and intensities of the peaks. This was done in the present study in a way similar to that employed in ref.[40] For the spectra of CF_4 on etched and unetched nanotubes, Lorentzian-shaped profiles of v$_3$ and $2\nu_4$ were found that upon numerically calculating the Fermi resonance interaction gave the best fits to the spectra observed.

Figure 7(A) shows the spectrum of CF_4 on unetched nanotubes, which corresponds to CF_4 adsorbed on the outer surface of nanotubes, and the Lorentzian profiles found for the ν_3 and the $2\nu_4$ energy level distributions. The fit calculated from these distributions approximates the experimental data well. The presence of the $2\nu_4$ energy level redistributes the intensity of ν_3 in the spectrum creating an additional feature at 1253 cm^{-1} and a "hole" (sometimes referred to as Evans hole in the literature) at 1257 cm^{-1}. Note that for CF_4 molecules bound to the SWNTs exterior, the ν_3 level is located to the higher frequency side of $2\nu_4$.

CF$_4$ on etched nanotubes should be adsorbed both on the outer surface and the inner surface, made accessible by the etching, whereas the spectrum for unetched nanotubes only contains the contribution from the outer CF$_4$. To find the spectrum of only the inner CF$_4$ one thus needs to subtract the spectrum for the unetched nanotubes from the spectrum for the etched nanotubes. As some of the SWNT surface is destroyed in the process of etching with ozone, the spectrum from the unetched nanotubes has to be multiplied by a coefficient smaller than 1 before the subtraction is carried out. We used a value of 0.75, chosen based on the goodness of the fit to the resulting spectrum. It corresponds to the destruction of 25% of the outer surface during ozonation. Figure 7(B) shows the spectrum of CF$_4$ adsorbed on the inner surface of nanotubes resulting from this subtraction and the Lorentzian distributions of ν_3 and $2\nu_4$ that give the best fit to the data. The most striking difference when compared to the external CF$_4$ distributions (Figure 7A, bottom) is that ν_3 shifts by 20 cm^{-1} to the red (now ν_3 is to the lower energy side of $2\nu_4$), whereas $2\nu_4$ does not change its position. The reason for the shift of ν_3 is the stronger interaction of the molecule with the surface when it is adsorbed in the interior of the nanotube. The LDA calculation also shows that the ν_3 band is much more prone to shift when the molecule's environment changes, than the $2\nu_4$ mode (as judged from the ν_4 fundamental). The calculation indicates that for the CF$_4$ molecule adsorbed in the interior of the nanotube, the ν_3 mode shifts by about -20 cm^{-1} compared to the gas phase, whereas the shift for ν_4 is only -2 cm^{-1} corresponding to a $2\nu_4$ shift of about -4 cm^{-1}.

This analysis of the experimental spectra shows that the shift for the ν_3-mode of CF$_4$ compared to gas phase CF$_4$ is -15 cm^{-1} for CF$_4$ molecules bound to the nanotube outer surface and -35 cm^{-1} for CF$_4$ molecules bound in the interior.

Figure 8 shows the addition of the fits for the external and internal CF$_4$ spectra, resulting in a fit for the total composite spectrum of CF$_4$ adsorbed on etched nanotubes. The coefficient of 0.75 is employed during addition.

The shift of the ν_3 mode to lower wavenumbers is in accordance with the redshift often observed for physically adsorbed species and for species bound inside of inert matrixes. The band associated with the smaller ν_3 wavenumber shift to the red is assigned to externally-bound CF$_4$ molecules on this basis, and the band associated with the larger wavenumber
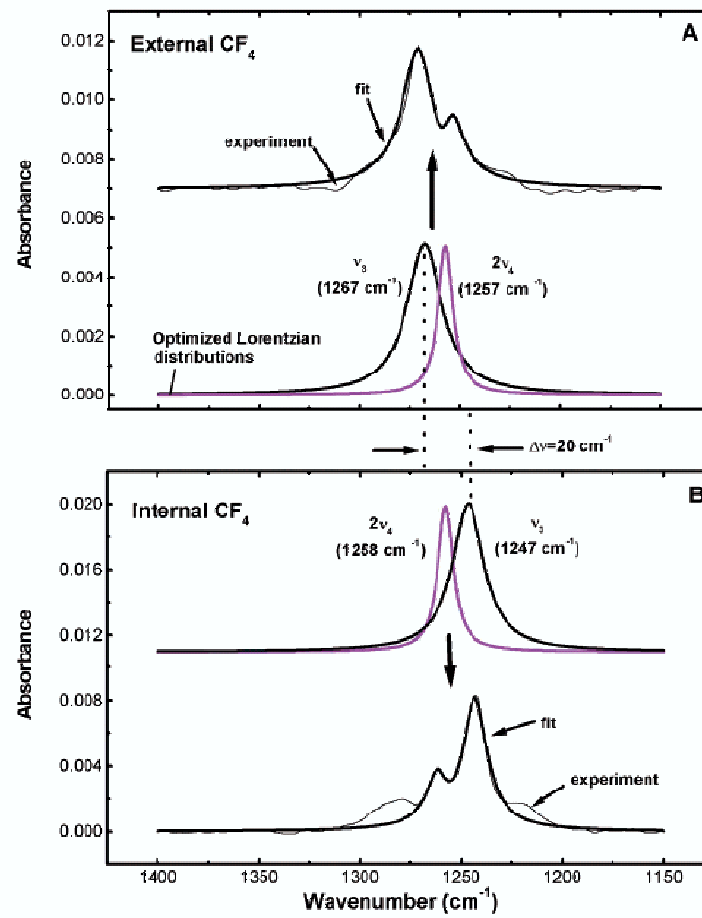
Figure 7: Convolution of fundamental ν_3 mode with Fermi resonance $2\nu_4$ mode for external and internal CF_4 species on SWNTs.

21
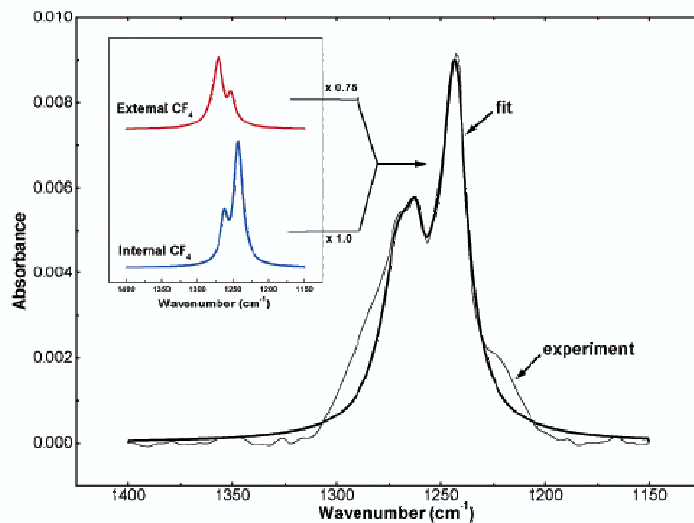
Figure 8. Simulation of combined external and internal CF₄ spectra on SWNTs.

Figure 8: Simulation of combined of external and internal CF_4 spectra on SWNTs.

shift is assigned to internally-bound CF_4, where the interaction would be expected to be larger.

2.5.3 Modeling of Xe Displacement of Adsorbed CF_4 from SWNTs

The displacement of CF_4 by Xe confirms the presence of four IR bands for the adsorbed CF_4 species present on both the exterior and interior sites. It is seen in Fig. 5 that Xe preferentially displaces internal CF_4 species causing the bands at 1262 cm^{-1} and 1242 cm^{-1} to disappear first as the Xe coverage is increased. The displacement experiments probe the thermodynamic factors responsible for Xe-CF_4 site exchange under equilibrium conditions, since similar infrared spectra are observed for either order of adsorption of CF_4 and Xe. We know that Xe is thermodynamically favored as an internally bound species compared to CF_4, causing preferential CF_4 displacement by Xe from the SWNT interior. We have performed molecular modeling of CF_4 and Xe coadsorption in order to observe whether preferential CF_4 displacement occurs for the internally-bound CF_4 compared to externally bound CF_4. Classical GCMC simulations were performed at 133 K and a constant partial pressure of CF_4

22

of $3.3{\times}10^{-2}$ Torr and various values of Xe partial pressure. Simulations were performed on each of the three model bundles described in Table 2 . Simulations on the three different types of bundles are qualitatively similar. In each case Xe begins to adsorb inside the nanotubes, displacing CF_4, at pressures below where there is appreciable Xe adsorption in the grooves on the external surface of the nanotubes. The partial pressure at which Xe begins to displace internal CF_4 is about 10^{-5} Torr. Xenon starts to adsorb on the outside of the nanotubes at about 10^{-4} Torr for the heterogeneous bundle and about 10^{-3} Torr for the homogeneous bundle. It is interesting to note that even after Xe begins to adsorb on the outside of the nanotubes, very little CF_4 is displaced by the Xe, even at the highest Xe partial pressure simulated (10^{-2} Torr). This observation agrees with the experimental results showing that the CF_4 modes associated with adsorption inside the nanotube disappear in a facile manner, while the IR peaks for external adsorption are not substantially attenuated by Xe adsorption. The reason for this can be easily seen by observing snapshots of the simulation. Figure 9 shows snapshots for adsorption on exterior sites of bundle 3 at Xe partial pressures of 10^{-3} (left) and 5×10^{-3} (right) Torr, both with a CF_4 partial pressure of $3.3{\times}10^{-2}$ Torr. Note that at the lower Xe partial pressure there are a number of CF_4 molecules (shown in red) but only one Xe atom (blue). Note also that CF_4 does not fill all the available external sites at this pressure. Hence, at the higher pressure (right) we observe a dramatic increase in the concentration of Xe atoms in the groove sites, while the number of CF_4 molecules remains almost constant. The first Xe atoms to adsorb onto the external sites simply occupy empty sites rather than replacing CF_4 molecules. At pressures higher than those sampled experimentally, Xe does displace CF_4 on the external sites. This explains why external CF_4 species responsible for the bands at 1272 cm^{-1} and 1253 cm^{-1} persist at all experimental Xe doses.

Molecular simulations show that Xe and CF_4 only adsorb inside the nanotubes and on the external groove of the perfectly packed homogeneous bundles (bundle 3). The interstitial channels in homogeneous bundles of (10,10) nanotubes are too small to allow adsorption of either gas. However, the heterogeneous bundles do not pack perfectly and hence have a few larger interstitial sites for gas adsorption. Simulation snapshots from homogeneous and heterogeneous bundles are shown in Figure 12. Most of the interstitial channels in the
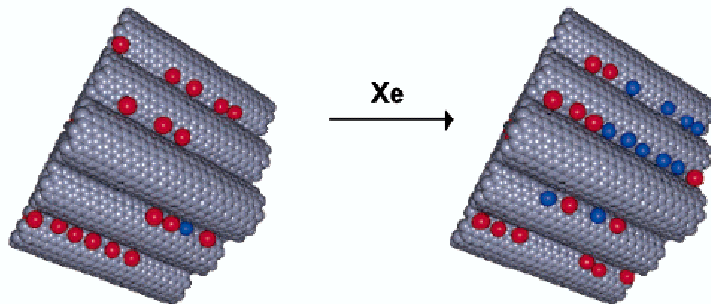
Figure 9: Simulation snapshots for CF_4-Xe coadsorption on the external groove sites at a Xe partial pressure of 10^{-3} Torr (left) and 5×10^{-3} Torr (right). In both cases the CF_4 pressure is 3.3×10^{-2} Torr. Note that the number of Xe atoms (blue) increases dramatically with increasing Xe partial pressure, while the number of CF_4 molecules (red) decreases only slightly.

heterogeneous bundle (left) are too small to accommodate adsorption of either Xe or CF_4. However, there are a few interstices that are large enough to facilitate Xe adsorption, but not CF_4, and other channels that are large enough to accommodate either molecule. This explains why the heterogeneous bundles exhibit external Xe adsorption at lower pressures than the homogeneous bundles. This explains why the heterogeneous bundles (Fig. 10) exhibit external Xe adsorption at lower pressures than the homogeneous bundles (Fig. 11). Adsorption in the interstitial channels is counted as external site adsorption so that the upturn in external Xe site adsorption is a result of Xe inside the interstitial channels. We expect that the nanotube bundles studied experimentally behave more like the heterogeneous bundles than the perfectly packed bundles, giving rise to some interstitial adsorption.

2.6 SUMMARY

The following results have been obtained in our study of CF_4 adsorption on unetched SWNTs and etched SWNTs:
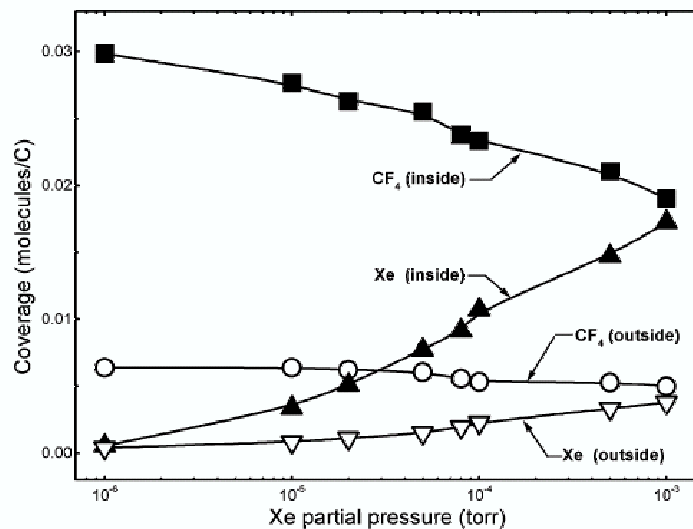
Figure 10: Simulated equilibrium adsorption uptake of CF_4 and Xe (per carbon atom) on heterogeneous nanotube bundle 1 (see Table 2) at 133 K as a function of Xe partial pressure. The CF_4 pressure is held constant at 3.3×10^{-2} Torr. Squares (circles) represent the loading of CF_4 molecules inside (outside) the nanotubes and up triangles (down triangles) represent Xe adsorption inside (outside) the nanotubes. Lines are drawn to guide the eye. The estimated statistical errors are of the order of the symbol sizes.
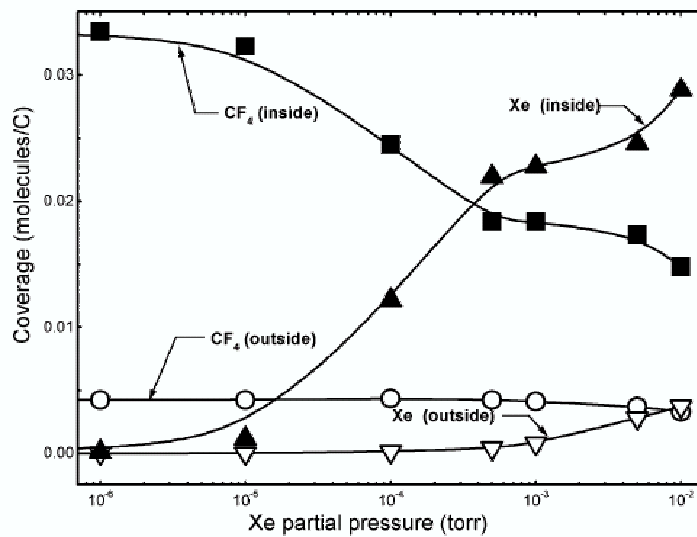
Figure 11: Simulated equilibrium coverage of CF_4 and Xe (expressed per carbon atom) on homogeneous nanotube bundle 3 (see Table 2) at 133 K as a function of Xe partial pressure. The CF_4 pressure is held constant at 3.3×10^{-2} Torr. The symbols are the same as in Fig. 9. The lines are drawn to guide the eye.
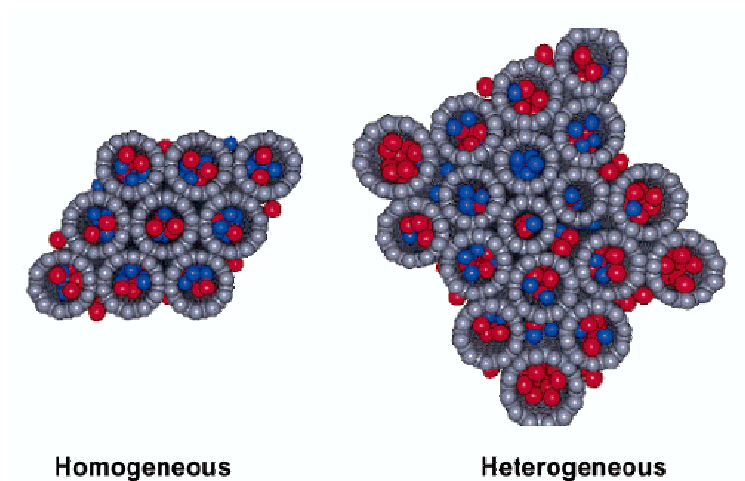
Figure 12: Simulation snapshots for CF_4-Xe coadsorption on homogeneous bundles (left) and on heterogeneous bundles (right). Note that the interstitial channels in the homogeneous bundle are too small to allow adsorption of either Xe or CF_4. The interstitial channels in heterogeneous bundles, such as bundle 1 from Table 2 shown here (right) have some larger interstitial channels that allow adsorption of Xe and CF_4.

1. The adsorption of CF_4 on SWNTs at 133 K occurs on two adsorption sites: internal and external. On closed SWNTs, CF_4 adsorbs only on the external sites, whereas on opened SWNTs, CF_4 adsorbs on both external and internal sites.

2. Adsorbed CF_4 on external sites of SWNTs manifests itself by two IR bands, at 1272 cm^{-1} and 1253 cm^{-1}. CF_4 adsorbed on internal sites exhibits two bands at 1262 cm^{-1} and 1242 cm^{-1}. The presence of two bands in both cases results from the Fermi resonance of the strong infrared-active ν_3 fundamental with the first overtone of the ν_4 mode.

3. The larger shift from the gas phase frequency of the ν_3 mode of internal CF_4 (shift $=-35$ cm^{-1}, -2.7%) compared to the external CF_4 (shift $= -15$ cm^{-1}, -1.2%) is due to the stronger interaction of CF_4 with the interior walls of SWNTs.

4. Xe preferentially displaces CF_4 adsorbed inside of SWNTs as observed both experimentally and in equilibrium simulations.

5. The confinement of CF_4 inside of the (10,10) single walled nanotube in pseudo one-dimensional structures does not result in production of LO and TO lattice modes characteristics of large 3D ensembles of CF_4 in crystallized CF_4.

3.0 DISPLACEMENT OF CO$_2$ BY XE IN SINGLE-WALLED CARBON NANOTUBE BUNDLES

The contents of this chapter were taken from Matranga, C., Chen, L., Bockrath, B. and Johnson, J.K., *Phys. Rev. B* **70**,165416,(2004). The experimental work was performed by Chris Matranga. The simulation work was performed by myself.

3.1 INTRODUCTION

Studying how gases physisorb on single-walled carbon nanotube bundles (SWNTs) not only yields information about the interactions of gases with these materials but can also produce fruitful information about the bundle itself. Knowledge of how gases access endohedral and interstitial sites aids our understanding of the defects present along nanotube sidewalls and on how these nanotubes have crystallized to form bundles. The effects that common purification steps have on access to these sites add another dimension of understanding, because acid oxidation can block sites through the addition of functionalization.

Molecular vibrations are sensitive to their local environment, so infrared studies are useful for differentiating molecules in samples with multiple adsorption sites.[46, 47, 48, 49] In this regard, CO$_2$ is an obvious choice for a probe molecule since its ν_3 asymmetric stretch mode has a large infrared cross section making it easily detectable with a standard FTIR spectrometer. In fact, several experimental and computational studies have appeared for CO$_2$ adsorption in SWNTs, so a fair amount of data exists for this system.[48, 49, 50, 51, 52, 53, 54]

Here, we present a joint experimental and computational study on the displacement of CO$_2$ by Xe in acid purified SWNTs. Both the experiments and simulations show there is a se-

quential displacement of physisorbed CO_2 by Xe with endohedral and interstitial sites preceding groove/external surface sites. Data from the molecular simulations are used to model how the experimental IR intensities should vary during displacement assuming Lorenztian lineshapes with spectroscopic parameters for each site set from previous experiments.[48, 49, 50] The qualitative agreement between these simulated IR spectra and the actual IR experiments is good, suggesting that the sites associated with the IR peak assignments and their intensity variations are adequately represented by the system used in the molecular simulations.

3.2   METHODS

3.2.1   Experimental

Infrared studies in the transmission geometry were performed in a vacuum chamber described previously.[49] The SWNT sample was purchased from Tubes@Rice as a "Purified Grade" suspended in toluene. This sample was produced by the laser ablation technique followed by acid purification [12-14]. Infrared samples were thin films prepared by dispersing the sample directly on a 1 mm thick plane parallel CaF_2 window (Janos Technology) and evaporating the solvent in a 120 °C oven for ~5 minutes. The background absorption of the film was adjusted by adding sample until the film had an optical density of ~ 0.9 near 2300 cm^{-1}. This film thickness gave enough sample path length to allow the observation of physisorbed CO_2 under the pressures and temperatures accessed in this study. Samples were degassed in the vacuum chamber at 373 K for 2 hours prior to use. CO_2 was physisorbed on the sample at 77 K by closing the gate valve between the pumping system and the chamber and backfilling the cell to a static pressure. All reported experimental pressures are uncorrected ion gauge values determined in the main portion of the chamber. After the infrared intensity growth from CO_2 physisorption was saturated with respect to pressure, Xe displacement studies were run by back filling the chamber with Xe to a desired pressure. To test that we were observing equilibrium conditions for the displacement of CO_2 we: i) heat the sample to 300 K (gate valve still closed) after reaching the highest experimental pressure ($P_{Xe} + P_{CO_2}$ ~ 0.8 mTorr); ii) check with IR that CO_2 is completely desorbed from the sample; iii) quench

30

the sample back to 77 K. The cell pressure and the integrated intensity for physisorbed CO_2 return to within ~ 5 and ~ 15 %, respectively, of their values before heating. Furthermore, we see no redistribution of CO_2 intensities from the IR peaks associated with the different adsorption sites.

3.2.2 Computational

Adsorption isotherms were computed from grand canonical Monte Carlo (GCMC) simulations[32]. The GCMC algorithm consists of three types of moves, namely, translation and rotation of a single molecule, creation of a new molecule, and deletion of an existing molecule. Moves were attempted randomly with a 20% probability for translation/rotation and 40% each for creation and deletion. Simulations were typically equilibrated for 5×10^7 moves, followed by data taken for 10^7 moves. The maximum displacement step size was adjusted during equilibration to achieve approximately a 50% acceptance ratio for combined translation and rotation moves. Canonical simulations were used to calculate average energies at a fixed coverage.

The Xe-Xe interaction was modeled as a Lennard-Jones (LJ) potential. The parameters (σ=4.1 Å, $\varepsilon/k = 221$ K) were taken from the literature.[33] The CO_2 and nanotube (carbon) potentials used in this work are the same as that used in our previous work.[49] The CO_2-CO_2 potential was taken from Harris and Yung and includes effective charges to account for the quadrupole moment.[55] The carbon atoms in the nanotube were assumed to have the same potential as carbons in a graphene sheet, with LJ parameters for carbon taken from Steele.[35] Cross interactions were computed from the Lorentz-Berthelot combining rules. We have ignored any charge-related interactions between CO_2 and Xe or nanotubes (such as charge-induced dipole).

We have simulated adsorption and displacement on three different nanotube bundles. Two of the bundles are heterogeneous, i.e., composed of SWNTs of different diameters. The heterogeneous bundles contain packing defects that create large interstitial channels, capable of adsorbing both Xe and CO_2. These bundles are similar to those studied by Shi and Johnson.[2] The third bundle is homogeneous, composed of only (10,10) SWNTs. The

first bundle contains 18 SWNTs, ranging in size from 10.84 to 16.28 Å in diameter. The second bundle contains 25 SWNTs covering the same range of sizes. The homogeneous bundle contains 16 nanotubes. Details of the bundles, including the number of each type of nanotube are given in Table 3. The simulation code includes an algorithm for identifying molecules as being adsorbed in endohedral, interstitial, or external sites. This allows for accurate statistics on the occupation and energetics in these three classes of sites. By conducting simulations on bundles with different packing arrangements, we are able to show that the effects seen are general and not specific to a particular bundle arrangement. A more detailed description of the potential models and construction of nanotube bundles can be found in reference.[49]

Table 3: Classes of Nanotube bundles studied in the molecular simulations in this work. The diameters are 10.84, 12.20, 13.56, 14.92, and 16.28 Å for the (8,8) through (12,12) nanotubes.

Bundle	Number of (8,8) tubes	Number of (9,9) tubes	Number of (10,10) tubes	Number of (11,11) tubes	Number of (12,12) tubes	Average diameter(Å)
1	2	2	10	2	2	13.56
2	3	5	12	3	2	13.54
3	0	0	16	0	0	13.56

Spectral simulations were constructed by summing 3 Lorenztians to produce a lineshape representing the endohedral, interstitial, and groove/external surface sites in the bundle. The frequencies and full width half maximums (FWHMs) for each adsorption site were determined from tentative assignments made in previous experiments and remained fixed during the simulation at 2330 and 10 cm^{-1}, respectively, for endohedral sites; 2339 and 14 cm^{-1} respectively for interstitial sites; and 2340 and 20 cm^{-1}, respectively, for groove sites.[48, 49] As discussed below, the CO_2 populations for interstitial and groove/external surface sites are displaced by Xe over different pressure ranges, so including a Lorenztian near 2340 cm^{-1} for both these sites can allow us to differentiate between them by examining the intensity profile near 2340 cm^{-1} with pressure. The integrated intensity of the Lorenztian for each site in the bundle is set from their CO_2 populations at each pressure, which are extracted directly from the GCMC simulations.

Experiments indicate that the sample degassed at 373 K retains most of its functionality and as a result, only has a small fraction of its endohedral and interstitial sites open to gas phase molecules. To account for this in the spectral simulations we multiply the GCMC determined CO_2 populations for the endohedral and interstitial sites of a fully open heterogeneous bundle by 0.05 to simulate how the spectra of a partially opened bundle might behave. The value of 0.05 gave a better "fit to eye" when compared to experimental spectra than values of 0.10, 0.15, or 0.20. We do not expect quantitative agreement between the spectral simulations and experiments (see discussion below) so these scaling factors are only used to easily simulate how selectively blocking an arbitrary fraction of endohedral/interstitial sites might change the spectral simulations when compared to simulations done on a fully open bundle without any such scaling. These scaling factors should not be interpreted, in any way, as being a quantitative representation of how many endohedral sites are opened/closed in the experimental system. The precise number of opened or closed sites cannot be obtained by the measurements presented here.

The experiments on the samples that were heated to 700 K indicate that many of the functionalities have been removed and as a result, most of the adsorption sites in the bundle are accessible. Spectra for these samples are simulated by directly using the GCMC populations for a completely open, heterogenuous bundle without any scaling.

3.3 RESULTS AND DISCUSSION

3.3.1 Physisorption of CO_2

The physisorption of gas phase CO_2 on the SWNTs after vacuum degassing at 373 K is shown in Fig. 13 . A single peak is seen at 2340 cm^{-1} from the ν_3 mode of physisorbed CO_2 that gains intensity with pressure until beginning to saturate at about 5×10^{-7} Torr. The peak at 2340 cm^{-1} on the acid oxidized SWNTs has previously been assigned to CO_2 physisorbed in groove sites on the periphery of the bundle. The SWNTs used in Fig. 13 have functionalities at defect sites from the acid purification step that can inhibit access to the endohedral and interstitial sites of the bundle.[24]. Degassing at 373 K is not sufficient to

33

cause the complete decomposition of these functionalities and consequently the IR spectra of Fig. 13. mostly show evidence for groove/external surface site adsorption.[49, 27] Later, we will show that there is some evidence from the Xe displacement studies that a small amount of endohedral adsorption does occur.
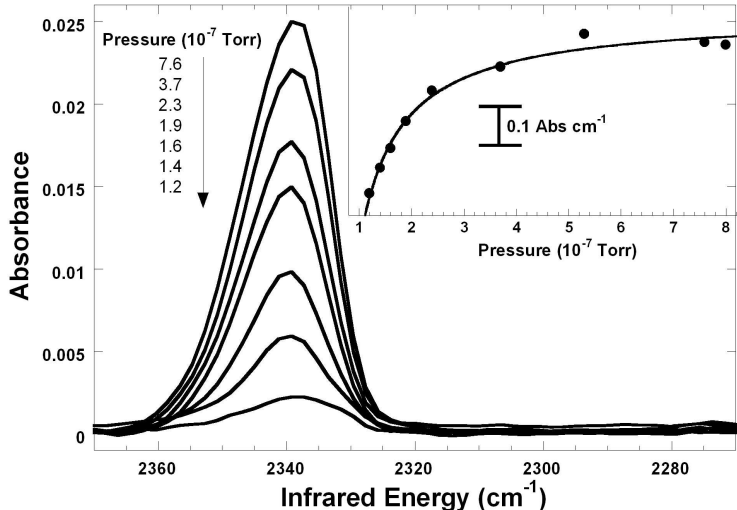
Figure 13: Infrared spectra of CO_2 physisorbed on the SWNTs at 77 K after degassing at 373 K for 2 hours. A single peak is seen near 2340 cm^{-1} from the ν_3 mode of CO_2, which gains intensity with pressure. The inset shows the integrated intensity of the IR spectra from the main figure. The solid line in the inset is only meant as a guide to the eye. The inset shows that the integrated intensity of the IR peak starts to saturate at around 4×10^{-7} Torr indicating a filling of sites associated with the 2340 cm^{-1} peak.

Vacuum heating of this sample to 700 K causes a partial decomposition of the functional groups that block access to the endohedral and interstitial sites of the bundle. The IR spectra associated with functionality decomposition on the sample used in this paper have been reported.[49] Some of the CO_2 generated during decomposition becomes permanently entrapped in the SWNT bundle and has been studied previously.[49, 50]

In order to illustrate how vacuum heating removes functionalities and opens access to new adsorption sites, we examine the physisorption of CO_2 on the SWNTs after heating to 700 K (Fig. 46). Some intensity is seen at 2330 and 2340 cm^{-1} due to the entrapped CO_2 present before introducing gas phase CO_2 to the cell. Physisorption of gas phase CO_2 first

causes the shoulder at 2340 cm^{-1} to gain intensity, with the peak at 2330 cm^{-1} following. The peak at 2330 cm^{-1} has been attributed to CO_2 in endohedral sites. The peak near 2340 cm^{-1} is more ambiguous and is seen for both interstitial and groove sites.[48, 49, 50] The similar ν_3 frequency seen for CO_2 in groove and interstitial sites suggests they have comparable adsorption environments. We have previously argued that the V-shaped pores created by adjacent nanotubes in large interstitial and groove sites are responsible for this environment. The reason for the similar morphology in the IR spectra for the trapped and physisorbed CO_2 has also been discussed.[49, 50]
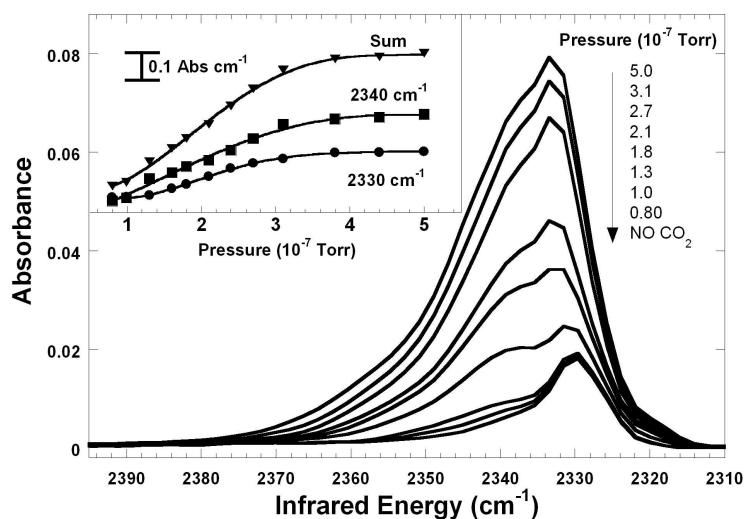
Figure 14: Infrared spectra of CO_2 physisorbed on the SWNTs at 77 K after vacuum heating to 700 K. Peaks at 2330 and 2340 cm^{-1} are seen before any gas phase CO_2 is introduced to the cell. These peaks are due to the physical entrapment of CO_2 in the bundle during the vacuum heating step. The inset shows the integrated intensity of the 2330 cm^{-1} (solid circles), 2340 cm^{-1} (open squares), and their sum (solid triangles) as determined by deconvoluting the spectra from the main figure with a two Lorenztian fit.

3.3.2 Xe Displacement of CO_2

Xe is a useful species for displacing molecules from SWNTs and this motivates our use of this technique to further understand CO_2 interactions with these materials.[46, 47, 48] Fig. 47 shows results for the displacement of CO_2 by Xe on three different nanotube bundles.

The similarity of the displacement of CO_2 from the endohedral and groove/external surface sites in these 3 panels indicates that the general displacement behavior for these sites is independent of the type of bundle chosen for the simulation and therefore not model dependent. One notable difference in Fig. 15 is the complete lack of interstitial site access in the homogeneous (10, 10) bundle (bottom panel) because these sites are too small to accommodate CO_2. In the more realistic heterogenous bundles (top 2 panels), some interstitial sites are accessible, but their populations make a small contribution to the total amount of adsorbed/displaced CO_2 (see discussion below). The lack of interstitial access in the homogeneous (10, 10) bundle is not necessarily what we expect to see experimentally, since this homogeneous bundle is not a realisitic representation of the distribution of tubes known to make up actual nanotube samples. The results for the (10, 10) bundle are included in Fig. 15 mainly to illustrate that groove/external surface and endohedral site behavior is not sensitive to whether a heterogeneous or homogeneous bundle is used for the simulations.

For further discussion, we refer specifically to the results displayed in the top panel of Fig. 15 for a heterogeneous bundle (bundle 1 of Table 3). The endohedral and interstitial sites of this bundle show a rapid loss of CO_2 in the presence of Xe with each site losing about $\frac{1}{2}$ of its initial CO_2 population by 1.7×10^{-6} Torr. The remaining fraction in these sites decreases by less than 10 % between 1.7×10^{-6} and 8.0×10^{-4} Torr. In comparision, the groove/external surface sites loose less than 1/5 of their original CO_2 population by 1.7×10^{-6} Torr with the remaining fraction decreasing by slightly more than a factor of 10 by 8.0×10^{-4} Torr.

For each adsorption site there is some fraction of CO_2 molecules that are not easily displaced by Xe at the highest pressures studied. For the endohedral and interstitial sites this remaining fraction is slightly less than $\frac{1}{2}$ of the starting CO_2 population with the groove/external surface sites retaining only $\sim 1/15$ of their initial population. The reason
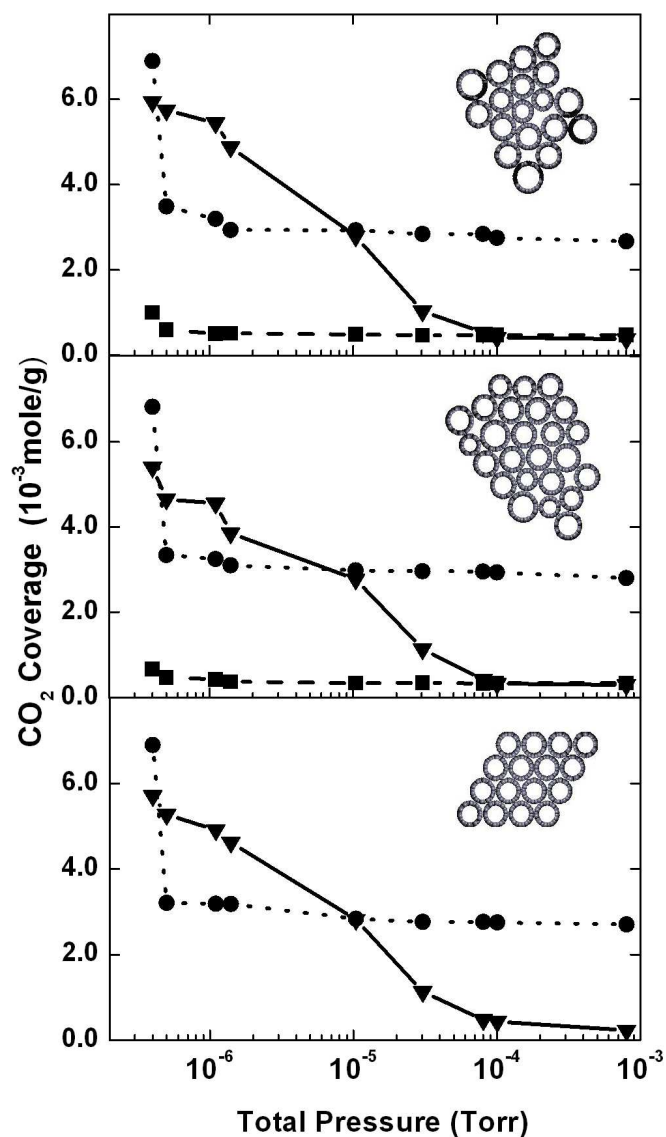
Figure 15: GCMC simulation results for the coverage of CO_2 molecules in the endohedral (dotted lines and circles), interstitial (dashed lines and squares), and groove/external surface sites (solid lines and triangles) as a function of increasing Xe partial pressure. The CO_2 pressure is 7.0×10^{-7} Torr: (top) on heterogeneous bundle 1; (middle) on heterogeneous bundle 2; (bottom) on homogeneous bundle 3. The tubes making up these bundles are described in Table 10 and their cross-sections are illustrated in the insets.

for this remaining fraction of CO_2 can be explained by considering the average energy of the physisorbed CO_2 in each of the sites on the bundle (Table 4). The endohedral and interstitial sites have the highest total average energies of 318.8 and 339.3 meV, respectively. In comparison, the groove and external surface sites have lower average energies of 258.5 and 252.2 meV, respectively. The total energy includes both CO_2-CO_2 and CO_2-SWNT interaction energies. The CO_2-CO_2 interaction is a sum of the van der Waals (Lennard-Jones) and the quadrupole-quadrupole (columbic) terms. Table 4 shows that the endohedral and interstitial sites are more strongly bound than groove and external surface sites and Xe will have more difficulty in displacing the more strongly bound species. The energies in Table 4 are average energies indicating that the fraction of CO_2that is displaced from the endohedral and interstial sites is likely from the lower end of the energy distribution associated with these sites. One interesting result in Table 4 is no single component of the average energy dominates the total energy trends seen in the different sites. The sum of all the components seems to be important when evaluating the relative stability of the different sites at the pressure and temperature used for the simulations. The importance of this observation is that one cannot predict displacement orders by the zero coverage solid-fluid energies only.

Table 4: Average energies from canonical simulations for CO_2 at 7.0×10^{-7} Torr and 77 K as determined for bundle 2 of Table 3

Site	Total Avg. Energy (meV)	Solid-Fluid Energy (meV)	Fluid-Fluid L-J Energy (meV)	Fluid-Fluid Coulombic Energy (meV)
Endohedral	318.8	218.6	65.2	35.0
Interstitial	339.3	277.0	42.3	20.0
Groove	258.5	235.1	8.7	14.7
Ext. Surface	252.2	153.0	57.0	42.2

A representative IR experiment for the displacement of CO_2 by Xe at 77 K is shown for the SWNTs after heating to 700 K (Fig. 16). An initial decrease of intensity at 2330 cm^{-1} with subsequent loss of the 2340 cm^{-1} shoulder is seen. Results for bundles that have only been degassed at 373 K prior to use are similar, but with the contribution at 2330 cm^{-1} being far less pronounced.
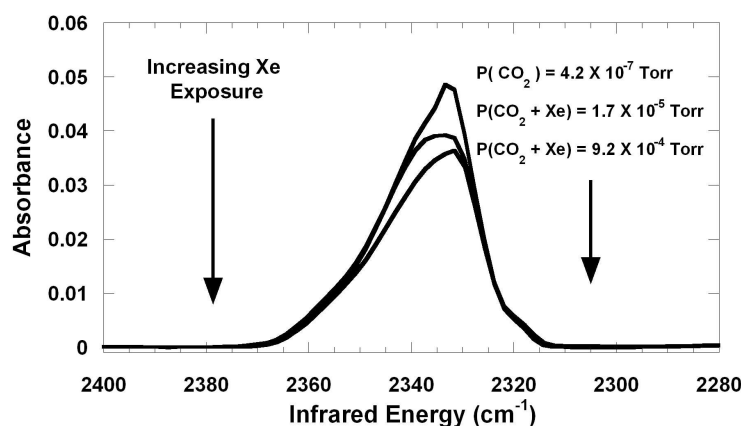
Figure 16: Representative IR experiments of Xe displacement at 77 K on a SWNT sample after vacuum heating to 700 K. The sample cell is initially charged with 4.2×10^{-7} Torr before introducing Xe. Xe exposure causes an initial loss of intensity is at 2330 cm^{-1} with loss of intensity at 2340 cm^{-1} at higher pressures. For clarity only 3 pressures are shown from the experiment.

The intensity changes associated with these CO_2 displacement experiments are best illustrated by subtracting the initial spectrum for the physisorbed CO_2 (No Xe present) from subsequent spectra as Xe is introduced into the cell (difference spectrum). Fig. 17 (a) shows difference spectra for the SWNT sample after degassing at 373 K. These difference spectra show that the introduction of Xe creates an initial intensity loss near 2330 cm^{-1} with a small shoulder at 2340 cm^{-1}. At higher pressures, a broad feature at 2340 cm^{-1} becomes evident. The initial loss near 2230 cm^{-1} indicates that some of the endohedral sites are open for CO_2 adsorption, although this is not obvious from the spectra of Fig. 13.

To correlate the IR experiments of Fig. 17 (a) with the molecular simulations we have used the data from the top panel of Fig. 15 (bundle 1) to carry out spectral simulations (see
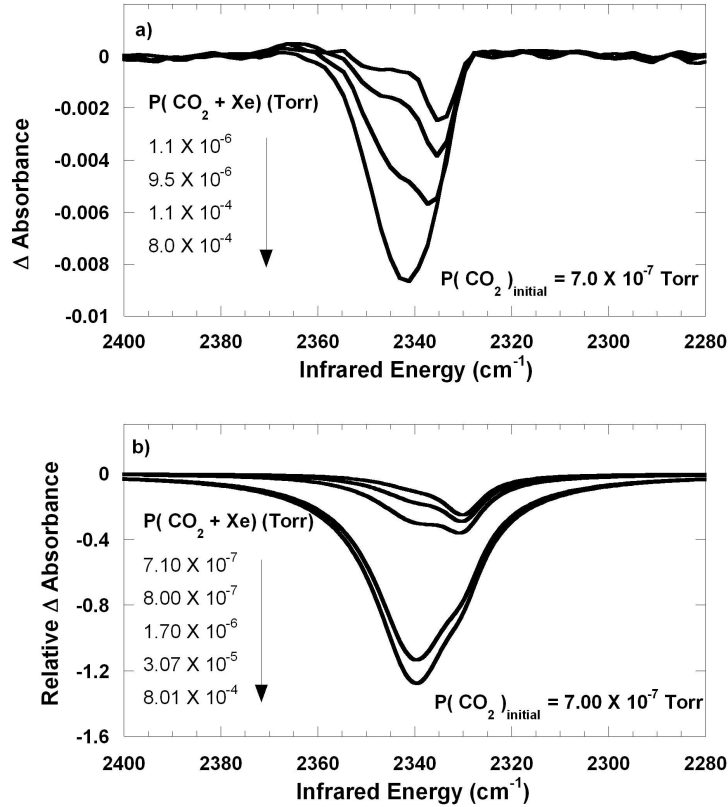
Figure 17: (a) Experimental difference IR spectra for the displacement of CO_2 by Xe from the SWNT sample with an initial CO_2 pressure of 7.0×10^{-7} Torr. The sample has been degassed at 373 K and has most of its endohedral and interstitial sites blocked. (b) Simulated IR difference spectra derived from the GCMC results on a fully open heterogeneous bundle (bundle 1 of Table 3) by scaling the endohedral and interstitial populations by 0.05 to mimic a bundle with only a small fraction of these sites available for adsorption and displacement. The initial CO_2 pressure in the simulation is 7.0×10^{-7} Torr.

Methods section). The results for a bundle with only 5 % of the endohedral and interstitial sites open for adsorption are shown in Fig. 17 (b). The spectral simulations in Fig. 17 (b) show the same qualitative behavior as the experiments in Fig. 17 (a). In the spectral simulations, the intensity loss at 2330 cm^{-1} occurs from the initial displacement of CO_2 in endohedral sites. Most of the initial intensity loss at 2340 cm^{-1}occurs from the partial displacement of groove/external surface site CO_2 occurring up to 1.70×10^{-6} Torr with the peak at 2339 cm^{-1}from interstitial CO_2 making a minor contribution overall.

The qualitative behavior of the experimental and simulated spectra agrees rather well. The intensity loss for each peak occurs in the same relative order and over the same general pressure ranges. The fact that the intensity changes of the experimental spectra are well represented in the simulations of Fig. 17 (b) by assuming that only 5 % of the endohedral sites are open for CO_2 adsorption and displacement indicates that these sites are indeed mostly blocked by functionalization with the small open fraction causing the changes seen at 2330 cm^{-1} at low pressures. The fact that only a fraction of sites are open for endohedral adsorption could be a result of slight defunctionalization during the 373 K degassing step. Another possibility is that a small number of nanotubes have very large sidewall defects that allow for endohedral adsorption even though the defect peripheries are decorated with functional groups. As discussed in the Methods Section, the 5 % scaling factor is only intended to illustrate how the selective blocking of these endohedral sites might affect the IR spectra and is not a quantitative representation of the actual number of opened endohedral sites.

The difference spectra for CO_2 displacement by Xe on the SWNTs heated to 700 K are shown in Fig. 18 (a). An initial loss of intensity is seen at $\sim$ 2330 cm^{-1} with a shoulder at 2340 cm^{-1} becoming visible at 4.3 $\times$ 10^{-4} Torr. The same sequence of intensity losses seen in Fig. 17 (a) are observed except the overall intensity contributions differ, indicating that vacuum heating to 700 K has changed the accessibility of sites in the bundle. The spectral simulations for a fully open heterogeneous bundle are shown in Fig. 18 (b). The simulations show an initial loss of intensity at 2330 cm^{-1} from displaced endohedral CO_2 followed by a loss at 2340 cm^{-1} from the displacement of groove/external surface site CO_2 starting at 1.07 $\times$ 10^{-5} Torr. Any loss of intensity at 2339 cm^{-1} occurring below 10^{-6} Torr in Fig. 18 (b) from the displacement of interstitial CO_2 is obscured by the large changes seen for endohedral CO_2 at 2330 cm^{-1}. This occurs mainly because the interstitial species has an initial CO_2 population in the simulations that is $\sim$ 1/7 of the endohedral species. Overall, the spectral simulations reproduce the qualitative behavior of the displacement experiments rather well, indicating that the intensity losses seen experimentally are likely the result of CO_2 displacement from the sites indicated in the spectral simulations. Since all the bundles in Fig. 15 give nearly identical population profiles with pressure for endohedral and groove/external surface sites.

As a control experiment, Xe displacement studies at 77 K were done without exposing the sample to CO_2 and after heating the sample to 700 K to test that the peaks at 2330 and 2340 cm^{-1} attributed to permanently entrapped CO_2 are not displaceable. No intensity changes for these peaks are seen up to Xe pressures of 9.0×10^{-4} Torr. Since the peaks at 2330 and 2340 cm^{-1} from the trapped CO_2 do not go away after exhaustive temperature cycles up to 700 K and venting to room air they also are not expected to be displaced by gas phase Xe.[49, 50]
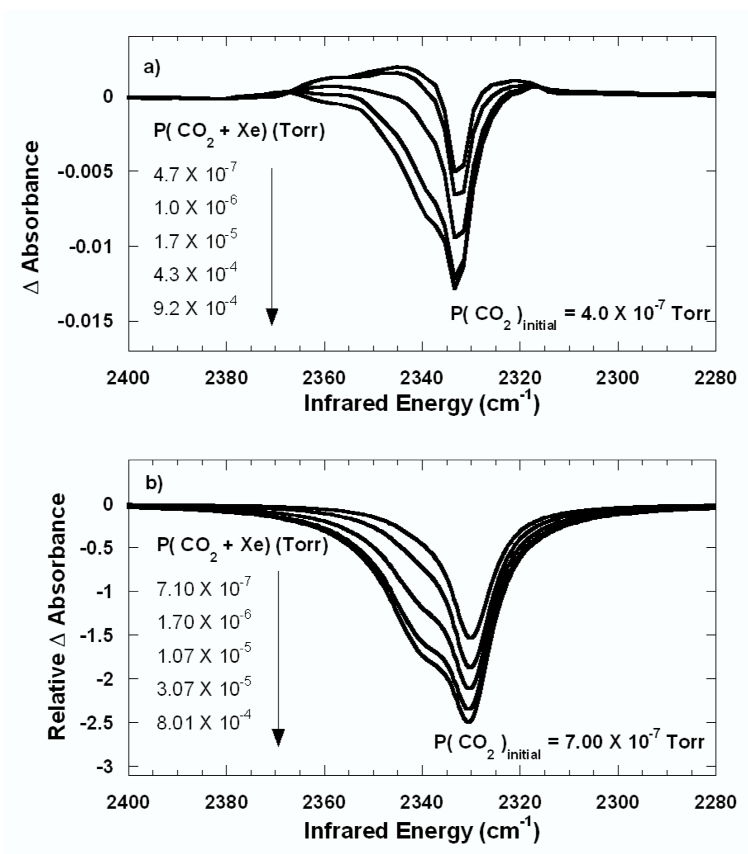
Figure 18: (a) Experimental difference IR spectra for the displacement of CO_2 by Xe after vacuum heating the sample to 700 K. The experiment was run at 77 K with an initial CO_2 pressure of 4.0×10^{-7} Torr. (b) Simulated IR difference spectra from GCMC results on a fully open heterogenous bundle (bundle 1 of Table 3), which was used to mimic the vacuum heated sample used in the experiments shown in (a). The starting CO_2 pressure in the simulation is 7.00×10^{-7} Torr.

We do not expect quantitative agreement between the simulations and experiments for the relative amount of CO_2 displaced by Xe without a precise knowledge of the bundle size distribution in the experiments. This stems from the simple observation that the ratio of endohedral and interstitial sites to groove/external surface sites is not constant with bundle size. We can illustrate this effect if we approximate the bundle as a simple cylinder. The sum of endohedral and interstitial sites should be proportional to the cylinder volume and the number of groove/external surface sites to the surface area along the length of the cylinder. This means that bigger bundles will have a larger ratio of endohedral and interstitial sites to groove/external surface sites with this ratio scaling approximately as the radius of the cylinder. This effect is likely why we see IR peaks displaced in the same relative order in the simulations and experiments but with slightly different intensity contributions at each pressure.

The spectral and GCMC simulations suggest that most of the experimental intensity changes seen during Xe displacement of CO_2 occur because of population changes in endohedral and groove/external surface sites. The large number of these sites with respect to interstitial sites in the simulation coupled with the qualitative agreement between simulations and experiments could lead to the conclusion that the interstitial sites play an insignificant role in this system. We urge caution with this interpretation. We do see a peak at 2339 cm^{-1} (Fig. 14) for trapped CO_2, which we have attributed in the past to an interstitial species.[49] The IR intensity ratio of trapped endohedral (2330 cm^{-1}) to trapped interstitial (2339 cm^{-1}) CO_2 in Fig. 14 is ~ 1.8, which is obtained by fitting this spectrum to a 2 Lorenztian lineshape. This suggests a similar trapped CO_2 population ratio assuming the IR cross section for the molecule in each site is roughly the same. We cannot say conclusively that this ratio mirrors the ultimate CO_2 capacity for these sites but it does suggest that the interstitial sites could have a significant adsorption volume in the experimental system if it were completely accessible by a gas phase species. The remaining functionalities on the sample may play a role in inhibiting access.

The role that interstitial sites play in gas interactions with SWNTs will likely be very dependent on the sample's tube size distribution and processing history. A more homogeneous distribution of tubes will likely crystallize into bundles with smaller and more regular

interstitial spaces that do not admit CO_2. Thermal annealing may also affect how the tubes pack to form bundles and interstitial sites if this step causes a large decomposition of functionalities introduced in interstitial sites between the tubes during purification. Evidence in the literature has been found both for and against interstitial adsorption with no clear cut trend with molecular size or properties.[48, 49, 50, 52] It is possible that some of the variations seen regarding interstitial accessibility are largely due to differences in the samples used for these experiments.

3.4 SUMMARY

The displacement of CO_2 by Xe on SWNTs has been investigated with IR spectroscopy and GCMC simulations. The experiments and simulations both show a sequential displacement of CO_2 with species associated with endohedral sites preceeding those in groove/external surface sites. Slightly less than ½ of the initial physisorbed CO_2 in interstitial and endohedral sites is not easily displaced by Xe whereas only 1/15 of the CO_2 population is retained in groove/external surface sites at the same pressure and temperature. Spectral simulations constructed from the GCMC results qualitatively reproduce the IR experiments for the displacement of CO_2 by Xe. The agreement between the simulations and experiments suggests that the sites associated with each IR peak and their intensity changes with Xe exposure are indeed the result of CO_2 being displaced from the adsorption sites indicated by the GCMC simulations.

4.0   TRAPPED CO$_2$ IN SINGLE WALLED NANOTUBES

The contents of this chapter were taken from Matranga, C., Chen, L., Smith, M., Bittner, E., Bockrath, B. and Johnson, J.K., *J. Phys. Chem* **107**,12930,(2003). The experimental work was performed by Chris Matranga. The simulation work was performed by myself.

4.1   INTRODUCTION

During a study of the adsorption of gases on carbon nanotube samples, we have discovered that physically entrapped carbon dioxide is produced by a mild thermolysis of partially oxidized samples. Physical entrapment of gas molecules within bundles of single walled carbon nanotubes (SWNTs) offers new opportunities to study molecules confined in a quasi one dimensional system. The study of confined molecules is a particularly active area of research and carbon nanotubes serve as an experimental realization of a one dimensional system. It is the unique structure of these SWNT bundles which is believed to create many novel adsorption and transport properties.[56, 10, 20, 17, 57, 58, 59, 19, 26] Infrared spectroscopy is particularly well suited to study adsorption and confinement in carbon nanotube bundles. In addition to directly monitoring chemical functionalities on the material,[26, 23, 25, 24] infrared spectroscopy has successfully probed adsorbate molecules for carbon nanotubes,[46, 47] C$_{60}$, and other types of carbon materials.[25] In the case of SWNT bundles, infrared studies have shown that oxygen related functionalities block access to the interior of the nanotube and vacuum heating results in a decomposition of these functionalities, which opens access to the interior of the nanotubes.[46, 47] Certain oxidative treatments have also been successful in opening access ports to interior sites in nanotubes.[46, 47] Infrared studies of these opened

nanotubes detected gas molecules adsorbed within the interior of the nanotubes.[46, 47] At low pressures, adsorption of light gases in opened nanotubes only occurs at cryogenic temperatures and the open access ports mean that desorption occurs upon heating in vacuum. Thus, these systems can only be studied over a fairly limited temperature range. In this work, we present infrared spectroscopic studies of CO_2 that becomes permanently trapped in carbon nanotube bundles during the partial decomposition of oxygen related functionalities on these bundles. We have observed trapped CO_2 in the same sample for periods of up to two months and over the temperature range (in vacuum) of 5-700 K. Furthermore, after venting the nanotube samples to room air the trapped CO_2 remains within the nanotube bundles. Venting creates few changes in the infrared spectra of the nanotubes. We use computer simulations to understand the behavior of the trapped CO_2 species and to understand how gas-phase CO_2 adsorbs in opened and closed nanotube bundles.

4.2 EXPERIMENTAL METHODS

Infrared studies were performed in a stainless steel vacuum chamber equipped with a 70 L/s turbomolecular pump, roughing pump, precision leak valve, and differentially pumped optical windows (KBr). Pressure was measured with an ionization gouge. The system base pressure was in the low 10^{-8} torr range after a 24 hour pump down. The sample was manipulated inside the chamber with an XYZ translation stage and a rotation stage. Sample cooling and heating (5-700 K) was done with a liquid He/N_2 cryostat (ST-400 Model, Janis Research) equipped with a copper sample holder accommodating a blank and one sample. The SWNT sample was purchased from Tubes@Rice as a "Purified Grade" suspended in toluene. This sample was produced by the laser ablation technique followed by a HNO3/H_2SO_4 oxidative/purification treatment to remove amorphous and unwanted carbons. The sample was dispersed directly on a 1 mm thick $\times$ 12.70 mm diameter plane parallel CaF2 window (Janos Technology) and the solvent evaporated in a 420 K oven for 5 minutes before being placed on the sample holder and transferred to vacuum. The blank was a separate plane parallel CaF_2 window placed on the same sample holder. Infrared measurements were done

with a Nicolet Nexus 670 ESP fourier transform infrared spectrometer equipped with a liquid N_2 cooled narrow band MCT detector. All measurements were taken in the transmission geometry. Spectra are averaged over 1000 scans at 4 cm-1 resolution unless otherwise noted. Infrared scans were done by heating/cooling the sample to the desired temperature and allowing for complete thermal equilibrium (20-30 mins). A reference spectrum was then taken of the blank CaF_2 window followed by a spectrum of the nanotubes dispersed on the other CaF_2 window. This process was repeated at each temperature. Under these conditions the samples were thermally stable and spectra taken at a given temperature did not change even over the course of hours. Two-Dimensional Infrared Correlation Spectroscopy (2D IR) was used to analyze the temperature dependence of the infrared spectra. In 2D IR, infrared spectra are taken as a function of an external perturbation (e.g. temperature, pressure, time). The technique allows one to easily visualize coupled intensity variations between highly convoluted spectral peaks which occur due to this perturbation. The correlation spectrum can be expressed as [60, 61, 62]

$$X(\nu_1, \nu_2) = \langle \tilde{y}(\nu_1, T) \cdot \tilde{y}(\nu_2, T') \rangle \quad (4.1)$$

$X(\nu_1, \nu_2)$ is a complex number, $X(\nu_1, \nu_2) = (\nu_1, \nu_2) + i\Psi(\nu_1, \nu_2)$, comprising two orthogonal components known as the synchronous, (ν_1, ν_2), and asynchronous, $\Psi(\nu_1, \nu_2)$, 2D correlation intensities. The synchronous 2D correlation intensity represents simultaneous intensity variations measured at ν_1 and ν_2 which occur because of the external perturbation. The asynchronous 2D correlation intensity represents sequential intensity changes at ν_1 and ν_2. The 2D IR method used here is described for the discrete case by Noda.[61, 62] A set of dynamic spectra, $y_j(\nu) = y(\nu, T_j)$, are generated by subtracting from each individual spectrum a reference that corresponds to the averaged spectrum over all the temperatures. The dynamic spectra can be conveniently represented as a column vector [60, 61, 62]:

$$(v) = \begin{bmatrix} \tilde{y}(\nu, T_1) \\ \tilde{y}(\nu, T_2) \\ \ldots \\ \tilde{y}(\nu, T_n) \end{bmatrix} \quad (4.2)$$

The synchronous spectrum is then given by the inner product of two dynamic spectrum vectors [61]:

$$\Phi(\nu_1, \nu_2) = \frac{1}{n-1}\tilde{\mathbf{y}}(v_1)^{\mathbf{T}\tilde{\mathbf{y}}(v_2)} \quad (4.3)$$

The asynchronous spectrum is given by ref.[61] :

$$\Psi(\nu_1, \nu_2) = \frac{1}{n-1}\tilde{\mathbf{y}}(v_1)^{\mathbf{T}\mathbf{N}\tilde{\mathbf{y}}(v_2)} \quad (4.4)$$

where $\mathbf{N}$ is the Hilbert transformation matrix [61]:

$$\mathbf{N} = \begin{bmatrix} 0 & 1 & \frac{1}{2} & \frac{1}{3} & \ldots \\ -1 & 0 & 1 & \frac{1}{2} & \ldots \\ -\frac{1}{2} & -1 & 0 & 1 & \ldots \\ -\frac{1}{3} & -\frac{1}{2} & -1 & 0 & \ldots \\ \ldots & \ldots & \ldots & \ldots & \ldots \end{bmatrix} \quad (4.5)$$

2D correlation analysis is simplified when spectra are collected at evenly spaced increments along the external perturbation variable. For this reason, the spectra used for 2D analysis in this study were collected every 50 K from 50-550 K. At temperatures above 550 K the intensity of the band analyzed with 2D IR becomes weak and difficult to detect. Spectra

reported at other temperatures (5, 77, and 700 K) are included to show the temperature range over which we observe the reported phenomena. Raman spectra were taken with a Nicolet Almega Dispersive Raman System with a 532 nm excitation source. The 10X objective of the microscopy attachment was used to collect spectra of samples dispersed on a CaF_2 window. A 1 second acquisition time added over 30 acquisitions was used for each spectrum. Estimated resolution is 1.5-2.5 cm^{-1} over the spectral range of 100-4000 cm^{-1}.

4.3 SIMULATION METHODS

We have modeled two different scenarios in our simulations. In the first case we model CO_2 molecules that are trapped inside the interior of individual SWNTs and in the interstitial regions of SWNT bundles. In this scenario the number of molecules in the simulation is fixed (canonical, or NVT ensemble). In the second case we consider an open system where CO_2 is allowed to adsorb onto the external and internal surfaces of SWNT bundles from the bulk gas phase. The number of molecules in the adsorption simulations fluctuates (grand canonical ensemble). The scenario is meant to model the experiments involving trapped CO_2, whereas the NVT simulations mimic CO_2 dosing experiments. Canonical ensemble simulations were carried out by first performing grand canonical Monte Carlo simulations [32] to achieve a desired fixed coverage, after which the system was allowed to equilibrate and data were taken in the NVT ensemble. In GCMC simulation part, moves were attempted randomly with probability 20% for translation/rotation and 40% each for creation and deletion. The NVT simulations consist of translation/rotation moves only. Simulations were typically equilibrated for 10^7 moves, followed by data taking for 5×10^6 moves. The maximum displacement step size was adjusted during equilibration to achieve approximately a 0.40 acceptance ratio for combined translation and rotation moves. The CO_2-CO_2 interaction was described by the Harris-Yung potential model [55], which employs three Lennard-Jones (LJ) sites and charges centered at each atom. The sites were held rigid (no bond vibration or bending allowed). Lorentz-Berthelot combining rules were used for the cross interactions. The interaction potential between CO_2 and the nanotubes was taken as cross interactions

between the LJ atoms of CO_2 and the C atoms of a graphene sheet, wrapped into a carbon nanotube. The graphite LJ parameters from Steele [35] were used for these calculations. The use of classical potentials to model the nanotube-fluid interactions precludes the modeling of electronic effects, such as the differences between metallic and non-metallic nanotubes. However, this type of potential has been shown to be accurate for modeling the adsorption of simple fluids [2], such as methane, adsorbed in bundles of carbon nanotubes. The solid-fluid potential used in the simulation was smoothed by integrating over the positions of all the carbon atoms in the nanotube. The resulting integrated potential is solely a function of the distance r from the center of the nanotube. The smoothed potential was fitted to separate polynomials for endohedral (internal) and exohedral (external) adsorption for each LJ atom type (i.e., different polynomial coefficients for carbon-carbon and for oxygen-carbon interactions). Three different nanotube bundles were considered in this work. Two bundles were constructed by randomly placing nanotubes of various diameters in a box and then optimizing the spacing between the nanotubes to mimic the vacuum heated sample. Each of these two bundles contained 18 nanotubes. Bundles 1 and 2 are representative of heterogeneous bundles, i.e., bundles with a heterogeneous distribution of nanotube diameters. Bundle 3 is a homogeneous bundle containing 9 (10,10) nanotubes packed into a perfect 3×3 array. This bundle is used to mimic the untreated nanotube samples because we only allow adsorption on the external surface (including grooves) of the bundle. We use a homogeneous bundle as a model for an unopened nanotubes bundle because previous work has shown that adsorption on the external surface of homogeneous and heterogeneous bundles is virtually identical.[2] Periodic boundary conditions were applied in all three directions. The x and y dimensions were large enough to eliminate the nearest neighbor interactions between periodic images in order to mimic isolated SWNT bundles.

4.4 RESULTS AND DISCUSSION

4.4.1 Decomposition of Oxygen Functionalities and CO$_2$ Entrapment

Infrared spectra of the carbon nanotube sample are shown in Figure 19a. Vibrational modes consistent with oxygen containing functionalities are apparent. At 300 K, vibrations due to carbonyl groups are detected at 1735 cm^{-1}and C-O type vibrations are seen at 1250 cm^{-1}. A very broad peak, which has previously been assigned to C=C vibration, is also seen at 1610 cm^{-1}.[24, 25] These types of oxygen derived functionalities have been seen in previous reports for carbon nanotube samples partially oxidized by a HNO$_3$/H$_2$SO$_4$ treatment [17, 19, 42]. Upon heating, a slight intensity decrease is seen in the 1735 cm^{-1} band accompanied by a frequency shifting toward 1690 cm^{-1}. Heating causes a slight intensity increase in the C-O band at 1250 cm^{-1} with shifting to 1220 cm^{-1} and the appearance of a new band occurs at 1080 cm^{-1}. The bands at 1220 cm^{-1} and 1080 cm^{-1} are close in energy to bands previously assigned to asymmetric and symmetric modes, respectively, of esters on carbon nanotubes, while the band at 1690 cm^{-1} is close in energy to carbonyls associated with quinone functionalities.[25] Heating causes the C=C mode at 1610 cm^{-1} to lose intensity on its high energy side and eventually become a very sharp feature at 1570 cm^{-1}. This sharp feature is evident in previous reports for carbon nanotubes heated to 723 K [24] and is likely related to the IR active nanotube phonon band at 1580 cm^{-1}. This phonon band becomes better defined after heating to $\sim$ 1000 K.[24]

The IR changes seen in Figure 19a are consistent with a partial decomposition of oxygen related functionalities on the nanotubes. After initial heating of the nanotube sample to 700 K the changes shown in Figure 19a become permanent and persist without change over the temperature range of 5 - 700 K. The frequency shifts seen after heating for some of the vibrations suggests that in addition to partial decomposition there are structural changes occurring to the functionalities or to the defect sites with which they are associated.

Figure 19b shows IR spectra taken in the region near the ν_3 asymmetric stretching mode of CO$_2$during heating. At 300 K, the IR spectra are featureless but at 400 K a vibrational mode becomes evident at 2334 cm^{-1} and at 500 K shoulders start to become apparent
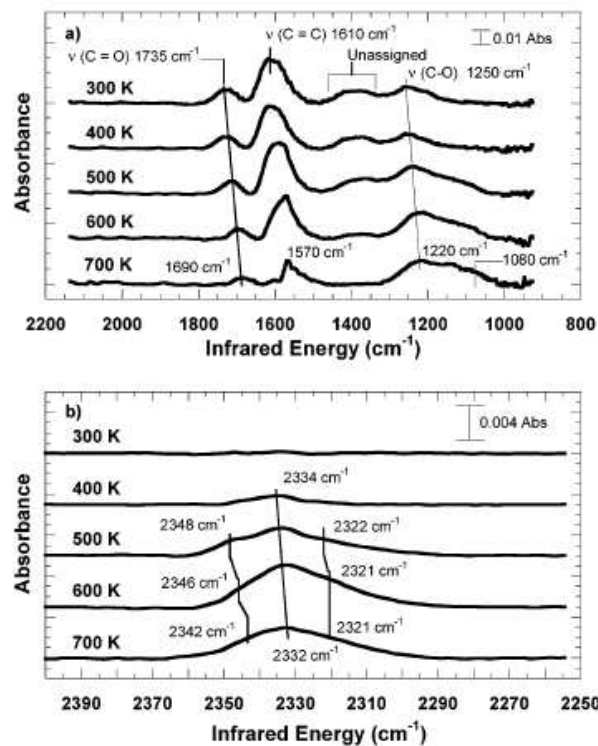
Figure 19: Infrared spectra of single-walled carbon nanotubes heated in a vacuum (a) The partial decomposition of oxygen-related functionalities in the 800-2000 cm^1 region. (b) The appearance of a new vibration near the v_3 mode of gaseous CO_2.

at 2348 cm^{-1} and 2322 cm^{-1}. At higher temperatures the peaks broaden and resolving each individual component becomes difficult. The decomposition of oxygen functionalities coupled with the appearance of a new IR band near the ν_3 frequency CO_2 in Figure 19b leads to the conclusion that the modes near 2330 cm^{-1} are due to CO_2 produced during the heating process. Previous studies have shown that CO_2 is generated during the heating of fictionalized carbon nanotube samples.[24]

The frequency shift from the gas phase seen for the ν_3 band in Figure 19b indicates a substantial interaction with the nanotube sample. By comparison, CO_2 adsorbed in powdered carbon has a band near 2332 cm^{-1}. In C_{60} films there is a band reported at 2328 cm^{-1}, or 2331 cm^{-1} depending on details of the film preparation. CO_2 trapped in octahedral voids of a C_{60} crystal has a vibration reported at 2332 cm^{-1} and 2329 cm^{-1}. CO_2 physisorbed on graphite displays a vibration at 2341 cm^{-1}. The extremely wide range of carbons creating a ν_3 band near 2330 cm^{-1} is indeed surprising.

After the initial thermal heating, the features near 2330 cm^{-1} in Figure 19b become permanent bands in the IR spectra and do not disappear with time or upon temperature cycling from 5 to 700 K. These features do broaden and change in intensity in a reversible fashion during subsequent heating cycles (see below). These results show that the thermally induced functionality changes are stable and that some of the associated CO_2 generated during heating is trapped within the carbon nanotube bundle. The CO_2 trapped in our samples persists after multiple temperature cycles and we have observed the ν_3 bands near 2330 cm^{-1} in samples for as long as 2 months in the vacuum chamber. Venting the vacuum chamber to room air and pressure (Figure 20) creates a slight intensity increase in the mode at 1610 cm^{-1} with the mode at 1690 cm^{-1} remaining unchanged in intensity and frequency. The bands near 2330 cm^{-1} also persist after venting of the chamber suggesting that CO_2 is indeed permanently trapped. Raman spectroscopy (Figure 21) of samples heated under vacuum and vented to room air display radial breathing modes characteristic of SWNTs. The Raman results prove that vacuum heating does not produce any drastic decomposition or rearrangement of the nanotube structure.

In order to test whether the CO_2 trapped within these samples comes from the oxygen functionalities on the sample or trace amounts of CO_2 residing in the vacuum chamber, we
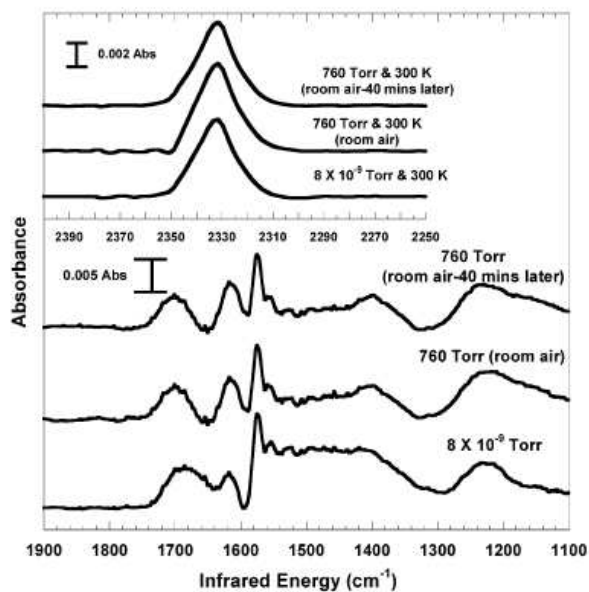
Figure 20: Infrared spectra of single-walled carbon nanotubes heated in a vacuum and subsequently vented to room air. In the 1100-1900 cm^{-1} region, no significant changes are seen with oxygen-related functionalities except for a slight growth in the band at 1610 cm^{-1}. The inset shows the IR spectra in the 2250-2400 cm^{-1} region illustrating that the vibration at 2330 cm^{-1} persists even after exposure to room air.
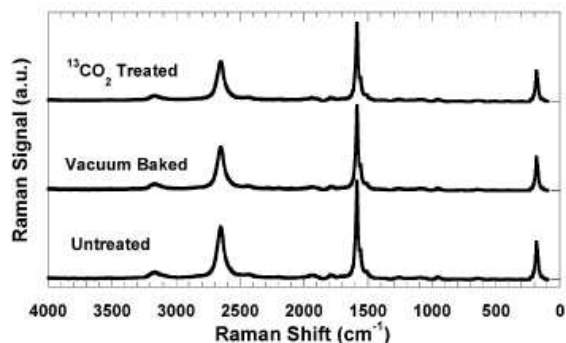
Figure 21: Raman spectra of untreated single-walled carbon nanotubes, vacuum heated nanotubes, and $^{13}CO_2$ treated nanotubes. The characteristics radial breathing modes are apparent for all samples indicating that neither vacuum heating nor $^{13}CO_2$ treatment results in any significant disruption of nanotube structure.

have vacuum heated samples to 700 K in 8×10^{-4} torr of ^{13}C enriched CO_2 for periods of about 1 hour. The functionality changes for samples heated under $^{13}CO_2$ are identical to those heated under a high vacuum (Figure 22). No evidence for trapped $^{13}CO_2$ was found near the 2283 cm^{-1} ν_3 mode of the isotopically labeled gas. IR bands were observed for unlabeled CO_2 as seen in Figure 19b indicating that the trapped CO_2 does not come from adventitious CO_2 gas in the vacuum chamber.

IR spectra for the $^{13}CO_2$ heated sample during venting are shown in Figure 23. Raman for this sample is displayed in Figure 21 . The results are identical to those shown earlier for the vacuum heated samples with the functionality changes and trapped CO_2 persisting even after exposure to atmosphere.

The changes in oxygen functionalities and generation of trapped CO_2 shown in these samples are not particular to the substrate or vacuum environment used in these experiments. Experiments run in the vacuum chamber using KBr windows as sample supports instead of CaF_2 also find trapped CO_2 in the nanotubes after heating to 700 K. Furthermore, samples heated to 673 K under ~ 250 atm of CH_4 in an autoclave cell also show the trapped CO_2 in their infrared spectra.
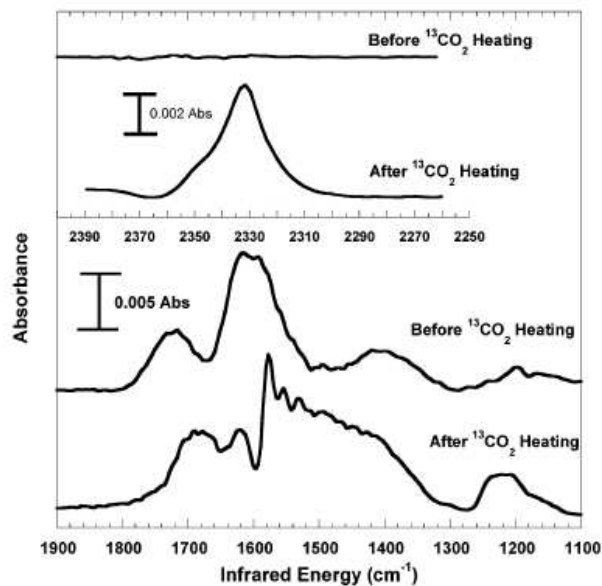
Figure 22: Infrared spectra of single-walled carbon nanotubes heated for 1h in 8×10^{-4} Torr of $^{13}CO_2$ at 700 K. Partial decomposition of oxygen-related functionalities is apparent in the IR of the 800-2200 cm^{-1} region. Few differences are apparent from the vacuum-heated sample shown in Figure 19. Inset shows the appearance of the v_3 vibration near 2330 cm^{-1} after heating in $^{13}CO_2$.
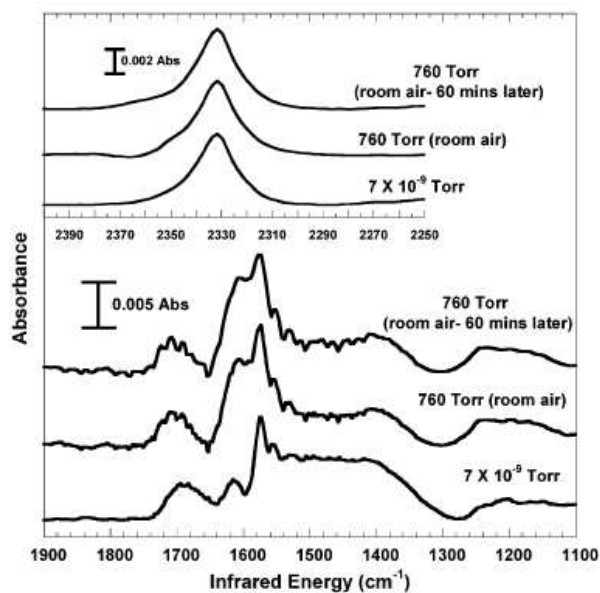
Figure 23: Infrared spectra of $^{13}CO_2$ treated single-walled carbon nanotubes during venting of the sample to room air. In the 1100-1900 cm^{-1} region, no significant changes are seen with oxygen-related functionalities except for a slight growth in the band at 1610 cm^{-1}. The noisy appearance of this spectrum is related to the incomplete background subtraction of atmospheric water vapor. Inset shows the 2250-2400 cm^{-1} region with the v_3 vibration at 2330 cm^{-1} persisting even after exposure to room air

4.4.2 Temperature Dependence of the Trapped ν_3 Band

As mentioned above, the vibrational bands near 2330 cm^{-1} in thermalized samples persist at all temperatures and display reproducible intensity and linewidth variations as a function of temperature. The temperature dependence of the 2330 cm^{-1} mode is shown in Figure 24a for a vacuum heated sample and in Figure 24b for a sample heated in 8×10^{-4} torr of $^{13}CO_2$. At low temperatures a prominent peak is seen near 2330 cm^{-1} with a high energy shoulder near 2340 cm^{-1}. Upon heating these peaks broaden and a low energy shoulder starts to develop near 2320 cm^{-1}. At 550 K the spectra evolve into what appears to be a single, broad, vibrational peak.
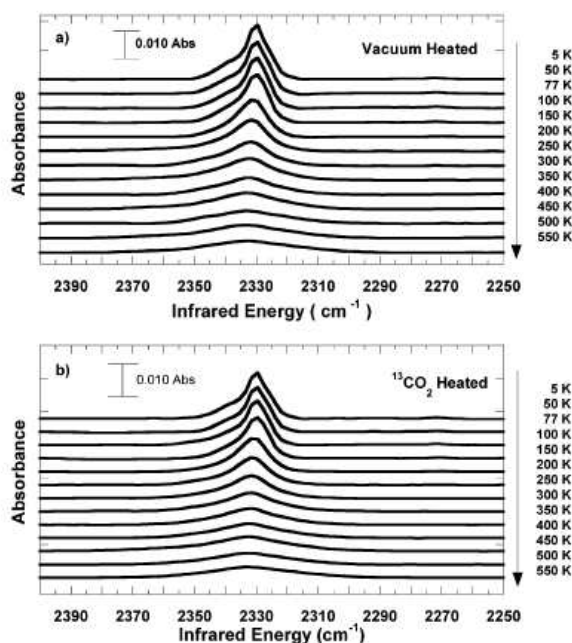
Figure 24: Temperature dependence of the v_3 mode of CO_2 trapped within single-walled carbon nanotube bundles. (a) Infrared spectra in the region of 2250-2400 cm^{-1} for a vacuum-heated sample. Spectra are intentionally offset on the y-axis for clarity. (b) Infrared in the same region as (a) but for a sample heated in $^{13}CO_2$. Again, y-axis offset is introduced for clarity

In an effort to understand the broadening and intensity changes seen in Figure 246, we have used 2D IR to analyze the data. The correlation spectra are given in Figure 25.

The intensity of synchronous 2D spectra represents simultaneous changes of intensity, which occur at two independent spectral frequencies, ν_1 and ν_2, during heating. Simply put, if vibrational peaks in a set of spectra are coupled and experience simultaneous changes upon heating, then this should be reflected in the synchronous 2D spectra. Figure 25a shows a positive autopeak at ν_1/ν_2 of 2330/2330 cm^{-1}that corresponds to the loss of intensity seen at 2330 cm^{-1} upon heating. Also, a negative cross peak is resolved at ν_1/ν_2 of 2318/2330 cm^{-1}. Negative cross peaks indicate that the intensity at one spectral variable is increasing while the intensity at the other variable is decreasing. In this particular case, the autopeak represents the decreasing intensity of the central 2330 cm^{-1} peak coupled with the increasing intensity of the low energy shoulder at 2320 cm^{-1}.

Asynchronous correlation spectra are also shown in Figure 25b. Peaks in the asynchronous spectra represent sequential changes that occur between bands in spectra. Asynchronous spectra are particularly useful in resolving overlapping bands of different origin in spectra. The asynchronous spectra show cross peaks at 2330/2340 cm^{-1} and at 2320/2330 cm^{-1}. This suggests that in addition to the clearly resolved feature at 2330 cm^{-1} in Figure 25, that the shoulders at 2340 cm^{-1} and 2320 cm^{-1} arise from distinct vibrational bands. This is also convincingly demonstrated by noting that the bands at 2320, 2330, and 2340 cm^{-1} are fairly well resolved in the spectra of Figure 19b.

The bands observed at 2340, 2330, and 2320 cm^{-1} suggest that there are three distinct environments accessible to CO_2 within the nanotube bundles. Using these three distinct vibrational features, we fitted the IR spectra with three lorenztians and extracted the integrated area, the resonance frequency, and linewidth, of each peak as a function of temperature.

The resonance frequency of each mode is shown in Figure 26a as a function of temperature. The vibrational frequencies of the bands near 2340 cm^{-1} and 2330 cm^{-1} increase with temperature from 2336 to 2342 cm^{-1} and from 2329 cm^{-1} to 2333 cm^{-1}, respectively. The frequency variation with temperature for both these modes is approximately linear. The mode near 2320 cm^{-1} shows no real frequency shifting upon heating.

Figure 26b shows that each mode broadens in an approximately linear fashion as a function of temperature. This broadening is, what makes the IR spectra at higher temperatures look like a single broadened vibrational feature rather than 3 distinct, resolved features.
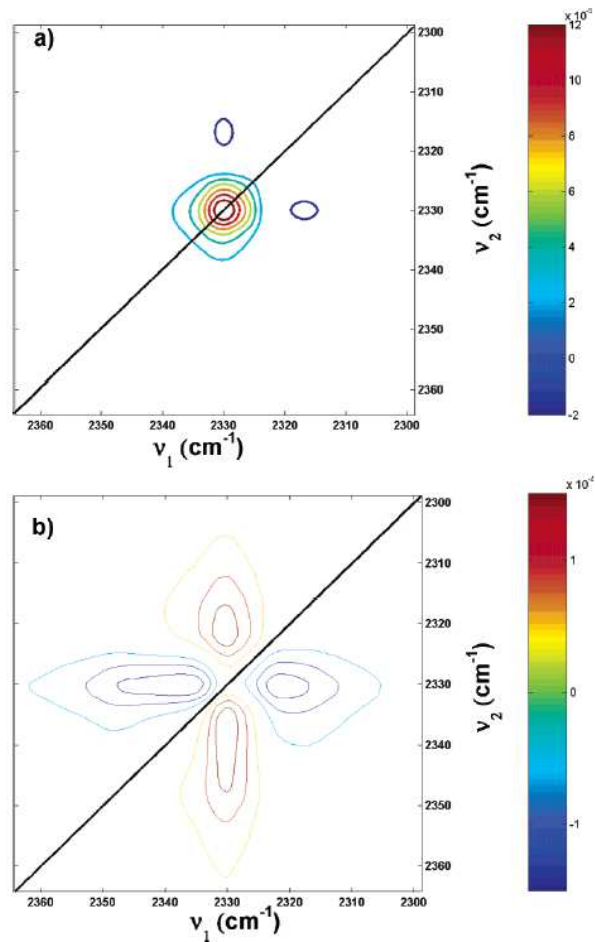
Figure 25: Two-dimensional correlation spectra displaying the temperature-induce changes in the v_3 mode of CO_2 trapped within the nanotube bundles. (a) Synchronous spectra for sample where trapped CO_2 is produced by vacuum heating to 700 K. (b) Asynchronous spectra for sample from (a). Two-dimensional correlation spectra for $^{13}CO_2$ heated samples show similar results.
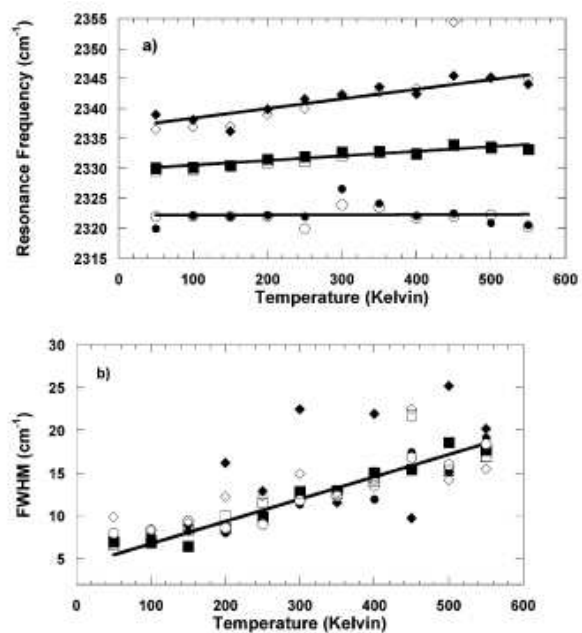
Figure 26: Temperature dependence of spectral parameters from the 3 Lorenztian line shape fit. (a) Temperature dependence of the resonance frequency for the mode near 2320 cm^{-1} (solid and open circles), 2330 cm^{-1} (solid and open squares). and 2340 cm^{-1} (solid and open diamonds). Solid symbols correspond to the vacuum-heated sample and open symbols to $^{13}CO_2$ treated sample. (b) Effect of temperature on the line width of the 3 Lorenztian features (same key as (a)).

The integrated areas for each deconvoluted vibration are shown in Figure 27a and 27b. The feature at 2330 cm^{-1} displays a strong decrease in its integrated area while the feature at 2320 cm^{-1} displays an increase. Below $\sim$ 300 K, the integrated area of the 2320 cm^{-1} mode becomes negligible. The band at 2340 cm^{-1} shows a decrease in integrated area upon heating. One striking feature of Figure 27 is the decrease of total integrated intensity from 2250-2390 cm^{-1} upon heating. This intensity loss is reversible and reproducible over successive temperature cycles (Figure 27b). No new CO_2 is introduced between temperature cycles so the intensity variations occur from a physical process, not from the loss of trapped CO_2 during heating. The factor of $\sim$ 2 change seen in the integrated intensity for each of the vibrations during heating indicates a $\sim$ $\sqrt{2}$ change in the dynamic dipole moment, $(\partial\mu/\partial Q_i)$, of trapped CO_2. This change is likely related to the temperature dependent interactions of the trapped CO_2 molecule with the nanotube bundle, which we examine through computer simulations below.

4.4.3   Simulations Results

We model CO_2 trapped in the interior of SWNTs and in the interstitial channels of nanotube bundles in order to examine possible causes for the temperature dependence of the IR peaks. For the vacuum heated samples, the CO_2 molecules are trapped in the interior and interstitial sites; thus we use a heterogeneous bundle in the calculations since GCMC simulations indicate that CO_2 does not adsorb in the interstitial channels of close-packed homogeneous nanotubes. We have computed the potential energy distribution for CO_2 trapped inside heterogeneous nanotube bundles at endohedral and interstitial sites at a constant coverage as a function of temperature. Figure 28a and Figure 28b present the results for endohedral and interstitial sites, respectively. At low temperatures, CO_2 molecules are practically trapped in the sites with the highest binding energies, as seen by the sharply peaked potential energy distribution. As the temperature increases, the CO_2 molecules move more freely in phase space and have a much larger probability of occupying sites with lower binding energy, which results in broader peaks with increasing temperature as shown in Figure 28. If we assume that the IR shift is roughly proportional to the binding energy, then the broadening and
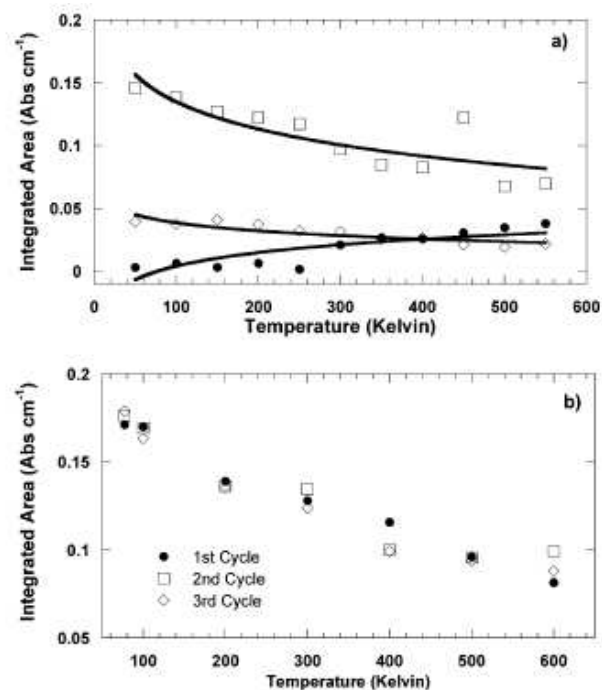
Figure 27: Temperature dependence of integrated intensity of the trapped v_3 mode. (a) Integrated area of the Lorenztian near 2320 cm^{-1} (solid circles), 2330 cm^{-1} (open squares), and 2340 cm^{-1} (open diamonds). For clarity only, results from the ^{13}CO$_2$ heated sample are shown, but vacuum-heated samples show the same trends. Solid lines are only meant as a guide to the eye. (b) Total integrated intensity change for the region 2250-2390 cm^{-1} during multiple temperature cycles.

decrease of the 2330 cm^{-1} and 2340 cm^{-1} peaks can be understood as the result of CO_2 molecules escaping from a tightly bound solid-like adsorbed phase to a freer, gas-like phase that is much less strongly bound to the surface. This change of state can be seen more clearly in Figure 29, which shows the densities profiles inside a (10,10) nanotube at the same coverage as in Figure 28a. At the lowest temperature the CO_2 molecules are mostly packed against the walls of the nanotube, shown as the first peak on the right in Figure 29. The smaller second peak on the right arises from configurations where the CO_2 molecules are closely packed together in such a way that some molecules are not parallel with the nanotubes axis, thus shifting their center of mass out slightly from the tube wall. This orientational ordering is due to quadrupole-quadrupole interactions and will be discussed in more detail later. There is also a small peak for CO_2 molecules in the center of the tube shown by the peak at r=0 for 100 K. This annular CO_2 occurs because the molecules form solid-like clusters rather than showing uniform density down the length of the tube. As the temperature increases the structure disappears; the density next to the wall decreases and the second and third peaks disappear. At very high temperatures the fluid is almost uniformly distributed across the radius of the nanotube, indicating a gas phase confined within the tube.

Note the presence of a large gap in energy distributions between 100 and 200 K in figure. This feature is indicative of a phase transition from a condensed phase of CO_2 to a gas-like phase inside the nanotube. There is no such energy gap for CO_2 in the interstitial sites because the interstitial channels are more strongly confined and more closely correspond to a true one-dimensional system (i.e., no first order phase transitions). The interior of a (10,10) nanotube is large enough to exhibit quasi-2-dimensional behavior.

Figure 30 presents the results for CO_2 adsorption isotherms on the closed perfect bundle at temperatures ranging from 77 to 100 K. No molecules were allowed to adsorb inside the nanotubes during the simulation. These simulation results should be compared with experimental data for CO_2 adsorption on untreated SWNT bundles. We assume that untreated nanotubes are either unopened or have internal and interstitial adsorption sites blocked by residual functional groups. Hence, we expect only groove site and external surface adsorption for these untreated nanotubes. Other simulations have shown that adsorption of simple
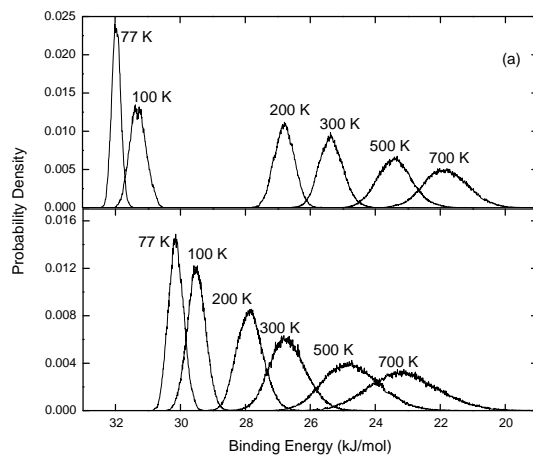
Figure 28: Potential energy distributions as a function of temperature. (a) For CO_2 trapped in the interior a (10,10) nanotube. (b) For CO_2 trapped in the interstitial regions of a heterogeneous nanotube bundle.
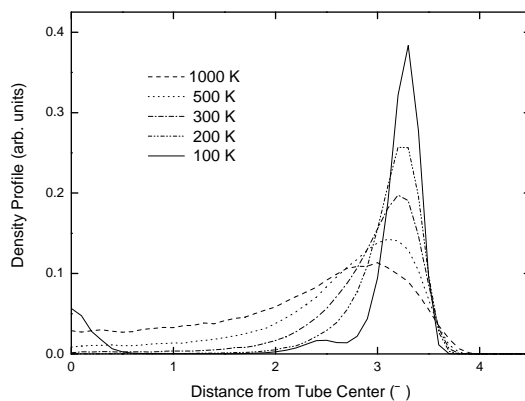
Figure 29: Density profiles for CO_2 trapped inside a (10,10) nanotube at constant coverage of 0.16 molecules per Angstrom as a function of temperature.

gases on groove sites and external surfaces of homogeneous and heterogeneous bundles are virtually identical. Therefore, we have used homogeneous bundles to examine adsorption of CO_2 in the groove sites in order to simplify the simulations.

The isotherms in Figure 30 each contain two plateaus. Each plateau corresponds to the filling of a certain type of site on the exterior of the nanotube bundle. Groove site filling corresponds to the first plateau in the isotherms shown in Figure 30. Analysis of simulation snapshots shows that quadrupole-quadrupole interactions force CO_2 molecules to form a T-shaped 1-dimension chain in the groove, as shown in Figure 31. Analysis of simulation snapshots at lower pressures show that a low density adsorbed phase forms first, where the CO_2 molecules are well separated and have their axes aligned with the groove axis in order to maximize their van der Waals interactions with the tubes making up the groove. As the pressure increases the distance between the CO_2 molecules in a single groove gets smaller and the molecules experience competing effects of repulsive quadrupole-quadrupole interactions and attractive dispersion interactions between a pair of CO_2 molecules. Roughly speaking, at close packing every other CO_2 molecule rotates up with its molecular axis perpendicular to the direction of the groove in order to make the quadrupole-quadrupole interactions attractive. This behavior is shown for a snapshot from a simulation at 90 K in Figure 31. Snapshots from isotherms at 77 and 100 K also show this behavior for loadings corresponding to groove site filling.

The second plateau appearing on each of the isotherms in Figure 30 corresponds to the formation of a monolayer film. These films begin to form at about 10^{-7}, 3×10^{-5}, and 6×10^{-4} torr at 77, 90, and 100 K, respectively. A contour density plot showing a close up of the bundle surface is shown in Figure 32. The top panel corresponds to the monolayer plateau region. However, the entire surface of the bundle is not actually covered. A bilayer film begins to form past the second plateau regions on each of the isotherms shown in Figure 30. The density contours are shown in Figure 32 in the lower panel. Note that the bilayer begins to form over the groove site first. Examination of various simulation snapshots and density contour plots (not shown) indicates that the bilayer begins to form well before the entire surface of the bundle is covered with a monolayer. In general, tubes on the corners of the bundle have sub-monolayer coverage, whereas tubes away from corners have

complete monolayer coverage. This means that experimentally observed vibrational spectra are not expected to show distinct changes with increased exposure. The spectra should gradually broaden and shift as the coverage increases. This is precisely what is observed in the experiments. We note that we do not observe a clear second-layer groove phase or three-stripe phase as observed by Cole et al. [9] We believe that this is due to our using a small finite bundle rather than an infinite row of nanotubes.
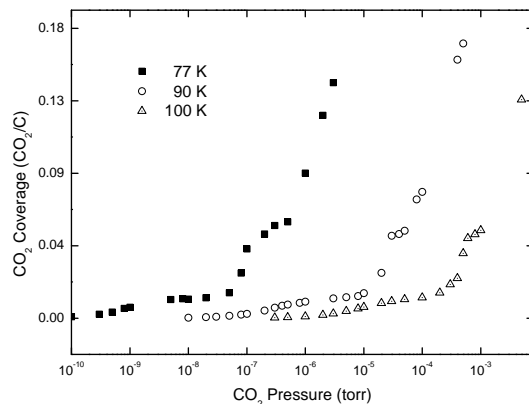
Figure 30: Adsorption isotherms at 77, 90, and 100 K for CO_2 on a closed perfect bundle of 9 (10,10) nanotubes.

We next consider adsorption of CO_2 on interstitial and internal sites of a heterogeneous nanotube bundle. Results of GCMC simulations on bundle 1 are plotted in Figure 33. Note that at low pressures (see the inset to Figure 33) the interstitial sites fill first, followed by adsorption inside the nanotubes. This qualitatively matches the experimental observations from dosing CO_2 on the heated nanotubes. The 2340 cm^{-1} mode, which we assign to interstitial adsorption, is seen to fill first, followed by growth of the 2330 cm^{-1} mode (assigned to internal adsorption). The quantitative differences may stem from the fact that in the experimental situation only a small fraction of the interstitial sites and nanotubes are opened enough to allow gas adsorption.
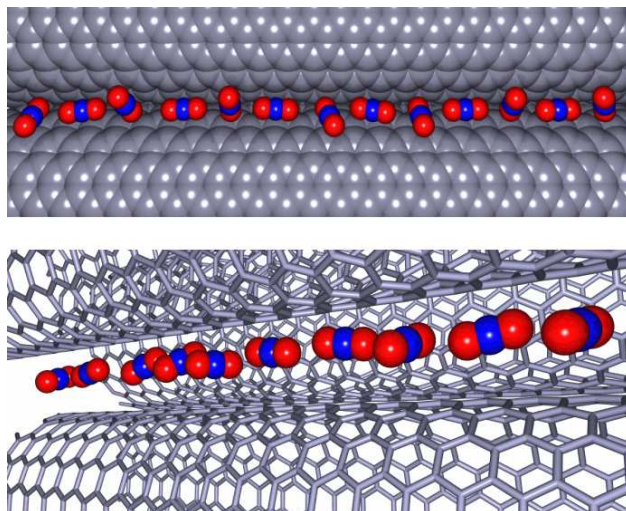
Figure 31: (top) Snapshot of CO_2 adsorption in a single groove site on a closed perfect bundle of 9 (10,10) nanotubes at 90 K and 3×10^{-6} Torr. Snapshots at other temperatures display similar structures at groove filling. Red spheres are oxygen atoms, blue spheres represent carbon in CO_2, and gray spheres represent carbon in the nanotubes. (bottom) Snapshot of CO_2 adsorption in an interstitial site of bundle 1. The carbons in the nanotubes are shown in wire frame to make the adsorbed CO_2 molecules visible. Most of the tubes in the bundle have been excluded from the figure for clarity.
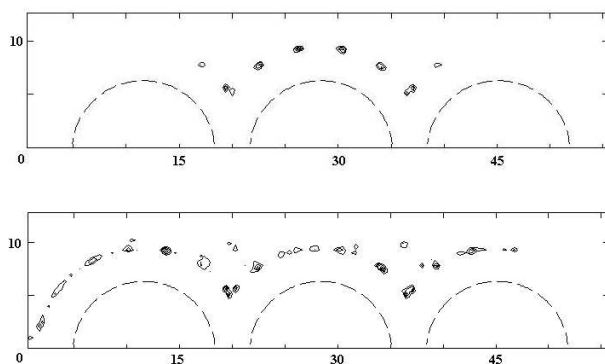
Figure 32: Density contours for CO_2 adsorbed on the external surface of a perfect bundle consisting 9 (10,10) nanotubes. Two groove sites are shown, along with the surface of the three tubes making up one side of the bundle. The central tube is located in the center of one edge of the nanotube bundle. The upper panel corresponds to a coverage of 0.055 molecule/carbon atom and the lower panel to a coverage of 0.1 molecule/carbon. Individual nanotubes are represented as deshed lines.
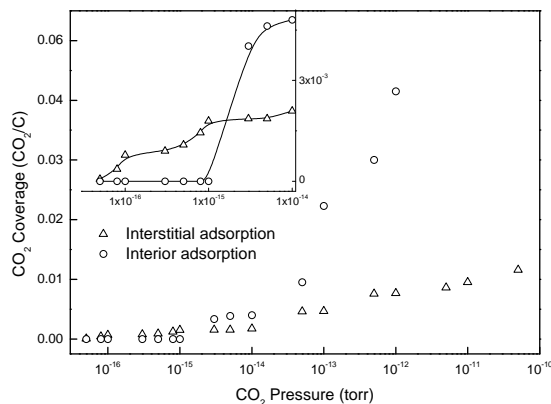
Figure 33: Adsorption isotherm at 77 K on a heterogeneous bundle. The inset shows the low pressure region. Gas initially adsorbs in the interstitial channels formed by nanotube packing defects, then into the open nanotubes.

4.4.4 Assigning Adsorption Sites for the ν_3 Bands

Assigning vibrational bands to particular adsorption sites can be a tricky task in heterogeneous samples like carbon nanotubes. Arguments for certain sites can be made based on all of the experimental and computational information available from this study. These assignments are tentative and are based on currently available data. Further experimentation and computational studies will be needed to make theses assignments definitive.

In a nanotube bundle, adsorption can occur in groove sites, interstitial sites, inside the tube, and on the curved outer surface of the nanotube. The only logical adsorption sites that can occur for the trapped CO_2 species are interstitial sites and sites inside the nanotube. Based on this, the bands seen at $\sim$2340 cm^{-1} and $\sim$2330 cm^{-1} for trapped CO_2 (Figure 24) must arise from either of these two sites. It is later argued that the mode at 2340 cm^{-1} comes from CO_2 in interstitial sites and the 2330 cm^{-1} vibration from CO_2 inside the nanotubes.

Adsorption on unheated nanotubes creates a single band at $\sim$2340 cm^{-1} which is similar to the one seen for trapped CO_2. This band must arise from a site with a similar enough local environment to produce the ν_3 frequency of $\sim$2340 cm^{-1} for both cases. The only site of similar nature on both the exterior and the interior of a bundle are the groove and larger interstitial sites, respectively. In both cases a V-shaped channel is created between adjacent nanotubes. Intuitively, a CO_2 molecule will lie lengthwise in the V-shaped channel in order to maximize its van der Waals interactions with the nanotube. Our simulations show that at high coverage the CO_2 molecules rotate with respect to one another in order to facilitate an attractive quadrupole-quadrupole interaction (see Figure 31). We therefore expect the local environment, particularly at low temperatures, to be nearly identical for both cases. The simulation snap shots of Figure 31 support this argument by showing that the adsorption geometry for both the groove and interstitial sites are similar. Based on this argument we assign the 2340 cm^{-1} band for the trapped CO_2 to CO_2 in interstitial channels. The 2340 cm^{-1} band of physisorbed CO_2 in unheated tubes is assigned to groove sites on the exterior of the bundle. Assigning the 2340 cm^{-1} mode to interstitial adsorption for trapped CO_2 forces the assignment of the 2330 cm^{-1} mode for trapped CO_2 to sites within the interior of the nanotube itself (endohedral).

Heating of the nanotube bundle creates a partial decomposition of chemical functionalities, which are known to block access to interior sites of the bundle. This is seen in adsorption experiments on unheated and heated samples, which display different adsorption sites. Adsorption of gas phase CO_2 on the heated nanotubes increases the intensity of the ν_3 bands of the trapped CO_2 species suggesting that the gas phase molecules are accessing identical sites as the trapped species. This suggests that in addition to trapping CO_2 in interstitial and endohedral sites, thermolysis also partially opens the nanotubes for CO_2 adsorption. The adsorption data of Figure reffig:trap16 show that the 2340 cm^{-1} band, which was assigned above to interstitial sites for trapped CO_2, grows before the 2330 cm^{-1} band assigned to endohedral adsorption. In addition to the earlier arguments for assignment of these bands, this sequential filling is also seen in the adsorption simulations displayed in Figure 33. This serves as another piece of evidence for these particular band assignments.

The similarity in frequency between the 2340 cm^{-1} modes from the current study and the 2340 cm^{-1} seen for CO_2 adsorption on graphite tempts one to assign this peak to CO_2 physisorbed on graphitic like carbon in the nanotube samples. We rule out CO_2 on graphitic carbon as a source for this peak in the nanotube samples since we observe contributions from the 2340 cm^{-1} band for trapped CO_2 over the entire temperature range (5 to 700 K) of this study. If graphitic carbon were the adsorbent for the trapped CO_2 species at 2340 cm^{-1}, heating in this manner would result in desorption from the graphite surface and a complete loss of intensity from the 2340 cm^{-1} mode.

The mode seen at 2320 cm^{-1} is difficult to assign. Since this mode is only seen during heating, it is possibly related to CO_2 diffusing into higher energy sites inside the tubes and interstitial pores. The simulation results of Figure 28 show this scenario by demonstrating how heating increases the ability of trapped CO_2 to sample phase space and access higher energy binding sites within both the nanotube and interstitial pores. Another possible cause for the 2320 cm^{-1} peak is that it is an artifact due to broadening of the central 2330 cm^{-1}. Currently, we are unable to make a strong argument for the origin of the 2320 cm^{-1} mode.

As mentioned earlier, many different types of carbon produce adsorbed [26, 27, 29] and trapped CO_2 species [23, 28] with vibrational frequencies similar to those observed in this study. This suggests that the frequency shifting from the gas phase seen for these species
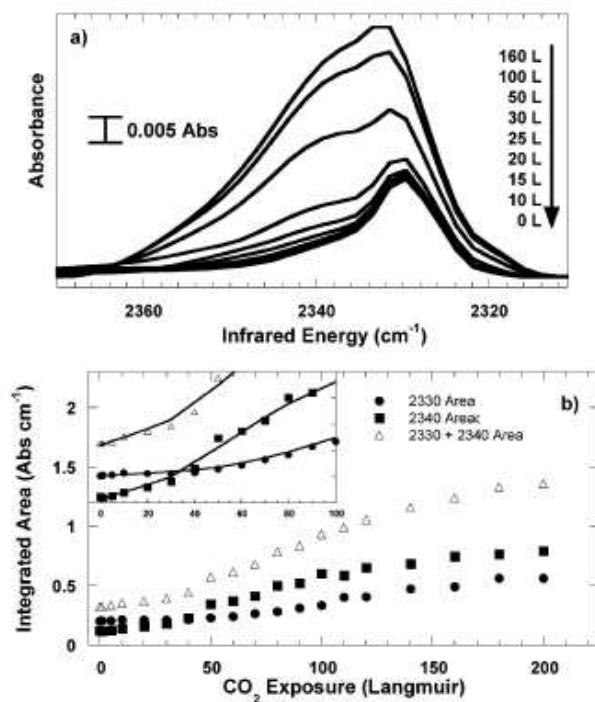
Figure 34: CO_2 dosing experiments for a nanotube sample subjected to heating at 700 K.(a) Infrared spectra as a function of CO_2 exposure. (b) Integrated area of the infrared band determined from deconvoluting the band in (a) as 2 Lorenztians. Inset of (b) is an enlargement of the region below 100 L showing the sequential filling of adsorption sites mentioned in the text

has a complicated dependence on the details of the CO_2 interaction with its adsorbent. The nanotube samples used in this study are of high quality and most of the unwanted carbons are removed by the acid purification procedure [32]. It seems highly unlikely that the effects we see in the current study can be solely due to any carbon impurities in our sample.

The idea of using trapped gases to help assign peaks for IR studies of gas adsorption in carbon nanotubes is interesting. The current study is restricted to CO_2 generated by the sample itself, but there is no fundamental reason why other gases cannot be adsorbed in opened nanotube bundles and then sealed by some chemical or physical procedure;. If this procedure was successful, then studies similar to what has been reported here could be carried out and the similarities/differences between trapped and adsorbed species could be used to help facilitate band assignments. It may also be possible to re-functionalize the defect sites so that other types of gases besides CO_2 are produced and trapped during thermolysis. This approach offers another means to trap gas in nanotube bundles without the extremes of pressure and heat [47].

4.5   SUMMARY

Thermolysis of oxygen-containing functionalities on carbon nanotubes can create CO_2 that becomes permanently trapped in the nanotube bundles. The decomposition of these functionalities and subsequent trapping of CO_2 was studied with infrared spectroscopy. The band of trapped CO_2 is red shifted from the gas phase to 2330 cm^{-1} with a high energy shoulder at 2340 cm^{-1}. At high temperatures, there is evidence for another shoulder at 2220 cm^{-1}. Computer simulations of the trapped CO_2 species show drastic changes in the binding energy distributions and density profiles, which qualitatively explain the frequency shifting, broadening, and integrated intensity changes observed in the infrared spectra. Computer simulations and experiments point to sequential filling of sites for gas-phase CO_2 adsorption on heated tubes with small defect interstitial sites filling before endohedral sites. The limited number of sites available for trapped CO_2 in nanotube bundles is used to facilitate tentative assignments for each of the infrared bands.

5.0 FORMATION OF ODD-NUMBERED CLUSTERS OF CO_2 ADSORBED ON NANOTUBE BUNDLES

The contents of this chapter were taken from Chen, L., and Johnson, J.K., *Phys. Rev. Lett.,* **94**,125701,(2005).

5.1 RESULTS AND DISCUSSION

The study of one-dimensional (1-d) states of matter has been of interest for many years [63]. Single-walled carbon nanotube (SWNT) bundles offer the possibility of realizing a 1-d physical system for gases adsorbed on specific sites on the bundles. In this work we focus on the adsorption of CO_2 on the groove sites of SWNT bundles. The groove sites are defined as the external surface of SWNT bundles where two tubes meet. The groove sites form an effective 1-d trap for molecule adsorption [9, 10, 18]. Experiments indicate that gases will adsorb primarily in the groove sites at low pressures if the nanotubes are closed so that gases cannot access the internal sites [64, 58, 65, 17, 59]. Lasjaunias et al. were the first to claim to observe direct evidence of 1-d behavior for gases adsorbed in SWNTs [66].

Most studies of gas adsorption on SWNT bundles have focused on spherical, or nearly spherical adsorbates, such as noble gases, H_2, and CH_4 [67, 68, 57, 69, 58, 70, 71, 64]. There have been a few recent theoretical and experimental studies of CO_2 adsorption on SWNTs [51, 72, 48, 50, 73, 49, 74, 54]. In this paper we show that CO_2 adsorbed in the groove sites of nanotube bundles exhibits unusual and unexpected quasi-1-d behavior. Our calculations show that CO_2 adsorbed in groove sites at low temperatures forms clusters containing only odd numbers of molecules at finite coverages. Furthermore, the molecules in the individual

clusters are orientationally ordered. The clustering and orientational behavior of the CO_2 molecules is shown to be a result of a delicate balance between the van der Waals (vdW) solid-fluid (sf) forces and the fluid-fluid (ff) quadrupole and vdW forces.

We performed atomistic simulations with model potentials to account for sf and ff interactions. We used the basin-hopping method coupled with the conjugate gradient algorithm [75, 76, 77] to identify the ground state structures of both CH_4 and CO_2 adsorbed in a single isolated groove site. Finite temperature calculations were performed in the canonical ensemble with parallel tempering Monte Carlo [78, 79, 80]. The Lennard-Jones (LJ) potential was used for vdW interactions for both ff and sf potentials. The LJ parameters for the carbons in the nanotubes were taken to be the same as for carbons in graphite [35], $\sigma = 3.4$ Å and $\epsilon/k = 28.0$ K, where σ and ϵ are the LJ size and well depth parameters, respectively, and k is the Boltzmann constant. Methane was treated as a spherical molecule, with LJ parameters $\sigma = 3.72$ Å and $\epsilon/k = 161.35$ K [9]. Four different CO_2 potentials were considered, namely, the EPM and EPM2 models of Harris and Yung [55], the Potoff and Siepmann (PS) potential [81] and the Arab et al. potential [51]. Each potential included LJ sites at each atom center and point charges to account for the quadrupole moment. Lorentz-Berthelot combining rules were used to compute the LJ parameters for the sf potential. We have ignored any charge-related interactions between CO_2 and nanotubes (charge-induced dipole) as these are expected to be small since CO_2 lacks a permanent dipole moment [51]. The sf potential was smoothed by integrating over the positions of all the carbon atoms in the nanotubes. Calculations using atom-explicit nanotube potentials gave nearly identical results with the smoothed potentials. The EPM, EPM2, and PS potentials all give good agreement with experimental data for CO_2-graphite interactions. The Arab et al. potential underestimates CO_2-graphite energetics. The experimental zero-coverage binding energy is 17.2 kJ/mol [82]; the values from simulations are 17.1, 16.6, 16.6, and 13.8 kJ/mol for the EPM, EPM2, PS, and Arab et al. potentials, respectively. The experimental isosteric heat at full monolayer coverage of CO_2 on graphite is 25.3 kJ/mol [83]; simulations give 26.6, 26.2, 26.0, and 22.3 kJ/mol from the EPM, EPM2, PS, and Arab et al. potentials, respectively. The zero-coverage isosteric heat for CO_2 on SWNTs computed from the EPM2 model is 22.7 kJ/mol, in good agreement with the experimental value of 22.5 kJ/mol [72]; the value

computed from the Arab et al. potential is 20.6 kJ/mol [51]. Simulation results reported here are for the EPM2 potential, unless otherwise specified.

Previous calculations have shown that at low coverages spherical molecules are adsorbed in the groove sites, forming a 1-d phase [9, 10]. The ground state for n spherical molecules in a single groove site is for the n molecules to form a cluster to maximize the ff attractive interaction. At high coverages, when the 1-d chain completely fills the groove site, molecules are forced out of the groove to form zig-zag or three-strip phases [9, 10]. Hence, the binding energy monatonically increases as molecules are added to the 1-d cluster, until the groove site is filled. The binding energy for CH_4 adsorbed in the groove site is shown in Fig. 35 for up to $n = 10$ molecules. We define the binding energy as $E_b = \sum_{i=1}^{n} E_i(\text{gas phase}) - E(\text{cluster})$, where $E_i(\text{gas phase})$ is the energy of each of the adsorbent molecules in the gas phase and $E(\text{cluster})$ is the ground state energy of the cluster adsorbed in the groove site. Note that this definition results in $E_b > 0$ for a bound cluster.
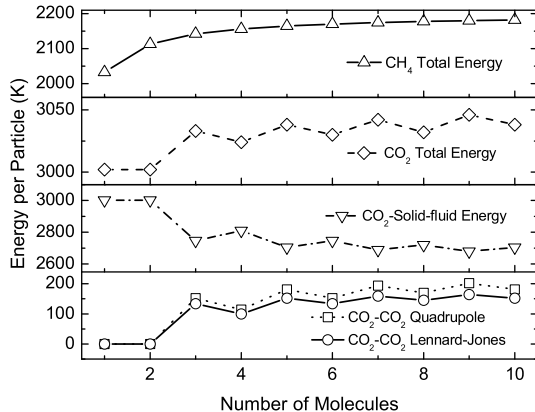
Figure 35: Binding energies for CH_4 and CO_2 adsorbed in the groove site as a function of the number of molecules in the groove. The top panel is for CH_4. The diamonds give the total binding energy, and the down triangles give the contribution to the binding energy due to solid-fluid interactions. The circles and squares give the LJ and Q-Q fluid-fluid contributions to the binding energy, respectively. The lines are drawn as a guide to the eye.

The gas phase CO_2 dimer is known to form a slipped parallel configuration in the ground state from both experiment and theory [84, 85]. This configuration results from a competition between vdW and electrostatic interactions, with the vdW forces favoring a parallel conformation to maximize the interaction energy and the quadrupole-quadrupole (Q-Q) term favoring a "T" conformation. The parallel and end-to-end configurations have repulsive interactions [85]. In the ground state, a single CO_2 in a groove has its molecular axis parallel with the groove, maximizing the sf interactions. This is shown in Fig. 35 for $n = 1$. This is also the ground state for $n = 2$ (Fig. 35). The CO_2-CO_2 distance is maximized in order to minimize the Q-Q repulsion imposed by the end-on configuration. The end-on Q-Q interaction energy is given by

$$U_{QQ}(r) = \frac{3\Theta^2}{(2\pi\varepsilon_0)r^5}, \tag{5.1}$$

where Θ is the CO_2 quadrupole moment and ε_0 is the vacuum permittivity. Note that Eq. (5.1) is longer ranged than the LJ potential, which decays as r^{-6}. The attraction due to the LJ potential for the CO_2 dimer is always smaller in magnitude than the Q-Q repulsion for the end-on configuration. Hence, there is no bound state for the CO_2 dimer confined to a groove site. The dimer could adopt a configuration that gives an attractive Q-Q interaction by one or both of the molecules rotating out of the groove site. However, such rotations are energetically unfavorable because of the substantial sf potential energy penalty (~ 750 K) associated with the rotation of a single molecule out of the groove site. Hence, the binding energy for the dimer shown in Fig. 35 is almost identical to the $n = 1$ case; the ff energy is virtually zero and the total binding energy is therefore equal to the sf energy. In contrast, Arab et al. predict that CO_2 dimers can form in the groove sites by forming a slipped parallel configuration that is only slightly perturbed from the gas phase [51]. The dimers form when using the Arab et al. potential because the sf potential used by Arab et al. is too weak compared with the other potentials.

Extrapolating from the dimer results one would assume that there is no bound state for a cluster of any number of molecules, n in the groove site. This is not the case. For $n = 3$ the ground state is a cluster of three molecules, with the two molecules on the ends of the cluster oriented parallel with the groove site and the middle molecule rotated up with $\theta = 90°$, where θ is the angle between the CO_2 molecular axis and the groove site axis. The trimer

78

also exhibits azimuthal ordering with the middle molecule lying against the surface of one of the nanotubes making up the groove site, at an angle of about 30° from the surface normal of the plane containing the nanotube axes. This configuration results in a sf energy penalty for the rotated molecule that is more than compensated for by the increased ff interactions from the two "T" configurations (down-up-down). Both the Q-Q and LJ interactions are needed to make up for the loss of potential energy due to rotating the central molecule out of the groove site. The sum of the Q-Q and LJ energies is larger than the decrease in the sf potential, so that the total binding energy increases for $n = 3$ relative to $n = 2$.

The ground state for $n = 4$ molecules is a cluster of three molecules with the same configuration as the $n = 3$ case and with the fourth molecule separated from the trimer. Roughly speaking, two pairs of favorable Q-Q and LJ interactions are required to compensate for the penalty of rotating one CO_2 out of the groove site. Therefore, every stable cluster must have the terminal molecules of the chain lying down in the groove. The only way to accomplish this is for each cluster to have an odd number of molecules. Thus, the $n = 4$ system splits into a trimer and a monomer. The sf binding energy shown in Fig. 35 increases slightly from $n = 3$ to $n = 4$ (down triangles) while the ff terms both decrease (squares & circles). The decrease in the total binding energy on going from $n = 3$ to $n = 4$ is due to the decrease in ff binding. When n is odd the ground state is always a single cluster with the end molecules parallel to the groove axis and alternating molecules in the interior of the cluster rotated out of the groove site. When n is even the system must split into two clusters, each containing an odd number of molecules, in order to maximize the binding energy. The total energy is therefore an oscillating function of the number of molecules in the system, as shown by the diamonds in Fig. 35. A single cluster containing an even number of molecules has a binding energy that is over 100 K less than that obtained by splitting the cluster into two odd-numbered clusters.

We have developed a simple order parameter to measure the orientational order in the system,

$$P(n) = \frac{2}{n} \sum_{i=1}^{n} \cos \theta_i - 1. \tag{5.2}$$

If all the molecules have their axes aligned with the groove site then $\theta_i = 0$ and $P(n) = 1$. If every other molecule is rotated into the $\theta = 90°$ position then $P(n) = 0$. In the limit of full coverage $P = 0$ since every other molecule should be rotated perpendicular to the groove axis, as noted by Matranga et al. [49]. The order parameter computed from basin hopping simulations is shown in Fig. 36. We see that $P(1) = P(2) = 1$ and there after the order parameter oscillates while decreasing asymptotically toward $P(\infty) = 0$. The oscillation can easily be understood. When n is odd there are $(n+1)/2$ molecules with $\theta = 0$ and the remainder with $\theta = 90°$, giving $P = 1/n$. When n is even there are two clusters, each with the first and last molecules parallel and every other molecule after that rotated up. Therefore, there are $n/2 + 1$ molecules having $\theta = 0$ and the remainder having $\theta = 90°$, giving $P = 2/n$. Therefore,

$$
P(n) = \begin{cases} \frac{1}{n} & n \text{ odd} \\ \\ \frac{2}{n} & n \text{ even} \end{cases}. \tag{5.3}
$$

These two functions are shown in Fig. 36 as the solid $(1/n)$ and dashed $(2/n)$ lines. This simple prediction is seen to match the calculated results almost exactly. Carbon dioxide without the quadrupole (charges set to zero) forms clusters of any number with every molecule lying flat in the groove. The calculated order parameter, shown as the diamonds in Fig. 36, is constant at $P = 1$.

Snapshots for systems with $n = 6, 7$, and 8 CO_2 molecules in a single groove are shown in Fig. 37. For $n = 6$ two trimer clusters are formed. For $n = 8$ the lowest energy is attained by splitting the cluster into a 5-mer and a trimer. For $n = 7$ and 8 the azimuthal angles of the $\theta = 90°$ molecules alternate between $\pm 30°$. The reason for this is that the next nearest neighbor Q-Q interactions are repulsive if all the azimuthal angles are the same. The energy is lowered by about 2 K per molecule by having every other $\theta = 90°$ molecule resting against the opposite nanotube.

Simulations in groove sites of (6,6), (8,8), (9,9), (10,10), and (11,11) nanotube bundles were carried out. The energetics were similar in each case and the selection of odd-numbered clusters was not influenced by the identity of the nanotube. We conclude that the nanotube radius does not play an important role, at least for radii ranging from 4.07 to 7.46 Å.
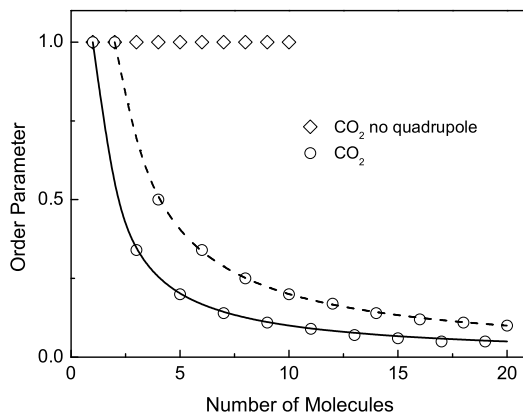
Figure 36: Order parameters, computed from Eq. (5.2), for CO_2 without the quadrupole term (diamonds) and with the full potential (circles). The solid and dashed lines are computed from the odd and even series, respectively, given by Eq. (5.3).

We studied clustering at finite temperatures by using parallel tempering Monte Carlo [78, 79, 80]. We found that large odd-numbered clusters tend to dissociate to smaller clusters containing primarily odd numbers of molecules. We have computed the probabilities of observing a cluster of a given number of molecules starting from a specific cluster as a function of temperature. The probabilities are very sensitive to the details of the potentials used. As an example, we here discuss the results starting from a 5-mer cluster. The 5-mer dissociates into a trimer and two monomers, with small probabilities of observing 4-mers and dimers at temperatures of 50 K and below. Calculations gave probabilities of observing a 5-mer cluster at 10 K of 0.86, 0.21, and 0.84 for the EPM, EPM2, and PS potentials, respectively. Although the EPM2 and PS potentials give very similar bulk phase diagrams [55, 81] and sf energies, there is a marked difference in the probabilities of observing an intact 5-mer between these two potentials. The reason for this is that the EPM2 and PS potentials have a slightly different balance of Q-Q and LJ potentials. Hence, experimental observation of clusters at 10 K could provide a very sensitive test of ff and sf potentials. At 50 K the potentials are in better agreement. The probability of observing a 5-mer is below

81
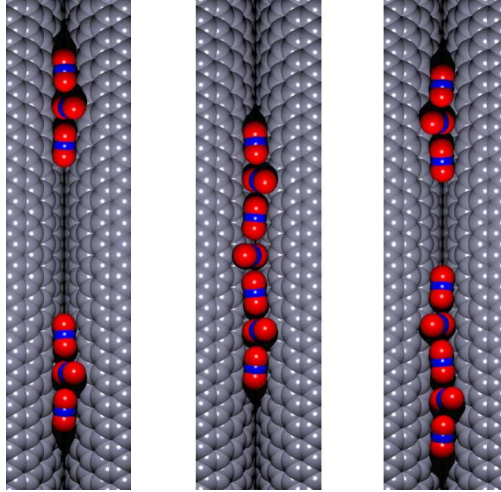
Figure 37: (color online) Snapshots of optimized CO_2 adsorbed in a single groove. (left) $n = 6$ (middle) $n = 7$, and (right) $n = 8$ CO_2 molecules.

0.1 for all three potentials. The probabilities of observing a trimer at 50 K are 0.41, 0.34, and 0.38 for the EPM, EPM2, and PS potentials, respectively. These probabilities indicate that odd-numbered clusters may be experimentally observable by AFM at temperatures lower than 50 K.

Manybody interactions may change the ff and sf energies [29]. We have modeled many-body effects by changing the ff potential by $\pm 30\%$ and the sf potential by $\pm 20\%$. Changes to the ff potential do not dramatically affect the tendency to form odd-numbered clusters. However, a decrease in the sf of 20% allows even-numbered clusters to form. This reaffirms the observation that the clustering behavior is a sensitive measure of the potential.

Stepped crystal surfaces provide quasi-1-d environments for physisorption of gas molecules that are in some ways similar to SWNT groove sites. We have investigated stepped surfaces of several crystals. However, the step edge sites did not lead to the exclusive formation of odd-numbered clusters, because the energy barrier for rotating a molecule away from the step edge is much lower than for rotating out of a groove site.

6.0 FIRST PRINCIPLES STUDY OF ADSORPTION AND DISSOCIATION OF CO ON W(111)

The contents of this chapter were taken from Chen, L. and Johnson, J.K., *J. Phys. Chem. B*, **110**, 1344(2006).

6.1 INTRODUCTION

CO adsorption on tungsten and modified tungsten surfaces has been studied both experimentally and theoretically because of their potential use in methanol reforming and fuel cell technology.[86, 5] The temperature programmed desorption (TPD) of CO on most transition metal surfaces shows a low temperature α state and several high temperature β states. In the conventional picture of CO binding to transition-metal surfaces, [87, 88, 4] The α state is assigned to CO adsorbed in an end-on orientation with the carbon end toward the surface, while the β state is assigned to the species adsorbed in an orientation that is tilted with respect to the surface normal and with both C and O interacting with the surface. Chen and coworkers[89] studied CO and H_2O adsorbed on W(111), C/W(111) and C/O/W(111) surfaces using TPD and high-resolution electron energy loss (HREEL) spectroscopy. They observed desorption and vibrational spectra. Their results imply that the α state CO desorbs molecularly from clean W(111) at about 293 K, while the low frequency β state CO dissociates at room temperature, and recombines to form molecular CO around 870 K. In contrast, dissociation is not observed for CO on the carbon modified W(111) surface, denoted as C/W(111). Lee and coworkers[90] have reported TPD, ultraviolet photoelectron spectroscopy, and x-ray photoelectron spectroscopy experiments for CO adsorption on the

clean W(111) surface. In contrast to the work of Chen et al., they suggested that β state CO molecules do not dissociate.[90]

We have found only one theoretical study of CO on the W(111) surface in the literature.[91] Ryu et al. used the atom superposition and electron delocalization molecular orbital theory,[92, 93] which is a corrected extended Hückel method, in their calculations. They used only three layers of atoms in their model, which is the minimum possible number of layers for a bcc (111) surface. Ryu et al. studied the energetics of CO adsorbed on various binding sites and configurations. Their reported binding energies are much higher than experimental values inferred from TPD.[89] Furthermore, they claimed that it is unclear if the β state CO leads to dissociation. In the present paper, we have used first principles density functional theory (DFT) to study the adsorption of CO on the W(111) surface. We have computed binding energies, vibrational frequencies, and diffusion and dissociation pathways of CO on clean and carbon pre-adsorbed W(111) surfaces. We compare our results with experimental data where possible.

6.2   THEORETICAL CALCULATIONS

Density functional theory calculations were performed using the generalized gradient approximation. The Vienna ab initio simulation package [94, 95, 96] was used for all calculations. The revised Perdew Burke Ernzerhof (rPBE) [97, 98] exchange-correlation functional was used because we found that the PW91 functional[99] gave binding energies for CO on W(111) that were 0.2-0.4 eV greater than those computed from the rPBE functional. It is known that PW91 predicts binding energies for CO on metal surfaces that are too high compared with experiments.[100] The electron-ion interactions were described by PAW (Projector Augmented Wave) pseudopotentials.[101, 102] Electron smearing was employed using the Methfessel-Paxton technique, with a smearing width of $\zeta = 0.1$ eV, in order to minimize the errors in the Hellmann-Feynman forces due to the electronic free energy. All calculated energies are extrapolated to $T = 0$ K.

The Brillouin zone was sampled with 13 irreducible k-points (5×5×1 mesh) generated from the Monkhorst-Pack scheme.[103] We have tested the k-point convergence by comparing calculations with 54 and 13 irreducible K-points. We found the energy to be converged to within 0.01 eV. An energy cutoff of 400 eV was used in all calculations. The rPBE calculated lattice constant for bulk tungsten is 3.18 Å, which agrees well with the experimental values of 3.17 Å. The calculated gas phase CO bond length is 1.14 Å, which also agrees well with the experimental value of 1.13 Å.

The binding energy is defined as $E_b = E_a + E_{slab}$ - $E_{a/slab}$ where the three terms on the right-hand side are the energy of an isolated molecule or atom, the energy of the clean W(111) surface, and the energy of the slab with the adsorbed molecule or atom, respectively. A positive value for E_b corresponds to a stable adsorption using this definition.

Vibrational frequencies were calculated by diagonalizing the Hessian matrix of selected atoms. The Hessian matrix was calculated within VASP by a finite difference method. The atoms in the top four W layers and CO were independently displaced by 0.02 Å along each Cartesian coordinate direction. We compared C-O stretching frequencies calculated by allowing all W atoms in the first four layers to move with those computed by fixing all W atom positions. The C-O frequencies were the same to within a few wavenumbers, indicating that coupling of the C-O vibration to the underlying W lattice is negligible.

The nudged elastic band (NEB) method of Jónsson and co-workers [104, 105] was used to compute diffusion and dissociation pathways. Initial and final states were chosen and the number of images was increased to achieve a smooth curve. At least eight images were used for each calculation.

6.3   RESULTS AND DISCUSSIONS

6.3.1   Surface relaxation

We begin by discussing the surface relaxation of the clean W(111) surface as a function of the number of layers. In each calculation, we used a supercell containing a 10 Å vacuum space and kept the bottom three layers fixed. The surface relaxation was characterized by monitoring

the interlayer relaxation with respect to the bulk interlayer spacing. The interlayer spacing is 0.914 Å for the unrelaxed W(111) surface. Note that this is much smaller than that of the W(100) slab, which is 1.59 Å. Table 5 presents the calculated relaxation of the W(111) slab and the thickness of the supercell. F_{ij} is the fractional change in the layer spacing. A triplet relaxation pattern was found with substantial contraction of the first two layer spacings and expansion of the third layer spacing. In contrast, the relaxation of other low-index surfaces is relatively small and follows a different oscillatory pattern. We have calibrated the accuracy of our DFT calculations by computing the relaxation of the W(110) and W(001) slabs and comparing our calculations with experimental data. Table 6 summarizes the calculated and experimentally measured [106] relaxation of the (110) and (001) surfaces. The agreement between experiments and calculations is excellent, giving us confidence in our W(111) results. The unusual relaxation pattern of (111) surfaces has been studied by Xu and coworkers using tight-binding and local density approximation DFT. [106, 107] There are no experimental data for interlayer relaxation of the W(111) surface, to the best of our knowledge.

The data in Table 5 indicate that a large supercell with at least seven layers is necessary to accurately model the surface relaxation of W(111). A model containing only six layers predicts that all relaxed layers will contract (see Table 5). This is mainly due to the very small interlayer spacing along the $\langle 111 \rangle$ direction of bcc metals. The data in Table 5 also indicate that the calculated results with seven layers are well converged; including more layers does not improve the accuracy dramatically. In the subsequent calculations, therefore, we chose to use a supercell containing seven W layers and a vacuum spacing of 10 Å.

6.3.2 CO adsorption

We have calculated the binding energies and vibrational frequencies of CO adsorbed on the W(111) surface in various binding sites and configurations. Figure 38 shows a schematic of the W(111) surface; the triangle represents the reduced unit cell. The light spheres, numbered 1-4, represent the first layer W atoms, while the medium and dark colored spheres, numbered 5 and 6, represent the second and third layer W atoms, respectively. We have investigated three end-on (α) configurations and four inclined (β) configurations for CO bound

Table 5: Interlayer relaxation of the W(111) surface as a function of number of layers in the model. The data in parenthesis are cited from the literature.[107] F_{ij} denotes the fractional change in the layer spacing of the relaxed thin films.

Number of layers	Thickness(Å)	$F_{12}(\%)$	$F_{23}(\%)$	$F_{34}(\%)$	$F_{45}(\%)$
6	14.57	-13.5	-10.5	-18.5	$-$
7	15.48	$-19.9\ (-17.5)$	$-23.8\ (-14.5)$	$18.1(11.2)$	$-$
9	17.31	$-23.3\ (-23.5)$	$-21.4\ (-17.4)$	$14.2(22.0)$	$-1.4(-5.5)$
11	19.14	-24.6	-23.8	18.1	-3.5

Table 6: Interlayer relaxation of the (001) and (110) surfaces of W. F_{ij} denotes the fractional change in the layer spacing of the relaxed thin films. Experimentally measured data from Xu and Adams[106] are also shown.

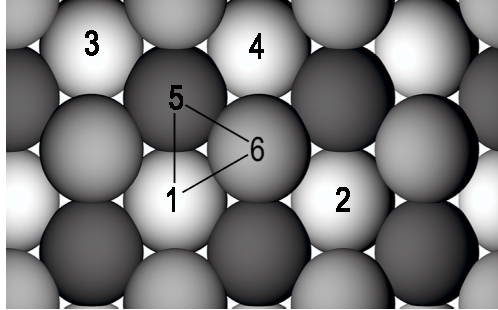| Surfaces	$F_{12}(\%)$	Exp.[106]	$F_{23}(\%)$	Exp.[106]
(001)	-8.04	-7	4.54	3.9
(110)	-3.08	-2.1	0.87	0.7

Figure 38: Schematic of the W(111) surface. The triangle represents the reduced unit cell. Light spheres (labeled 1-4) are the first layer W atoms, the black spheres (e.g., 5) represent second layer W atoms, and the gray spheres (e.g., 6) represent the third layer W atoms.

to the W(111) surface. The top and side views of the most favorable inclined adsorption configuration, C-2:O-1 are shown in Figure 39. The notation for inclined adsorption, C-n:O-m indicates that the carbon is interacting with the nth W atom, while oxygen is interacting with the mth W atom as numbered in Figures 38 and 39. Only four layers are shown in Figure 39, although seven layers were used in the calculations.

We have performed calculations for CO adsorption on (1×1) and (2×2) ad-layers, corresponding to coverages of 1 and 1/4 ML, respectively. The coverage effect is quite small, giving less than 0.1 eV difference in E_{b}. This is because the (111) surface of a bcc metal is very open. In contrast, the (111) surface of a fcc metal is close-packed and the coverage has a significant effect on the binding energy. [108]

Table 7 shows that the 4th–7th layers play a very important role in the adsorption. For example, on the one-fold site, the calculated binding energy without taking 4th–7th layers into account gives an error of 0.99 eV. Therefore, the results of Ryu et al., [91] computed with only three layers, are not accurate.

We have compared our calculations with two different experimental studies of CO on the W(111) surface.[89, 90] These studies present TPD spectra that are not exactly consistent with one another. We have transformed the TPD results to binding energies, by using both a standard Redhead analysis [109] and the Polanyi-Wigner equation. [110, 111] Both methods give very similar results. Chen and co-workers [89] found that CO molecularly desorbs at
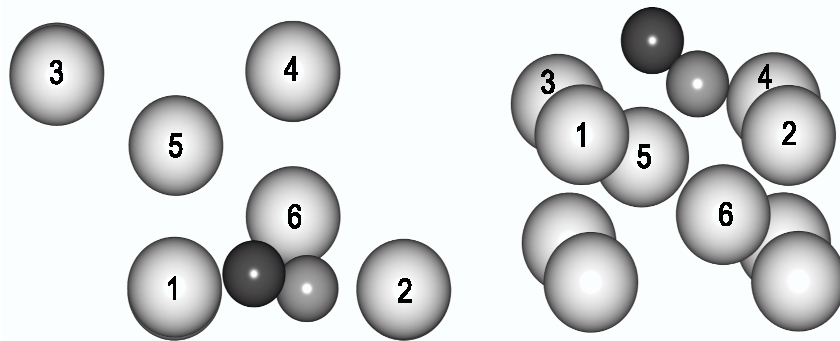
Figure 39: The inclined CO (β) state with the highest binding energy. The left figure is the top view and the right figure is side view. The black sphere is oxygen and the gray sphere is carbon. Only the top four W layers are shown.

293 K at a heating rate of 3 K s^{-1}, which corresponds to a binding energy of 0.79 eV. Lee and co-workers [90] observed the desorption of CO at 400 K at the heating rate of 8 K s^{-1}, which corresponds to a binding energy of 1.13 eV. Better estimates of the binding energy can be made if the coverage and heating rates are varied in the experiments. This was not done in either of the experimental papers, and therefore, we use a simple Redhead analysis to give reasonable estimates for the binding energies from the information available.

Chen and coworkers have measured HREEL spectra of CO adsorption on the W(111) surface.[89] Two dominant peaks are observed close to 400 cm^{-1} and 2060 cm^{-1} for $T \leq$ 230 K. In addition, a broad band ranging from about 1000 to 1600 cm^{-1} is also present. According to previous experimental and theoretical studies of CO adsorption on other early transitional metals, i.e., Fe(110) and Fe(111) surfaces[87, 88], the $\sim$ 400 cm^{-1} peak is assigned to the W-CO vibrational mode, $\sim$ 2060 cm^{-1} to the C-O stretching mode of α state CO, and the broad band to the C-O stretching mode in β state CO.

Our calculated binding energies and vibrational frequencies for CO adsorbed on different sites are reported in Table 8. In accordance with convention, we define the α state as end-on adsorption with the C-O bond oriented parallel to the surface normal and the β state as being inclined with respect to the surface normal. The two-fold bridge state is similar to the C-5:O-6 state, but has a smaller tilt angle. Among the seven binding sites

considered, the β state CO in the C-2:O-1 configuration has the highest binding energy (1.79 eV) and also the lowest C-O stretching frequency (1318 cm^{-1}). The binding energies for β states range from 1.6 to 1.79 eV and display stretching frequencies from 1318 cm^{-1} to 1645 cm^{-1}. These values are in reasonable agreement with the experimentally observed vibrational band between about 1000 to 1600 cm^{-1}.[89] The experimental and calculated gas phase C-O frequencies are 2143 cm^{-1} and 2117 cm^{-1}, respectively. Hence, the red shifts measured experimentally range from about 500 to 1100 cm^{-1}, while the calculated red shifts range from about 470 to 800 cm^{-1}. The large red shifts are due to the weakening of the C-O triple bond,[91, 4] which indicates that the β state CO is the mostly likely precursor to dissociation.

The one-fold (on-top) and three-fold shallow are the most favorable α sites; both have binding energies of of 1.37 eV (Table 8). In both cases, the adsorbed CO pulls the substrate W atom 0.04-0.06 Å out of the surface. These binding energies are somewhat larger than energies calculated from Redhead analysis of the TPD data of Chen and coworkers (0.79 eV) and of Lee et al. (1.13 eV). The discrepancy between our results and the experimental data may be due to limitations of the Redhead analysis or to overbinding on the part of the DFT calculations. The calculated C-O vibrational frequencies for the two sites are 1930 and 1722 cm^{-1}, respectively, as shown in Table 8. These frequencies are considerably lower than the experimental peak at $\sim$ 2060 cm^{-1}, which is red shifted by 83 cm^{-1} from the gas phase C-O stretch.[89] The larger red shifts seen in the calculations may be the result of DFT overbinding. The three-fold deep site has a smaller E_{b} but a much larger C-O frequency red shift.

6.3.3 Carbon and oxygen adsorption

We have studied the structures and energetics of adsorbed C and O atoms on the W(111) surface as part of our study of CO dissociation. The calculated binding energies are summarized in Table 9, which lists the binding energies of the atoms at 1/4 ML coverage and δE, the energy relative to the most favorable binding site. The one-fold on-top site is the most favorable binding site for an oxygen atom, while the two-fold bridge site is the most favorable

Table 7: Binding energy (eV) of CO adsorbed on the W(111) surface as a function of the numbers of layers. The data in the last column are from the literature.[91]

	Number of Layers						
Site	3	4	5	6	7	8	3*
One-fold	2.46	2.23	1.37	1.40	1.37	–	2.89
Three-fold shallow	2.15	2.21	1.43	1.37	1.37	–	2.53
Three-fold deep	1.49	1.35	1.41	1.05	0.89	0.93	1.99
Inclined C-2:O-1	–	–	–	2.14	1.79	1.74	4.5

*Ryu et al.[91]

Table 8: Binding energies and vibrational frequencies of CO adsorbed on the W(111) surface. The red shifts are measured relative to the computed gas phase CO vibrational frequency of 2117 cm^{-1}.

Site	State	E_b (eV)	Frequency (cm^{-1})	Red shift (cm^{-1})
One-fold	α	1.37	1920	197
Three-fold shallow	α	1.37	1722	395
Three-fold deep	α	0.89	1560	557
Two-fold bridge	β	1.62	1645	472
Inclined C-2:O-1	β	1.79	1318	799
Inclined C-5:O-6	β	1.71	1386	731
Inclined C-5:O-4	β	1.60	1467	650

binding site for a carbon atom. The co-adsorption of C and O on their most favorite sites has also been examined and the optimized configuration was used as the final state for CO dissociation calculations. The co-adsorption energies are the same as the 1/4 ML coverage binding energies to within a few meV. This is consistent with the observation above that the coverage effect for CO adsorption in going from 1/4 to 1 ML is very small. In contrast, Li et al. found that the coadsorption interaction energies for C and O on the Ni(111) surface are larger than 1 eV.[112]

The carbon modified W(111) surface was studied by Chen and coworkers because of its potential application in fuel cells. [89] Their TPD study shows that the carbon modified surface is apparently unable to dissociate CO. We have used the carbon pre-adsorbed W(111) surface as a model for the the carbon modified surface in our calculations in order to understand why the carbon modified surface is nonreactive toward CO dissociation. Our findings are discussed in the following section.

Table 9: Binding energies and relative stabilities for atomic carbon and oxygen adsorption on the W(111) surface. All energies are in eV.

Site	C		O	
	E_b	δE	E_b	δE
One-fold	5.31	2.04	6.29	0
Three-fold shallow	5.30	2.11	5.50	0.79
Three-fold deep	6.20	1.21	6.01	0.28
Two-fold bridge	7.41	0	5.96	0.33

6.4 CO DISSOCIATION

Previous studies have shown that perpendicularly adsorbed CO (α state) desorbs molecularly without dissociation at high temperature.[113] The inclined CO (β) is believed to dissociate due to strong interactions with the d-band of the substrate metals. As mentioned above,

our calculations show that the β states have higher binding energies and larger red shifts than the α states, which indicates weakening of the C-O bond. Consequently, we have calculated the minimum energy paths corresponding to dissociation of CO starting from three inclined configurations. Three possible minimum energy paths were constructed by connecting three initial β states to final states with atomic carbon and oxygen adsorbed in their most favorable binding sites. The last three β states listed in Table 8 were chosen as the initial states for dissociation calculations. In each NEB calculation, we used from 8 to 14 linearly interpolated images along the reaction path in addition to the initial and final points. The reaction pathway starting from the inclined configuration C-2:O-1 is shown in Figure 40. The left and right insets show the initial and final states, respectively. Fitting the data along the energy curve yields a dissociation barrier of 0.82 eV. Chen and coworkers [89] found evidence that CO dissociates rapidly around 330 K. Our calculated activation energy agrees very well with this experimental observation. Figures 41 and 42 show the minimum energy dissociation pathways from the inclined configurations C-5:O-6 and C-5:O-4, respectively. The calculated activation energies are 1.19 and 1.41 eV, respectively. The C-2:O-1 configuration is the most likely precursor to dissociation because it has a significantly lower activation energy than the other two β states identified in this work. All the transition states observed in our calculations are "early" in the sense that the structure of the transition state is quite similar to the initial state. For example, the C-O bond length increases from 1.28 Å to 1.46 Å in going from the initial to the transition state for C-2:O-1 in Figure 40.

An analysis of the structure of CO in the C-2:O-1 configuration shows that the carbon atom is located close to the two-fold bridge site, but closer to the W atom labeled 2 in Figure 38. According to our atomic carbon and oxygen adsorption calculations, carbon atoms are most likely to occupy the two-fold bridge sites, having a binding energy that is 1.21 eV larger than the next most favorable site. Therefore, adsorbed carbons may block the adsorption of dissociative β state CO molecules. Moreover, C/W(111) has all favorable final states for C blocked so that dissociation from any β state is inhibited. Only the one-fold sites are accessible to CO adsorption on the carbon modified surface. This blockage mechanism helps explain the experimental observation that the C/W(111) surface is inactive toward to CO dissociation. [89]

Figure 40: Dissociation of CO on the W(111) surface from the C-2:O-1 β state. The insets show the initial (left) and final (right) states. The line is drawn as a guide to the eye.

Figure 41: Dissociation of CO on the W(111) surface from the C-5:O-6 β state. The insets show the initial (left) and final (right) states. The line is drawn as a guide to the eye.
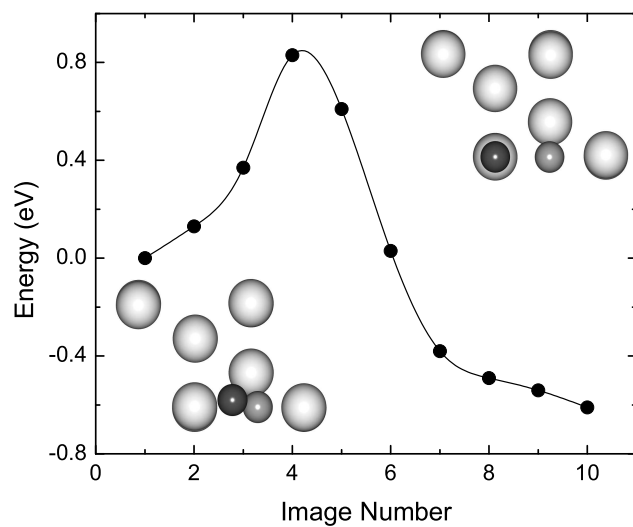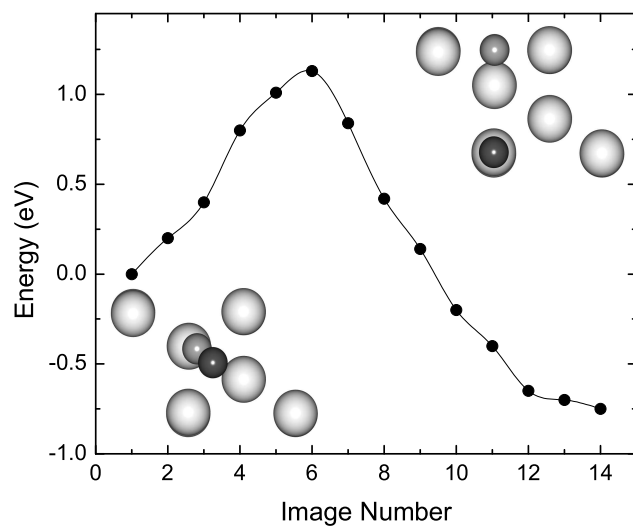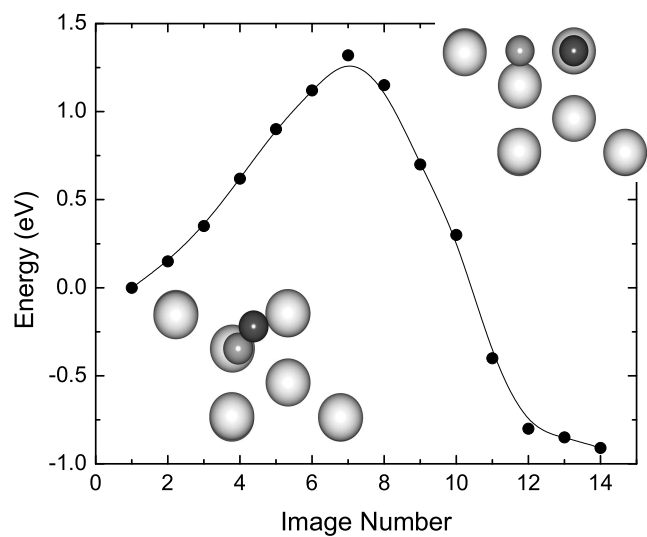
Figure 42: Dissociation of CO on the W(111) surface from the C-5:O-4 β state. The insets show the initial (left) and final (right) states. The line is drawn as a guide to the eye.

6.4.1 CO/C/O diffusion

We have investigated the diffusion of CO, atomic oxygen and atomic carbon on the clean W(111) surface by using the NEB method.[104, 105] For each adsorbate, we selected the most favorable binding state as the initial state and the second most favorable binding state as the final state. Diffusion from the three-fold shallow site to the one-fold site has a calculated barrier energy of 0.76 eV. This low activation barrier suggests that the migration of CO between various end-on (α state) configurations is facile at moderate temperatures. The diffusion energy barrier from the C-2:O-1 β site to the one-fold α site is plotted in Figure 43. The diffusion barrier is about 1.42 eV in going from the β to the α state, and about 1 eV for the reverse path. The calculated diffusion barrier for a carbon atom from the two-fold bridge site to the three-fold deep site is 1.91 eV. The calculated diffusion barrier for an oxygen atom moving from the one-fold site to the three-fold deep site is 0.69 eV. The strong binding energy and relatively high diffusion barrier of carbon indicate that carbon atoms are effectively frozen in the two-fold site at moderate temperatures. The hopping rate for C moving from the two-fold bridge site to the three-fold deep site is 8.2×10^{-20} s^{-1} at room temperature, assuming a prefactor of 10^{13} s^{-1}. In contrast, we predict that oxygen atoms are able to diffuse freely on the surface at room temperature. For example, the hopping rate for O moving from the one-fold to the three-fold deep site is 1.7 s^{-1} at 300 K. It would be interesting to see experimental verification of our predictions, perhaps by STM measurements.

6.5 CONCLUSIONS

We have studied the adsorption and diffusion of C, O and CO on the W(111) surface using density functional theory. A summary of our findings is presented schematically in Figure 44 as an energy landscape diagram for a few selected states. We have computed dissociation pathways for CO on the W(111) surface. Atomic oxygen is preferentially adsorbed on the one-fold on-top site, but can diffuse to other adsorption sites at room temperature. In contrast, atomic carbon is most strongly adsorbed on the two-fold bridge site and is essentially
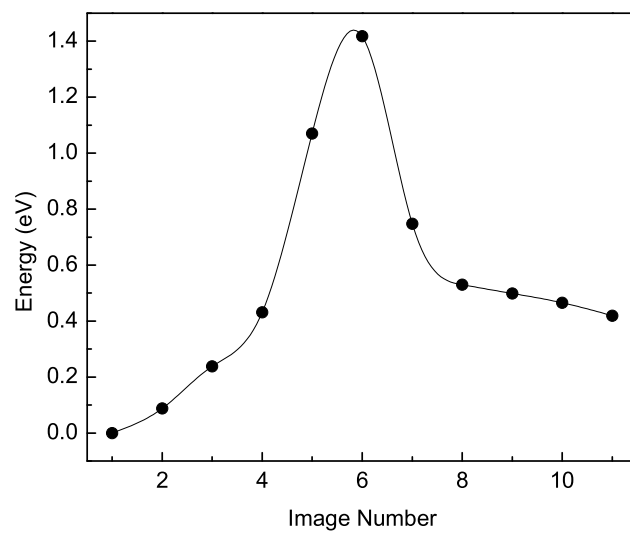
Figure 43: Diffusion pathway of CO on the W(111) surface from the C-2:O-1 β site to the one-fold α site. The line is drawn as a guide to the eye.
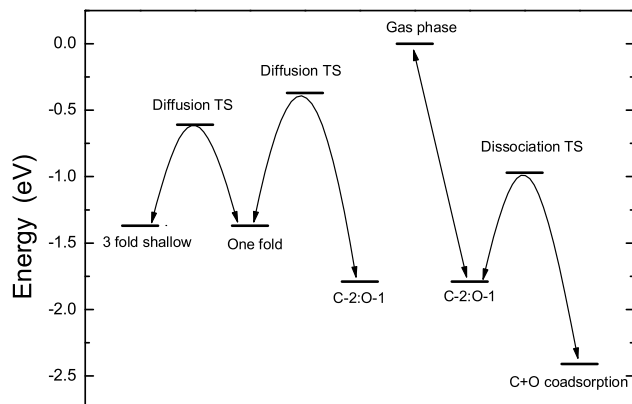
Figure 44: A schematic of the energy landscape for adsorption, diffusion, and dissociation. Only a few selected states are shown.

immobile on the surface except at elevated temperatures. Molecular CO can be adsorbed in α states, with the C-O bond aligned parallel to the surface normal, or in β states, inclined to the surface normal. The β states have the highest binding energies, the largest C-O stretching frequency red shifts, and are predicted to be the precursor states for dissociation. The lowest calculated dissociation barrier is 0.82 eV, which is consistent with experimental TPD studies. We predict that CO dissociation will result in a self-poisoning process, whereby C blocks further dissociation of CO on the surface. This blockage also explains the experimental observation that the C/W(111) surface is inactive toward CO dissociation.[89]

Finally, our calculations account for the experimental observation that dissociated CO on the W(111) surface does not recombine until ~ 900 K.[89] We take the dissociation and recombination of the C-2:O-1 β state, shown in Figure 40, as an example. The dissociation energy barrier is $E_{\mathrm{dis}} = 0.82$ eV, the recombination energy barrier is $E_{\mathrm{rec}} = 1.44$ eV, and the desorption energy, given in Table 8, is $E_{\mathrm{des}} = 1.79$ eV. The desorption rate can be approximated as

$$r_{\mathrm{des}} = \frac{k_{\mathrm{rec}} \, k_{\mathrm{des}}}{k_{\mathrm{dis}} + k_{\mathrm{des}}}[\mathrm{C}][\mathrm{O}] = k_{\mathrm{eff}}[\mathrm{C}][\mathrm{O}], \qquad (6.1)$$

99

where

$$k_{\text{eff}} = \frac{k_{\text{rec}} k_{\text{des}}}{k_{\text{dis}} + k_{\text{des}}} \propto \exp\left(\frac{-E_{\text{eff}}}{k_{\text{B}}T}\right), \tag{6.2}$$

where k_{B} is the Boltzmann constant, T is the absolute temperature and

$$E_{\text{eff}} \approx E_{\text{rec}} + E_{\text{des}} - E_{\text{dis}} = 2.41 \text{ eV}. \tag{6.3}$$

We have assumed that $k_{\text{dis}} \gg k_{\text{des}}$ and that the prefactor is the same for each of the steps. The effective desorption energy barrier of 2.41 eV is consistent with the observed high temperature required of recombination, assuming a typical prefactor of 10^{13} s^{-1}.

7.0   DIRECT OBSERVATION OF MOLECULARLY-ALIGNED MOLECULES IN THE SECOND PHYSISORBED LAYER-CO/AG(110)

The contents of this chapter were taken from Lee, J.G., Hong, S.H., Ahner, J., Zhao, X.C., Chen, L., Johnson J.K., and Yates, J.T., *Chem. Phys. Lett.* **418**,86,(2005). The classical simulation part was performed by Zhao X.C.. The first pricinples simulation part was performed by myself.

7.1   INTRODUCTION

The formation of multilayers by adsorption on surfaces at low temperatures is a fundamental concept that has been recognized since the early days of the study of adsorption[114]. The first chemisorbed layer on planar crystalline surfaces involves the formation of relatively strong chemical bonds with the surface, often producing translationally-ordered and azimuthally-oriented molecules [115, 116]. The second layer is generally described as a more weakly-bound layer, held mainly by van der Waals forces. The second layer is often envisioned as being liquid like, but there are examples of long range translational ordering in this layer in certain systems[117, 118, 119, 120]. One of the first quantitative descriptions of this sequence of adsorption from monolayer to multilayer was developed over 60 years ago in the BET theory of adsorption[121]. In this report, we present direct evidence that a second adsorbed layer can possess a distinct angular registry with the underlying localized chemisorbed monolayer and the single crystal substrate. We demonstrate that the orientational ordering of the physisorbed second layer is a result of a delicate balance of forces from *both* the underlying Ag(110) surface *and* the chemisorbed first layer of CO.

7.2 EXPERIMENTAL METHODS

An atomically clean Ag(110) surface at 25 K was exposed to CO using a collimated molecular beam doser delivering a known flux to the crystal [122]. The time-of-flight ESDIAD (electron stimulated desorption ion angular distribution) method[123] was employed to study the angular distribution of electron-stimulated desorption products. In addition, low energy electron diffraction (LEED) measurements were made using the ESDIAD apparatus in the LEED mode.

Temperature programmed desorption (TPD) was used to probe the energetics of CO desorption from the Ag(110) surface. A constant heating rate of 0.336 K/s was used.

The ESDIAD, LEED, and TPD measurements were carried out as a function of CO exposure. The CO exposure is expressed as monolayers (ML) of incident CO, where 1 monolayer = 8.5×10^{14} CO molecules/cm^2, which is the density of surface Ag atoms on the crystal.

7.3 SIMULATION METHODS

We have used both quantum and classical simulation methods to model the adsorption of CO on the Ag(110) surface. Electronic structure density functional theory (DFT) calculations were performed using the spin polarized generalized gradient approximation. The Vienna ab initio simulation package[94, 95, 96] was used for all calculations. The revised Perdew Burke Ernzerhof (rPBE)[97, 98] exchange-correlation functional was used because this functional has been shown to give better binding energies for CO adsorbed on transition metals[100]. The rPBE functional binding energy at 0.5 ML is 0.17 eV, which is in good agreement with the binding energy at the same coverage measured from TPD of 0.15 eV. The electron-ion interactions were described by PAW (Projector Augmented Wave) pseudopotentials[101]. The Brillouin zone was sampled with 32 irreducible k-points generated from the Monkhorst-Pack scheme. An energy cutoff of 400 eV was used in all calculations. The rPBE calculated lattice constant for bulk Ag is 4.23 Å, in reasonable agreement with the experimental value

of 4.09 Å. The computed gas phase CO bond length is 1.14 Å, which is identical to the experimental value.

The Ag(110) surface was modeled as (4×1) and (2×2) slabs, each with 4 layers with a 15 Å vacuum region above the surface. The topmost 2 layers were relaxed. The fractional change in the distance between the first and second layers was Δd_{12}=-12.5% and Δd_{23}=9% between the second and third layers; these values are in good agreement with reported experimental[124] and calculated data[125].

The binding energies and geometries for CO in the first layer at 0.25, 0.5 and 1 ML coverages have been computed and are given in Table 10 . The binding energies are defined as $E_b = E_{Ag} + nE_{CO} - E_{Ag\text{-}CO}$, where E_{Ag} and E_{CO} are the total energies of the Ag slab and isolated CO molecule, respectively, and $E_{Ag\text{-}CO}$ is the energy of the Ag surface with n adsorbed CO molecules. The binding energies are very weak compared with chemisorption of CO on other metals and one may ask if the first layer is actually physisorbed, rather than chemisorbed. We believe that chemisorption is a better descriptor for the CO/Ag(110) monolayer atop interactions because the Ag-C distance is less than 2.2 Å as shown in Table 10, which is similar to metal-carbon bond distances for CO chemisorbed on other metals. In contrast, N_2 physisorbed on Ag(110) is reported to have an Ag-N distance of 3.7 Å and a binding energy of about 0.039 eV.

Classical simulations employing semi-empirical atomistic potentials have been used to study the angular and positional ordering of the second (physisorbed) layer of CO on the Ag(110) surface as a function of the geometry and charge distribution of the underlying metal surface and chemisorbed first layer. A potential model for the CO molecule was taken from the literature[126]; it consists of two Lennard-Jones (LJ) sites and three charge sites to account for the multipole moments of CO. The Ag atoms were represented as LJ sites with parameters taken from Ramseyer et al.[127]. The cross interactions were computed from Lorentz-Berthelot combining rules for the LJ parameters. The Ag atoms in the outer surface layer are given a positive charge of +0.2 |e|. The second layer Ag atoms are given a charge of –0.2 |e|. This charging scheme is qualitatively consistent with the Smoluchowski effect for a corrugated metal surface[128, 129]. A potential cutoff of 15.3 Å was applied to all LJ interactions and no long-range corrections were applied. The electrostatic interactions

were computed with the same cut off, but the reaction field method was used to account for the electrostatic long-range corrections. Molecular simulations at 25 K were performed in both the grand canonical (GCMC) and the canonical (NVT) ensembles[32]. GCMC was used to generate the desired coverage of CO molecules in the second layer followed by NVT moves to efficiently sample angle and position distributions. Histograms of the CO bond angles with respect to the Ag surface principal azimuths and surface normal were collected from 40 independent simulations.

7.4 RESULTS AND DISCUSSION

We focus on the behavior of the O^+ fragment from the ESDIAD measurements. The ion yield (ions/electron) as a function of the exposure is shown in Figure 45 . The O^+ yield exhibits characteristic breaks as the monolayer, second layer and the multilayer develop. Initially, the O^+ yield is low up to an exposure of 0.5 ML, and a weak maximum in ion yield is observed at about 0.2 ML (see Figure 45 inset). The decrease of the ion yield as the coverage becomes complete in the chemisorbed layer has been observed in other adsorption systems and is attributed to adsorbate-adsorbate interactions that quench the electronic excitation, decreasing the efficiency of ionization per incident electron[130]. As seen in Figure 46, in the region of the chemisorbed monolayer development up to 0.5 ML, two different O^+ ESDIAD patterns, A and B, are observed in different coverage regimes. The direction of O^+ emission in these patterns is closely related the direction of the C-O bond in the chemisorbed molecules. In pattern A, the CO molecules are oriented normally and a sharp normal O^+ ESDIAD beam is observed. The conversion from pattern A to pattern B indicates that at high coverages in the first chemisorbed layer, repulsive intermolecular interactions cause the molecules to undergo a change in C-O bond direction as the molecules tilt away from each other as the chemisorbed monolayer becomes saturated.
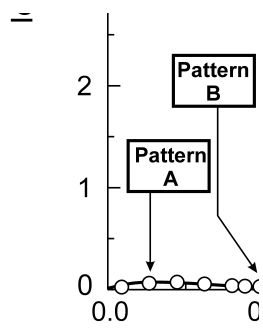
Figure 45: O$^+$ ion yield for adsorbed CO on Ag(110) as the exposure to CO increases at 25 K.

The LEED measurements (not shown) indicate that the chemisorbed CO exhibits a (2×1) two-dimensional periodicity at 0.5 ML coverage. Abruptly, at the onset of the development of the second physisorbed monolayer, a very large increase in the O^+ yield occurs and a unique 4-beam O^+ ion angular distribution pattern is observed (Figure 46, pattern C). The increase in O^+ yield is caused by a lower rate of ion neutralization for second-layer molecules, a phenomenon often seen in electron stimulated desorption as a result of the greater distance of second-layer molecules from the surface[116, 131]. The DFT calculations corroborate the ion yield observations; the chemisorbed CO molecules have a Ag-C bond length of 2.2 Å, whereas the second layer CO molecules are at least 4 Å from the surface. Finally, as the CO coverage increases into the multilayer regime, a fourth O^+ ESDIAD pattern (Figure 46, pattern D) develops as the ion yield continues to increase.

In the first stages of the formation of the chemisorbed monolayer, the C-O bond is oriented normally to the surface. The DFT calculations confirm that for 0.25 ML coverage the chemisorbed C-O bond axis is parallel to the surface normal in the ground state (see Table 10). In Figure 47B, as the coverage of the first layer increases, the normal O^+ beam is replaced by a two-beam O^+ pattern where the two beams are oriented off normal in azimuths parallel to the <001> azimuth of the Ag(110) crystal. This indicates that the CO molecules tilt away from the normal in azimuthal directions parallel to the <001> azimuth of the crystal. The chemisorbed C-O bond tilt angle from the normal is 26°. Similar molecular tilting effects have been seen in a number of cases for CO chemisorption on (110) metal surfaces[132, 133]. All polar angles measured here are influenced slightly by final state effects, which modify the ion ejection angle by a few degrees[134, 135]. Corrections for these effects are made in reporting the C-O bond directions[136]. In addition, corrections due to ion optical effects between the planar grids and the crystal at positive potential have been made in all angular measurements reported here. The tilting of the polar angle is also observed in DFT calculations. At 0.5 ML the CO molecules adsorbed on the atop sites display a polar angle of 24°, which is in very good agreement with the experimentally measured value of 26°. We note that CO on the Ni(110) surface is bound to the short bridge (s-b) site in the ground state[108]. In contrast, the s-b site for CO on Ag(110) is about four times less strongly bound than CO on the atop site (see Table 10).
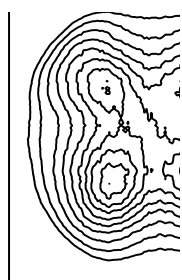
Exposure = 0

Figure 46: The observed O^+ ESDIAD patterns from CO on Ag(110) at various exposures at 25 K.

Table 10:   Binding energies, E_b, and geometries of chemisorbed CO on the Ag(110) surface. The polar angle is the angle between C-O bond axis and the surface normal. s-b is short bridge site.

Coverage	E_b (eV)	Polar angle	d(Ag-C) (Å)	d(C-O) (Å)
0.25 ML (atop)	0.144	0	2.19	1.15
0.5 ML (atop)	0.17	24 $^\circ$	2.16	1.15
0.5 ML (s-b)	0.04	59 $^\circ$	2.39	1.15
1.0 ML (atop)	0.05	0 $^\circ$	2.20	1.15

As the second physisorbed CO layer forms, the two-beam O^+ pattern is replaced by a distinctively different four-beam pattern. Here O^+ ions are ejected along diagonal azimuths at angles of about 45 $^\circ$ to the principal azimuthal axes of the (110) surface, as shown in Figure 46C. This is the key new finding, indicating that the second layer of physisorbed CO recognizes the structure of the underlying first layer of chemisorbed CO and the crystal substrate by adopting specific C-O bond directions that relate in a new and unexpected geometrical manner to the direction of the principal azimuths of the surface. In the physisorbed CO, the O atom is directed outward. The O^+ ion for the second layer are ejected at an angle of 43 $^\circ$ to the normal. The DFT calculations confirm that the second layer physisorbed structure is azimuthally ordered. Calculations carried out in the (4×1) cell gave an angle of 56°.

Note that the experiments show that at coverages greater than 0.5 ML CO is physisorbed in the second layer, which indicates that a full monolayer of CO chemisorbed on the Ag(110) surface is not energetically favorable. In contrast, CO/Ni(110) does form a full monolayer. The lattice constant for Ag is larger than that for Ni of 3.52 Å, so the lack of a stable chemisorbed full monolayer is unexpected. Our DFT calculations confirm that full monolayer coverage of CO on Ag(110) is energetically unfavorable compared with 0.5 ML (chemisorbed) plus 0.5 ML (physisorbed). The 1 ML coverage binding energy is 0.05 eV (Table 10) compared with 0.1 eV binding energy for 0.5 ML plus 0.5 ML. Adsorbate-adsorbate repulsion

is much more important for the CO/Ag(110) case than the CO/Ni(110) system because the binding energy for CO/Ni(110) is about one order of magnitude greater than that for CO/Ag(110).

As the CO coverage is increased still further into the multilayer region, a broad normally-oriented O^+ pattern superimposed on the underlying $45°$ pattern develops (Pattern 2D). The larger breadth of this angular distribution, compared to that of the original chemisorbed CO (Pattern 2A), indicates that CO species exhibiting random C-O bond directions exist at multilayer coverages above the second layer. The underlying two CO layers and the Ag(110) crystal have little influence on the orientation of the CO molecules in the third and higher layers.

To be certain that a layered surface is forming in these experiments, we carried out experiments in which the first two distinct layers were occupied by sequential dosing of CO isotopomers. Figure 47 shows the TPD spectrum of CO from a layer dosed with 0.78 ML of $C^{16}O$ (mainly chemisorbed) followed by 0.10 ML of second-layer $C^{18}O$. Several thermal desorption processes are seen. Near 30 K, the thermal desorption process from the second layer results in a sharp desorption peak, and this peak contains approximately equal amounts of the two CO isotopomers. At temperatures above about 35 K, two desorption processes from the chemisorbed monolayer are observed, and here only a small fraction of $C^{18}O$ is desorbed compared to the $C^{16}O$, which was adsorbed first. This result indicates that the second physisorbed layer and the first chemisorbed layer are energetically distinct, and that only slow isotopomer exchange occurs between the layers when they are grown in the manner described here. The second layer is weakly bound compared to the first layer.
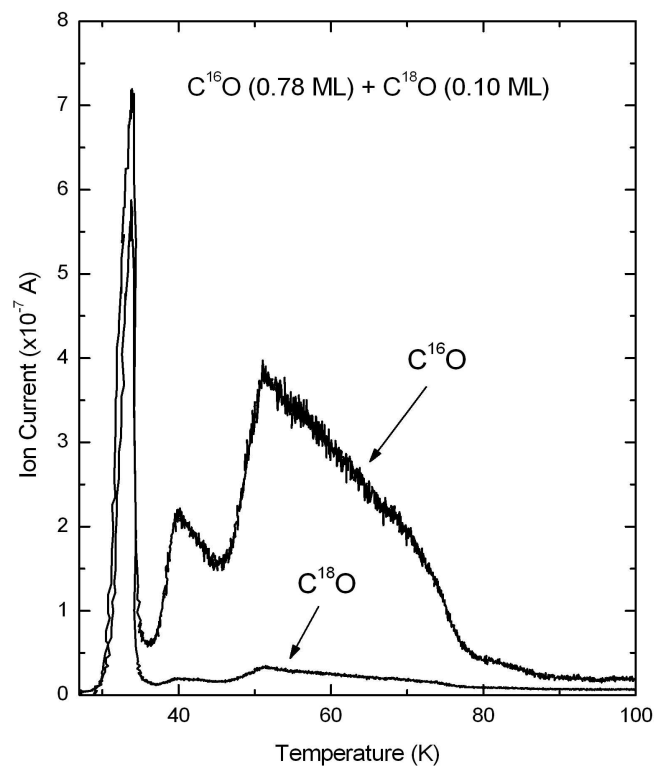
Figure 47: Temperature programmed desorption measurement of CO as a function of coverage.

We have performed classical simulations to investigate the role of charge distribution and geometry on the orientational ordering of the physisorbed layer. Several different configurations of the chemisorbed layer were investigated, along with several different charge distributions in the top two layers of Ag (Smoluchowski effect). Note that reliable charge distributions cannot be calculated within planewave periodic density functional theory. We therefore treated the charges on the top two Ag layers and on the chemisorbed CO molecules as adjustable parameters, while maintaining charge neutrality on both the Ag slab and the CO molecules. Simulations were carried out for the physisorbed second layer at 25 K for the various geometries and charge schemes and the positional and orientational ordering of the physisorbed CO layer was monitored. Agreement with experiment was found for the following case: The chemisorbed CO molecules were placed on the Ag(110) surface in the experimentally observed (2×1) periodicity at 0.5 ML coverage. The CO bond directions were tilted in accordance with the experimental measurements at 26° from the surface normal along the <001> azimuth, with CO molecules tilted in opposite directions in each of the rows as one moves along the close-packed $< 1\bar{1}0 >$ azimuthal direction. This actually gives a (4×1) periodicity when one takes into account the tilt angle. This point is discussed below. We assumed that the chemisorbed CO molecules maintained the same bond length and LJ parameters as gas phase CO, in agreement with the DFT finding that the C-O bond length does not change substantially. The CO charge distribution was modified by adding and subtracting 0.2 |e| to the charge sites closest to and farthest from the O site, respectively. The adjusted charges give a dipole moment of 1.8 Debye for the chemisorbed CO.

A representative snapshot from a simulation is shown in Figure 48. The silver colored atoms represent Ag, the yellow and green atoms represent chemisorbed CO, yellow being the C atoms. The blue and red atoms are physisorbed CO, with blue representing the C atoms. We observe from the snapshot that virtually all the second layer CO molecules adsorb with the oxygen atoms pointing away from the surface and that the majority of the physisorbed CO molecules are tilted near one of four different azimuthal angles at 45° to the principal crystal axes of the (110) surface. Probability distributions of the CO bond angles averaged over 40 independent simulations are shown in Figure 49. The solid line is the probability density of observing CO molecules with various azimuthal angles with respect to

the $< 1\bar{1}0 >$ direction. It can be seen that there are peaks in the azimuthal angle probability at $45\,^{\circ}$, $135\,^{\circ}$, $225\,^{\circ}$, and $315\,^{\circ}$ with respect to $< 1\bar{1}0 >$, in excellent agreement with the ESDIAD experiments.
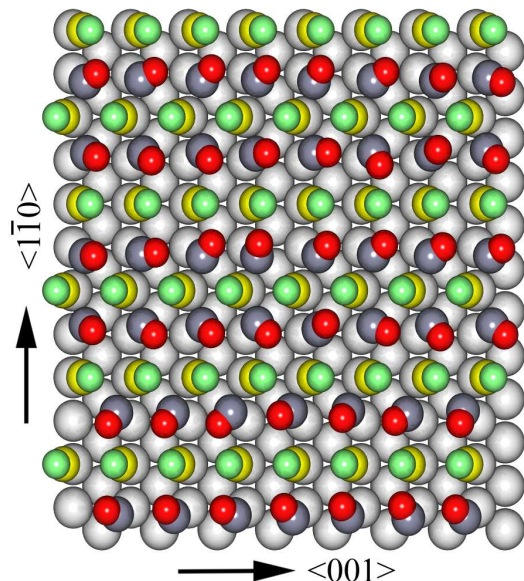

Figure 48: A snapshot of a molecular simulation of CO adsorbed on the Ag(110) surface (top). The silver spheres represent Ag atoms. The yellow and green atoms represent chemisorbed CO, where the yellow spheres represent the position of the C atoms. The physisorbed (second layer) CO molecules are shown as gray (carbon) and red (oxygen) atoms. Note that the second layer CO prefers to adsorb near a row of chemisorbed CO molecules, giving different row spacing. Also adjacent second layer rows can undergo lateral displacement making out of registry structures. The side view is shown in the bottom panel.

The agreement with experiment is remarkable given the simplicity of the model. The dashed curve in Figure 49 is the probability density of observing the second-layer C-O bond direction at a given angle with respect to the Ag(110) surface normal. It can be seen that the most probable C-O bond angle is at about $50\,^{\circ}$ to the normal, in reasonable agreement with the experimentally measured ion-ejection angle of $43\,^{\circ}$. The azimuthal ordering of CO in the second layer is very sensitive to the charges on the Ag atoms in the first and second layer in the model. If we remove the charges from the Ag atoms then no azimuthal ordering
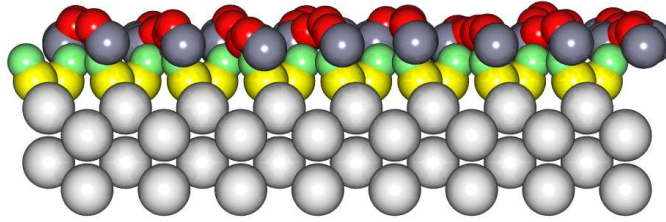
Figure 49: The probability densities of the angles made by the CO molecules in the second layer. The solid line is the probability density for C-O bond directions oriented azimuthally with respect to the $< 1\bar{1}0 >$ azimuth. The peaks indicate that CO molecules are preferentially ordered at angles of 45° with respect to the principal azimuthal axes of the (110) surface. The dashed line is the probability density for the C-O bond polar angles measured with respect to the (110) surface normal

is observed, even with the chemisorbed CO molecules in place. Likewise, the orientation and charges on the chemisorbed CO molecules are also crucial for generating the correct angular distribution. If the chemisorbed CO molecules are all pointing in the same direction (2×1) rather than alternating (4×1), then the simulated physisorbed CO molecules do not preferentially point along directions at 45° to the principal azimuths. This was also observed in the DFT calculations. If a (2×2) cell was used to model the 0.5 ML plus 0.5 ML system then the physisorbed molecules were aligned parallel to the $< 1\bar{1}0 >$ direction, instead of at an angle to the principle azimuths. However, DFT calculations with the (4×1) did produce azimuthal ordering, but with angles of about 56° rather than 45°. The (4×1) unit cell for the chemisorbed CO layer, which is required by simulation to produce the 45° orientation in the CO second layer, may appear as a (2×1) structure in LEED due to missing spots resulting from the glide symmetry of the (4×1) structure.

7.5 CONCLUSIONS

We have shown by direct physical measurements and by quantum and classical simulations that a physisorbed second layer exhibits unique azimuthal orientations as a result of weak interactions with an underlying ordered chemisorbed layer bound to a single crystal substrate. Density functional theory calculations show that adsorbate-adsorbate repulsion prevents the formation of a full chemisorbed monolayer of CO on Ag(110). Both classical and DFT calculations indicate that the chemisorbed CO molecules in neighboring rows must be oriented in opposite directions in order for the second layer CO molecules to adopt non-zero azimuthal angles. Classical simulations indicate that the azimuthal ordering is due to a combination of factors, including (1) structure of the Ag surface, (2) orientation of the first layer CO molecules, (3) charges on the top Ag layers, and (4) the charge distribution in the first layer CO molecules. If any one of these factors is different, then the correct C-O bond orientation is not observed. Thus, the azimuthal ordering results from a delicate balance of forces. We expect that similar orientational ordering may occur for many similar systems when the energy barrier to rotation is large compared to the thermal energy. These observations also indicate that the widely postulated extrinsic precursor state, bound extrinsically by physical adsorption forces to an underlying chemisorbed layer, may also possess azimuthal order at sufficiently low temperatures. Such molecular orientational effects can govern the molecule's dynamical behavior as it participates in precursor-mediated adsorption and reaction processes on a surface.
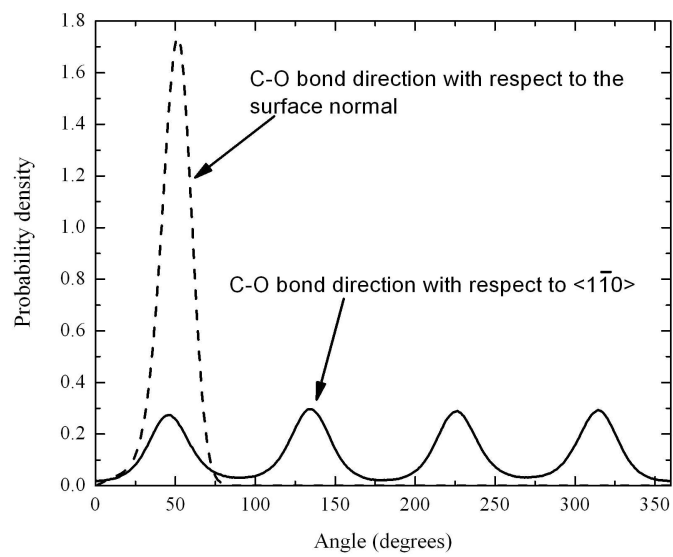
Figure 50: Angular Orientation of Second Layer CO on Ag(110)

8.0 FIRST PRINCIPLES STUDY OF TUNGSTEN DIFFUSION IN COBALT

The contents of this chapter were taken from Chen, L. and Johnson, J.K., in preparation.

8.1 INTRODUCTION

Experimental work has shown that microwave processing of materials such as tungsten carbide with cobalt produce functional materials with much higher strength and corrosion resistance than thermally sintered materials. Experiments show that the electric and magnetic fields play different roles in the processing of materials. However, there is little fundamental understanding of the underlying physics of microwave processing. It is not known exactly how or why microwave processed materials possess better properties.

It is experimentally known that thermally sintered WC/Co materials have about 20 wt% W dissolved in the Co binder phase, whereas microwave processed materials have almost no W in the Co phase.[137] This dramatic difference may be due to different mobilities of W in thermally and microwave processed materials. We are therefore studying diffusion processes in the Co phase, at first in the absence of an Electric-Magnetic field in this paper. We will study the diffusion phenomena in two steps. First, we present a study at vacancy formation and diffusion in bulk cobalt in this paper. Second, the diffusion mechanism of tungsten within defective cobalt is also presented in this work.

Haglund and Agren [138] have studied the diffuison of tungsten and carbon into solid cobalt phase. At temperatures below 1123 K, the tungsten is found to be practically immobilized. The diffusion coefficients are $5.3 \times 10^{-18} \mathrm{m}^2/\mathrm{s}$ at 1123 K and $6.9 \times 10^{-15} \mathrm{m}^2/\mathrm{s}$ at

1473 K, respectively. Lavergne and Allibert [139] found the diffusion coefficient of tungsten in molten cobalt to be $2 \times 10^{-9} \mathrm{m}^2/\mathrm{s}$ at 1723 K. They also estimated the diffusion coefficient of carbon in liquid cobalt to be $1 \times 10^{-8} \mathrm{m}^2/\mathrm{s}$ to $2 \times 10^{-8} \mathrm{m}^2/\mathrm{s}$. The diffusion coefficients for carbon and tungsten are of the same order of magnitude in liquid cobalt, while in solid cobalt, the diffusion coefficient of carbon is three to five orders of magnitudes larger than that of tungsten.

There are a few possible mechanisms for diffusion of substitutional atoms. First, atoms can migrate by directly exhanging sites, with the correlated motion of adjacent atoms. But this would entail very large distortions in the crystal. Second, in crystals such as germanium and silicon which have a diamond cubic structure with sufficient free space, the atoms may be forced into interstitial positions during diffusion.[140] Third, the distortions in the direct exchange mechanism can be reduced by the ring diffusion mechanism, but this has the disadvantage that many atoms have to move in a correlated manner. This mechanism is common in liquids and amorphous solids, which have more free space. Hence, it has been studied both experimentally and theoretically in various ordered and disordered systems such as microelectronic devices and transitors.[140, 141]

Density functional theory has (DFT) been shown to be capable of accurately calculating the defect formation energies and migration barrier energies, which are especially important in vacancy-mediated diffusion. Liu et al.[142] have studied the diffusion mechanism of P in Si by using DFT method. They paid special attention to structural exploration and charge effects. Their calculated diffusion activation energies in both interstitial and vacancy mediated diffusion are in agreement with experimental values. Mehrer et al.[143] have studied diffusion of various elements in decagonal quasicrystals: Co and Ni in AlNiCo by using radiotracer techniques. The diffusivities follow Arrhenius-like temperature dependencies. The small diffusion anisotropy is a strong argument in favour of vacancy-mediated diffusion. Pankratov et al.[140] studied the ring mechanism of diffusion of As impurity in Si by using DFT methods. They found the vacancy-mediated diffusion of substitutional impurities in Si drastically depends on the character of the impurity-vacancy interactions. The attractive interaction, which extends to at least the third nearest neighbors, allows a vacancy to move along a ring of Si sites around the impurity. This process enables the impurity-vacancy pair

to move and underlies the ring mechanism of diffusion. Venezuela et al.[144] have studied the vacancy-mediated diffusion in diordered SiGe alloys. Their calculations have shown that the vacancy formation energies have a strong dependence on the configuration of the nearest neighbor atoms. Ramanarayanan et al.[141] have tried to develop a systematic scheme to relate the macroscopic activation energy to the energy barriers of microscopic processes. They also presented the numerical verification using kinetic Monte Carlo simulation in diamond lattice.

8.2   COMPUTATIONAL METHOD

Density functional theory calculations were performed using the spin polarized generalized gradient approximation. The Vienna ab initio simulation package [94, 95, 96] was used for all calculations. The Perdew-Wang (PW91) [97] exchange-correlation functional was used. The electron-ion interactions were described by ultrasoft pseudopotentials.[101, 102] The Brillouin zone was sampled with a 5×5×5 Monkhorst-Pack mesh.[103] An energy cutoff of 400 eV was used in all calculations. All atoms were fully relaxed with the forces converged to less than 0.05 eV/ Å. Electron smearing was employed using Methfessel-Paxton technique, with a smearing width of $\zeta = 0.1$ eV, in order to minimize the errors in the Hellmann-Feynman forces due to the electronic free energy. All calculated energies are extrapolated to $T = 0$ K. The cobalt lattice is chosen as FCC type, which is stable at the experimental temperatures (1500 K). The calculated lattice constants for bulk tungsten and cobalt are 3.18 Å and 3.54 Å respectively, which agree well with the experimental values of 3.17 Å and 3.54 Å.

The nudged elastic band (NEB) method of Jónsson and co-workers [104, 105] was used to determine the diffusion pathways. Initial and final states were chosen and the number of images was increased to achieve a smooth curve. A minimum of eight images were used for each calculation.
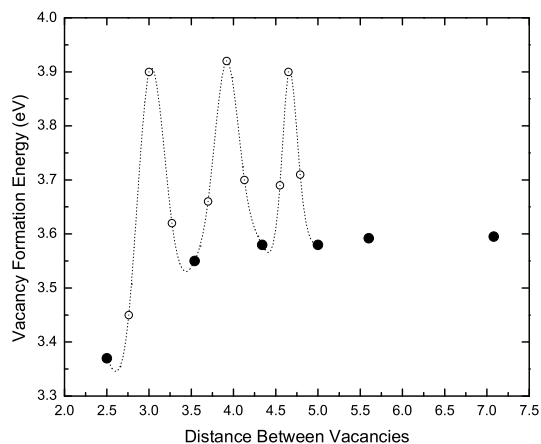
Figure 51: Vacancy-vacancy interactions

8.3 RESULTS AND DISCUSSIONS

8.3.1 Vacancy formation and self-diffusion

We have studied the formation of vacancy defects in bulk cobalt. A periodic supercell with 108 Co atoms was used for the non-defective bulk calculation. Single and adjacent double vacancy defects were generated and the defective structures were optimized. The formation energy was calculated by $E_{\mathrm{f}} = E_{(n-1)\mathrm{Co}} + E_{\mathrm{Co}}$ - $E_{n\mathrm{Co}}$. The formation energy for a single vacancy, which corresponds to about the 1 % concentration defect level, was found to be 1.75 eV. The formation energy for two adjacent defects, 2% concentration, was found to be 3.146 eV. The vacancy-vacancy interactions as a function of the separation between the vacancies is shown in Figure 51. The vacancy-vacancy interactions are short ranged. The formation energy of two vacancies in second nearest neighbors is 3.40 eV, roughly twice the formation energy of a single vacancy. The lower formation energy of two adjacent defects shows the two vacancies tend to coalesce.

The formation energy for three and four coalesced vacancies was found to be 4.78 and 6.31 eV, respectively. Table 1 shows the vacancy formation energy (VFE) and vacancy formation

119

energy per vacancy (VFEPV). VFEPV is roughly constant when the number of vacancies is greater than two. As a result, only single vacancies and di-vacancies are expected to exist at higher temperatures considering the entropy effect.

Table 11: Vacancy formation energy per vacant site

Number of Vacancies	1	2	3	4
VFE	1.75	3.40	4.78	6.31
VFEPV	1.75	1.57	1.59	1.58

We have studied the diffusion pathway of single and double vacancy defects in bulk cobalt by using the nudged elastic band method. In each NEB calculation, we used a minimum of eight linearly interpolated images along the reaction path in addition to the pre-optimized initial and final points. Figure 52 shows the diffusion pathway for a single vacancy. The diffusion of a single vacancy is equivilant to one of the nearest neighbor atoms moving into the vacant site. The calculated activation barrier energy is 0.46 eV. The overall vacancy mediated self-diffusion activation energy is a sum of the vacancy formation energy and vacancy migration energy. Therefore, the calculated activation energy for cobalt is 2.21 eV.

Figure 53 shows the diffusion pathway for the coalescence of two separated vacancies, where the calculated diffusion barrier is 0.53 eV. The calculated low diffusion barrier indicates that the vacancies are mobile and able to coalesce even at low temperature. The hopping rate for two separated vacancies coalescing is significant at 900K, assuming a prefactor of 10^{13} s^{-1}.

8.3.2 Substitutional impurity and diffusion

We have studied the the substitution of tungsten and carbon atoms within defective cobalt. We inserted one impurity atom into the pre-optimized defective structures, then preformed an accurate optimization with the forces converged to 0.05 eV/Å. The subsitution energy is defined as $E_s = E_I + E_{V/\mathrm{Co}} - E_{I/\mathrm{Co}}$ where the three terms on the right-hand side are the
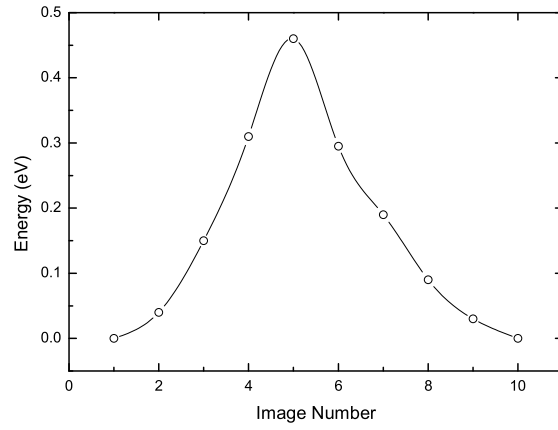
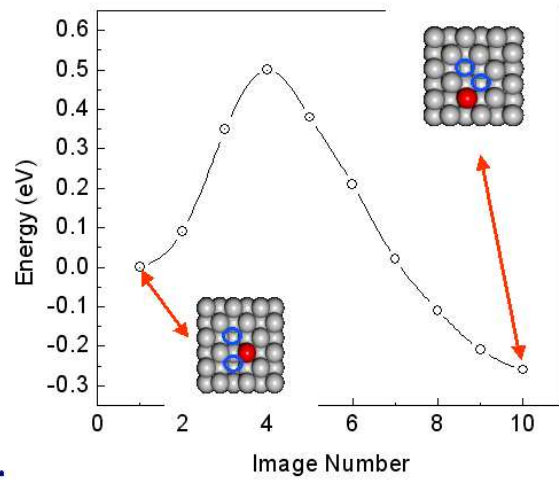Figure 52: Diffusion pathway of a single vacancy

Figure 53: Diffusion pathway of two vacancies: two seperated vacancies coalesce.

energy of single impurity atom, the energy of the defective Cobalt, and the energy of the Co with the substitution impurity atom, respectively. A positive value for E_b corresponds to a stable substitution with this definition. We have considered the substitution in one, two and three vacancies in the calculations. The calculated values of E_s are 0.85, 1.04 and 1.11 eV for one through three vacancies, respectively.

We have investigated two possible vacancy-mediated tungsten and carbon diffusion mechanisms: triangle and quadrangle mechanisms. In both cases, the diffusion consists of two steps. First, the substitutional tungsten or carbon jumps into the nearest neighboring empty site. As a result, the vacancy moves to the site previously occupied by the impurity. Second, the vacancy migrates to the first nearest Co site by following a triangle or qudrangle path, in the 111 or 100 planes, respectively. Figure 54 shows the calculated tungsten diffusion pathway of the triangle mechanism. The first peak in Figure 54 corresponds to the activation barrier for the exchange of W and a vacancy. The barrier height is 0.83 eV. The second peak corresponds to the barrier for the vacancy migration, with a height of 0.50 eV. The rate-limited step is the exchanging between tungsten and vacancy. Therefore, the overal tungsten diffusion activation energy is 2.58 eV, which is the sum of vacancy formation energy and activation barrier of the rate-limited step. The diffusion pathway following the qudrangle mechanism is shown in Figure 55. The three peaks are corresponding to the diffusion barrier of tungsten-vacancy exchange, vacancy moving from the first nearest neighbor of tungsten to the second nearest neighbor and vacancy moving to the first nearest neighbor on the other side, respetively. It is observed that tungsten-vacancy exchange is still the rate-limited step, which has a height of 0.83 eV.

8.4   CONCLUSION

In this paper, we have studied vacancy formation energy as a function of number of vacancies and vacancy coordinates. We found that vacancies tend to coalesce, and the interactions between them are very short ranged, which is negligible when the distance is larger than 3.5Å. The calculated cobalt self-diffusion activation energy is 2.21 eV. We have also evaluted
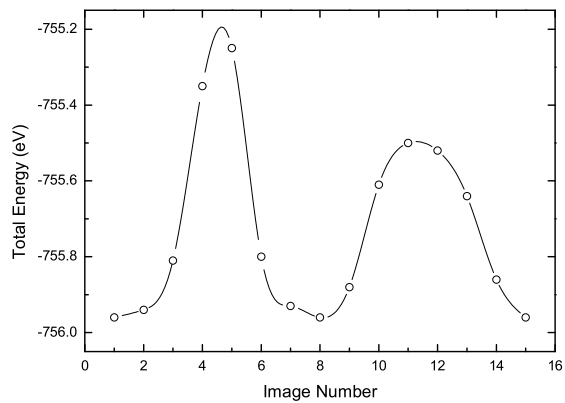
Figure 54: Diffusion pathway of tungsten: triangle mechanism. Activation barrier for the rate-limited step is 0.83 eV.

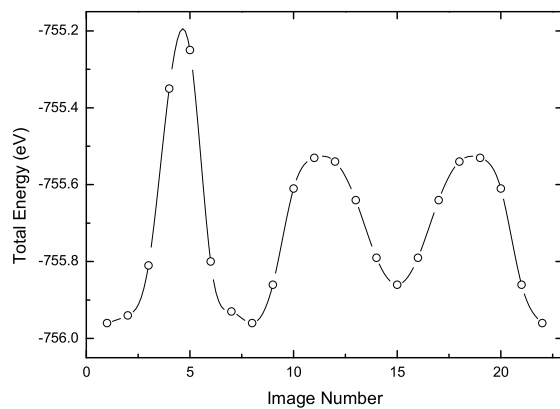Figure 55: Diffusion pathway of tungsten: qudrangle mechanism. Activation barrier for the rate-limited step is 0.83 eV.

W diffusion mechanisms in cobalt. The full diffusion pathways are calculated. In both mechanisms, the highest activation barriers are 0.83 eV. We will study the competition between the difference diffusion mechanisms by using kinetic Monte Carlo simulation in the subsequent paper.

9.0 FUTURE WORK

9.1 STUDY OF CO ADSORPTION, DIFFUSION AND REACTION ON WC SURFACE

Tungsten carbide is an important material for catalysis and fuel cell electrodes. However, very little is known about the fundamental processes on WC. This is partly because the tungsten carbide surface is complex and very hard to model. Therefore, investigating the catalytic properties of the tungsten carbide surface as an extension to our previous study on clean W(111) surface is highly expected. First principles methods will be required to study the adsorption, diffusion and dissociation of carbon monoxide, nitrogen monoxide and methane on the WC surface. WC(0001) and carbon modified W(111) surface would be very good candidates for the reactivity study. The adsorption of carbon monoxide and nitrogen monoxide can be studied, and compared with some published experimental results.[89, 145] Futhermore, the reaction pathway of methane reforming on the two surfaces can be calculated.

9.2 DIFFUSION OF CARBON AND TUNGSTEN IN DEFECTIVE COBALT

We have so far studied the diffusion pathways and mechanisms of vacancies and tungsten in defective cobalt without eletric or magnetic field by using DFT. The subsequent related study could be the vacancy-mediated diffusion mechanisms of carbon in cobalt. A similar triangle or qudrangle mechanism would work here as well as the interstitial-mediated mech-

anism. As an extension, the diffusion coefficients of carbon and tunsten diffusion in defective cobalt phase can be calcualted by using kinetic Monte Carlo, utilizing the possible diffusion pathways we have calculated from DFT. In the KMC method, larger super cell and periodic boundary conditions will be used to simulate the infinite bulk. Vacancy and impurity atoms are allowed to move according to the hopping rates calculated from the diffusion barriers. Finally, the diffusion coefficients will be calculated from the mean squared displacements and time.

We could also perform accurate first principles study of the vacancy, tungsten and carbon diffusion inside defective cobalt under external field(eletric field). Uniform electric field can be applied.[146, 147]

BIBLIOGRAPHY

[1] G. K. Papadopoulos. *J. Chem. Phys.*, 114:8139, 2001.

[2] W. Shi and J. K. Johnson. *Phys. Rev. Lett.*, 91:015504, 2003.

[3] M. C. Gordillo, J. Boronat, and J. Casulleras. *Phys. Rev. Lett.*, 85:2348, 2000.

[4] D. C. Sorescu, D. L. Thompson, M. M. Hurley, and C. F. Chabalowski. *Phys. Rev. B*, 66:035416, 2002.

[5] J. B. Claridge, A. P. E. York, A. J. Brungs, C. Marques-Alvarez, J. Sloan, S. C. Tsang, and M. L. H. Green. *J. Catal.*, 180:85, 1998.

[6] J. Chen. *Chem. Rev.*, 96:1477, 1996.

[7] S. Iijima. *Nature*, 354:56, 1991.

[8] M. W. Cole, V. H. Crespi, G. Stan, C. Ebner, J. M. Hartman, S. Moroni, and M. Boninsegni. *Phys. Rev. Lett.*, 84:3883, 2000.

[9] M. M. Calbi, S. M. Gatica, M. J. Bojan, and M. W. Cole. *J. Chem. Phys*, 115:9975, 2001.

[10] S. M. Gatica, M. J. Bojan, G. Stan, and M. W. Cole. *J. Chem. Phys*, 114:3765, 2001.

[11] W. Kohn and L. J. Sham. *Phys. Rev.*, 140:A1133, 1965.

[12] P. Hohenberg and W. Kohn. *Phys. Rev. B*, 76:6062, 1964.

[13] J. P. Cheng, D. K. Agrawal, S. Komarneni, M. Mathis, and R. Roy. *Materials Research Innovations*, 1:44, 1997.

[14] D. K. Agrawal. *Current Opinion in Solid State and Materials Science*, 3:480, 1998.

[15] E. Breval, J. P. Cheng, D. K. Agrawal, P. Gigl, M. Dennis, R. Roy, and A. J. Papworth. *in preparation*, 2004.

[16] D. S. Bethune, C. H. Kiang, G. Gorman, R. Savoy, J. Vazquez, and R. Beyers. *Nature*, 363:605, 1993.

[17] M. Muris, N. Dupont-Pavlovsky, M. Bienfait, and P. Zeppenfeld. *Surf. Sci.*, 492:67–74, 2001.

[18] S. Talapatra and A. D. Migone. *Phys. Rev. Lett.*, 87:206106, 2001.

[19] S. E. Weber, S. Talapatra, C. Journet, A. Zambano, and A. D. Migone. *Phys. Rev. B*, 61:13150, 2000.

[20] V. V. Simonyan, J. K. Johnson, A. Kuznetsova, and J. T. Yates. *J. Chem. Phys.*, 114:4180, 2001.

[21] G. Stan, V. H. Crespi, M. W. Cole, and M. Boninsegni. *J. Low Temp. Phys.*, 113:447, 1998.

[22] T. Duren and F. J. Keil. *Chem. Eng. Technol.*, 24:698, 2001.

[23] D. B. Mawhinney, V. Naumenko, A Kuznetsova, J. T. Yates, J. Liu, and R. E. Smalley. *Chem. Phys. Lett.*, 324:213, 2000.

[24] A. Kuznetsova, D. B. Mawhinney, V. Naumenko, J. T. Yates, J. Liu, and R. E. Smalley. *Chem. Phys. Lett.*, 321:292, 2000.

[25] D. B. Mawhinney, V. Naumenko, A Kuznetsova, J. T. Yates, J. Liu, and R. E. Smalley. *J. Am. Chem. Soc.*, 122:2383, 2000.

[26] D. B. Mawhinney and J. T. Yates. *Carbon*, 39:1167, 2001.

[27] A. Kuznetsova, J. T. Yates, V. V. Simonya, J. K. Johnson, C. B. Huffman, and R. E. Smalley. *J. Chem. Phys.*, 115:6691, 2001.

[28] A. Kuznetsova, J. T. Yates, J. Liu, and R. E. Smalley. *J. Chem. Phys.*, 112:9590, 2000.

[29] M. K. Kostov, M. W. Cole, J. C. Lewis, P. Diep, and J. K. Johnson. *Chem. Phys. Lett.*, 332:26–34, 2000.

[30] R. P. Fournier, R. Savoie, F. Bessette, and A. Cabana. *J. Chem. Phys.*, 49:1159, 1968.

[31] V. Zhukov, I. Popova, and J. T. Yates. *J. Vac. Sci. Technol. A*, 18:992, 2000.

[32] M. P. Allen and D. J. Tildesley. Oxford, Clarendon, 1987.

[33] R. L. Rowley. *Statistical Mechanics for Thermophysical Property Calculations*. Englewood Cliffs, Prentice Hall, 1994.

[34] R. Q. Snurr and J. Kärger. *J. Phys. Chem. B*, 101:6469, 1997.

[35] W. A. Steele. *Surf. Sci.*, 36:317, 1973.

[36] P. Nextoux, M. Drifford, L. Belloni, and A. Vinit. *Mol. Phys.*, 49:1375, 1983.

[37] V. Buch, L. Delzeit, C. Blackledge, and J. P. Devlin. *J. Chem. Phys.*, 100:3732, 1996.

[38] L. H. Jones and B. I. Swanson. *J. Phys. Chem*, 95:2701, 1991.

[39] M. Gilbert and M. Drifford. *J. Chem. Phys.*, 66:3205, 1977.

[40] J. R. Scherer. *Adv. Infrared Raman Spectrosc.*, 16:352, 1960.

[41] J. C. Evans and N. Wright. *Spectrochimica Acta*, 16:352, 1960.

[42] J. C. Evans. *Spectrochimica Acta*, 16:994, 1960.

[43] J. Bertie and J. P. Devlin. *J. Chem. Phys.*, 79:2092, 1983.

[44] J. P. Devlin, P. J. Wooldridge, and G. Ritzhaupt. *J. Chem. Phys.*, 84:6095, 1986.

[45] J. R. Scherer, M. K. Go, and S. Kint. *J. Phys. Chem*, 77:2108, 1973.

[46] O. Byl, P. Kondratyuk, S. Forth, S. Fitzgerald, J. T. Yates, L. Chen, and J. K. Johnson. *J. Am. Chem. Soc.*, 125:5889, 2003.

[47] O. Byl, P. Kondratyuk, and J. T. Yates. *J. Phys. Chem. B*, 107:4277, 2003.

[48] W. Yim, O. Byl, J. T. Yates, and J. K. Johnson. *J. Chem. Phys.*, 120:5377, 2004.

[49] Christopher Matranga, Liang Chen, Milton Smith, Edward Bittner, J. Karl Johnson, and Bradley Bockrath. *J. Phys. Chem. B*, 107:12930–12941, 2003.

[50] C. Matranga and B. Bockrath. *J. Phys. Chem. B*, 108:6170–6174, 2004.

[51] M. Arab, F. Picaud, M. Devel, C. Ramseyer, and C. Girardet. *Phys. Rev. B*, 69:165401, 2004.

[52] A. Kleinhammes, S. Mao, X. Yang, X. Tang, H. Shimoda, J. Lu, O. Zhou, and Y. Wu. *Phys. Rev. B*, 68:75418, 2003.

[53] M. Cinke, J. Li, Bauschlicher C., A. Ricca, and M. Meyyappan. *Chem. Phys. Lett.*, 376:761, 2003.

[54] J. Zhao, A. Buldum, A. Han, and J. Pinglu. *Nanotechnology*, 13:195, 2002.

[55] J. G. Harris and K. H. J. Yung. *J. Phys. Chem.*, 99:12021, 1995.

[56] G. Stan, M. W. Cole, and M. Boninsegni. *Surf. Sci.*, 395:280, 1998.

[57] S. Talapatra, V. Krungleviciute, and A. D. Migone. *Phys. Rev. Lett.*, 89:246106, 2002.

[58] S. Talapatra and A. D. Migone. *Phys. Rev. B*, 65:045416, 2002.

[59] S. Talapatra, A. Z. Zambano, S. E. Weber, and A. D. Migone. *Phys. Rev. Lett.*, 85:138–141, 2000.

[60] I. Noda. *Appl. Spectrosc.*, 47:1329, 1993.

[61] I. Noda. *Appl. Spectrosc.*, 54:994, 2000.

[62] I. Noda, A. E. Dowrey, C. Marcott, G. M. Story, and Y. Ozaki. *Appl. Spectrosc.*, 54:236, 2000.

[63] T. Graim and D. P. Landau. *Phys. Rev. B*, 24:5156, 1980.

[64] M. Bienfait, P. Zeppenfeld, N. Dupont-Pavlovsky, J. P. Palmari, M. R. Johnson, T. Wilson, M. Depies, and O. E. Vilches. *Phys. Rev. Lett.*, 91:035503, 2003.

[65] A. J. Zambano, S. Talapatra, and A. D. Migone. *Phys. Rev. B*, 64:075415, 2001.

[66] J. C. Lasjaunias, K. Biljakovic, J. L. Sauvajol, and P. Monceau. *Phys. Rev. Lett.*, 91:025901, 2003.

[67] W. Teizer, R. B. Hallock, E. Dujardin, and T. W. Ebbesen. *Phys. Rev. Lett.*, 82:5305, 1999.

[68] D. G. Narehood, M. K. Kostov, P. C. Eklund, M. W. Cole, and P. E. Sokol. *Phys. Rev. B*, 65:233401, 2002.

[69] T. Wilson and O. E. Vilches. *Low Temp. Phys.*, 29:732, 2003.

[70] S. Ramachandran, T. A. Wilson, D. Vandervelde, D. K. Holmes, and O. E. Vilches. *J. Low Temp. Phys.*, 134:115, 2004.

[71] T. Wilson, A. Tyburski, M. R. Depies, O. E. Vilches, D. Becquet, and M. Bienfait. *J. Low Temp. Phys.*, 126:403, 2002.

[72] M. Bienfait, P. Zeppenfeld, N. Dupont-Pavlovsky, M. R. Johnson, T. Wilson, M. DePies, and O. E. Vilches. *Phys. Rev. B*, 70:035410, 2004.

[73] Christopher Matranga, Liang Chen, Bradley Bockrath, and J. Karl Johnson. *Phys. Rev. B*, 70:165416, 2004.

[74] M. Cinke, J. Li, C. W. Bauschlicher, A. Ricca, and Meyyappan M. *Chem. Phys. Lett.*, 376:761–766, 2003.

[75] D. J. Wales and J. P. K. Doye. *J. Phys. Chem. A*, 101:5111, 1997.

[76] J. P. K. Doye and D. J. Wales. *Phys. Rev. Lett.*, 80:1357, 1998.

[77] D. J. Wales and H. A. Scheraga. *Science*, 285:1368, 1999.

[78] A. P. Lyubartsev, A. A. Martsinovski, S. V. Shevkunov, and P. N. Vorontsovel. *J. Chem. Phys.*, 96:1776–1783, 1992.

[79] E. Marinari and G. Parisi. *Europhys. Lett.*, 19:451, 1992.

[80] C. J. Geyer and E. A. Thompson. *J. Am. Stat. Soc.*, 90:909, 1995.

[81] J. Potoff and J. I. Siepmann. *AIChE Journal*, 47:1676, 2001.

[82] R. A. Beebe, A. V. Kiselev, N. V. Kovaleva, J. R. Holmes, and M. E. R. Camplin. *Russ. J. Phys. Chem.*, 38:506, 1964.

[83] A. Terlain and Y. Larher. *Surface Science*, 125:304–311, 1983.

[84] Miles J. Weida, Jeanette M. Sperhac, and David J. Nesbitt. *J. Chem. Phys.*, 103:7685, 1995.

[85] M. Welker, G. Steinebrunner, J. Solca, and H. Huber. *Chem. Phys.*, 213:253, 1996.

[86] G. A. Somorjai. Wiley, New York, 1994.

[87] S. P. Mehandru and B. Anderson. *Surf. Sci.*, 201:345, 1988.

[88] C. E. Bartosch, L. J. Whitman, and W. Ho. *J. Chem. Phys.*, 85:1052, 1986.

[89] H. H. Hwu, B. D. Polizzotti, and J. G. Chen. *J. Phys. Chem. B*, 105:10045, 2001.

[90] S. Lee, YD Kim, TS. Yang, JH Boo, SC Park, SB Lee, and CY Park. *J. Vac. Sci. Technol. A*, 18:1455, 2000.

[91] G. H. Ryu, S. C. Park, and S.-B. Lee. *Surf. Sci.*, 427–428:419, 1999.

[92] A. B. Anderson. *J. Chem. Phys.*, 62:1187, 1975.

[93] A. B. Anderson, R. W. Grimes, and S. Y. Hong. *J. Phys. Chem.*, 91:4245, 1987.

[94] G. Kresse and J. Hafner. *Phys. Rev. B*, 49:14251, 1994.

[95] G. Kresse and J. Furthmuller. *Comput. Matter. Sci.*, 6:15, 1996.

[96] G. Kresse and J. Furthmuller. *Phys. Rev. B*, 54:11169, 1996.

[97] J. P. Perdew., K. Burke, and M. Ernzerhof. *Phys. Rev. Lett.*, 77:3865, 1996.

[98] Y. Zhang and W. Yang. *Phys. Rev. Lett.*, 80:890, 1998.

[99] J. P. Perdew, J. A. Chevary, S. H. Vosco, K. A. Jackson, M. R. Pederson, D. J. Singh, and C. Fiolhais. *Phys. Rev. B*, 46:6671, 1992.

[100] B. Hammer, L. B. Hansen, and J. K. Nørskov. *Phys. Rev. B*, 59:7413, 1999.

[101] G. Kresse and J. Joubert. *Phys. Rev. B*, 59:1758, 1999.

[102] P. E. Blochl. *Phys. Rev. B*, 50:17953, 1994.

[103] H. J. Monkhorst and J. D. Pack. *Phys. Rev. B*, 13:5188, 1976.

[104] G. Mills, H. Jónsson, and G. K. Schenter. *Surf. Sci.*, 324:305, 1995.

[105] H. Jónsson, G. Mills, and K. W. Jacobsen. In B. J. Berne, G. Ciccotti, and D. F. Coker, editors, *Classical and Quantum Dynamics in Condensed Phase Simulations*, Singapore; River Edge, NJ, 1998. World Scientific.

[106] W. Xu and J. B. Adams. *Surf. Sci.*, 319:45, 1994.

[107] N. A. W. Holzwarth, J. A. Chervenak, C. J. Kimmer, Y. Zheng, , W. Xu, and J. B. Adams. *Phys. Rev. B*, 48:12136, 1993.

[108] V. Shah, T. Li, K. L. Baumert, H. Cheng, and D. S. Sholl. *Surf. Sci.*, 217:537, 2003.

[109] C. E. Bartosch, L. J. Whitman, and W. Ho. *J. Chem. Phys.*, 85:1052, 1986.

[110] J. G. Lee, J. Ahner, and J. T. Yates. *J. Chem. Phys*, 114:1414, 2001.

[111] M. Polanyi and E. Wigner. *Z. Phys. Chem.*, 139:439, 1928.

[112] T. Li, B. Bhatia, and D. S. Sholl. *J. Chem. Phys*, 121:10241, 2004.

[113] J. J. Mortensen, L. B. Hansen, B. Hammer, and J. K. Nørskov. *J. Catal.*, 182:479, 1998.

[114] A. W. Adamson. Wiley, New York, 1990.

[115] M. A. Van Hove, W. H. Weinberg, and C.-M. Chan. volume 6 of *Springer Series in Surface Sciences*. Springer-Verlag, Berlin, 1986.

[116] R. D. Ramsier and Jr. Yates, J.T. *Surf. Sci. Rep.*, 12:246, 1991.

[117] S. K. Wang, J. C. Newton, R. Wang, H. Taub, and J. R. Dennison. *Phys. Rev. B*, 39:10331, 1989.

[118] G. S. Leatherman and R. D. Diehl. *Langmuir*, 12:7063, 1997.

[119] P. Jakob and D. Menzel. *Surf. Sci.*, 220:70, 1989.

[120] C. Benndorf and T. E. Madey. *Surf. Sci.*, 135:164, 1983.

[121] S. Brunauer, P. H. Emmett, and E. Teller. *J. Am. Chem. Soc.*, 60:309, 1938.

[122] Jr. Yates, J.T. AIP press and Springer-Verlag, New York, 1998.

[123] J. Ahner, D. Mocuta, and Jr. Yates, J.T. *J. Vac. Sci. Technol. A*, 17:2333, 1999.

[124] J. R. Noonan and H. L. Davis. *Vacuum*, 32:107, 1982.

[125] Jun Wan, Y. L. Fan, D. W. Gong, S. G. Shen, and X. Q. Fan. *Modelling Sim. Mat. Sci. Eng.*, 7(2):189–206, 1999.

[126] J. Piper, J. A. Morrison, and C. Peters. *Mol. Phys.*, 53:1463, 1984.

[127] C. Ramseyer, C. Girardet, F. Bartolucci, G. Schmitz, R. Franchy, D. Teillet-Billy, and J. P. Gauyacq. *Phys. Rev. B*, 58:4111, 1998.

[128] R. Smoluchowski. *Phys. Rev.*, 60:661, 1941.

[129] R. Gomer. American Vacuum Society Classic. AIP, NewYork, 1993.

[130] F. P. Netzer and T. E. Madey. *J. Chem. Phys.*, 76:710, 1982.

[131] F. P. Netzer and T. E. Madey. *Surf. Sci.*, 119:422, 1982.

[132] W. Riedl and D. Menzel. *Surf. Sci.*, 163:39, 1985.

[133] J. Ahner, D. Mocuta, R. D. Ramsier, and Jr. Yates, J.T. *J. Chem. Phys.*, 105:6553, 1996.

[134] Z. Miškovic, J. Vukanic, and T. E. Madey. *Surf. Sci.*, 141:285, 1984.

[135] Z. Miškovic, J. Vukanic, and T. E. Madey. *Surf. Sci.*, 169:405, 1986.

[136] Q. Gao, C. C. Cheng, P. J. Chen, W. J. Choyke, and Jr. Yates, J.T. *J. Chem Phys.*, 98:8308, 1993.

[137] E. Breval, J.P. Cheng, D.K. Agrawal, P. Gigl, M. Dennis, R. Roy, and A.J. Papworth. *Mat. Sci. Eng. A*, 391:285–295, 2005.

[138] S. Haglun and J. Ågren. *Acta Mater.*, 46:2801, 1998.

[139] O. Lavergne and C. H. Allibert. *High Temp. High Press.*, 31:347–355, 1999.

[140] O Pankratov, H. C. Huang, T. D. de la Rubia, and C Mailhiot. *Phys. Rev. B*, 56:13172, 1997.

[141] P. Ramanarayanan, B. Scrinivasan, K. Cho, and B. M. Clemens. *J. Appl. Phys.*, 96:7095–7107, 2004.

[142] XY Liu, W Winl, KM Beardmore, and MP Masquelier. *App. Phys. Lett.*, 82:1839–1841, 2003.

[143] H Mehrer and R Galler. *J. Alloy and Compounds*, 342:296–301, 2002.

[144] P Venezuela, G. M. Dalpian, J. R. A. da Silva, and A. Fazzio. *Phys. Rev. B*, 65:193306, 2002.

[145] M. Zhang, H.H. Hwu, M.T. Buelow, J.G. Chen, T.H. Ballinger, P.J. Andersen, and D.R. Mullins. *Surf. Sci.*, 522:112–122, 2003.

[146] D. Vanderbilt. *Ferroelectrics*, 301:9–14, 2004.

[147] M. Machado, P. Piquini, and M. Mota. *Nanotechnology*, 16:302–306, 2005.